HADRONIC MATRIX ELEMENTS IN LATTICE QCD

DISSERTATION ZUR ERLANGUNG DES GRADES
"DOKTOR DER NATURWISSENSCHAFTEN"

VORGELEGT AM FACHBEREICH PHYSIK,
MATHEMATIK UND INFORMATIK DER JOHANNES
GUTENBERG UNIVERSITÄT IN MAINZ

JOHANNES GUTENBERG
UNIVERSITÄT MAINZ

BENJAMIN JÄGER

GEBOREN IN IDAR-OBERSTEIN

Mainz, den 12. Mai 2014

Benjamin Jäger: *Hadronic Matrix Elements in Lattice QCD*

DATUM DER PROMOTION:
12. Mai 2014 D77

ABSTRACT

The lattice formulation of *Quantum ChromoDynamics* (QCD) has become a reliable tool providing an *ab initio* calculation of low-energy quantities. Despite numerous successes, systematic uncertainties, such as discretisation effects, finite-size effects, and contaminations from excited states, are inherent in any lattice calculation. Simulations with controlled systematic uncertainties and close to the physical pion mass have become state-of-the-art. We present such a calculation for various hadronic matrix elements using non-perturbatively $\mathcal{O}(a)$-improved Wilson fermions with two dynamical light quark flavours. The main topics covered in this thesis are the axial charge of the nucleon, the electro-magnetic form factors of the nucleon, and the leading hadronic contributions to the anomalous magnetic moment of the muon.

Lattice simulations typically tend to underestimate the axial charge of the nucleon by $5-10\%$. We show that including excited state contaminations using the summed operator insertion method leads to agreement with the experimentally determined value. Further studies of systematic uncertainties reveal only small discretisation effects. For the electro-magnetic form factors of the nucleon, we see a similar contamination from excited states as for the axial charge. The electro-magnetic radii, extracted from a dipole fit to the momentum dependence of the form factors, show no indication of finite-size or cutoff effects. If we include excited states using the summed operator insertion method, we achieve better agreement with the radii from phenomenology.

The anomalous magnetic moment of the muon can be measured and predicted to very high precision. The theoretical prediction of the anomalous magnetic moment receives contribution from strong, weak, and electro-magnetic interactions, where the hadronic contributions dominate the uncertainties. A persistent 3σ tension between the experimental determination and the theoretical calculation is found, which is considered to be an indication for physics beyond the Standard Model. We present a calculation of the connected part of the hadronic vacuum polarisation using lattice QCD. Partially twisted boundary conditions lead to a significant improvement of the vacuum polarisation in the region of small momentum transfer, which is crucial in the extraction of the hadronic vacuum polarisation.

ZUSAMMENFASSUNG

Die Gitterformulierung der *QuantenChromoDynamik* (QCD) hat sich zu einem sehr verlässlichen Werkzeug entwickelt, mit dem eine rein theoretische Beschreibung der Hadronenphysik möglich ist. Neben einer Vielzahl von Erfolgen zeigen alle Gitterrechnungen eine Reihe von systematischen Unsicherheiten wie Diskretisierungseffekte, Effekte aufgrund des endlichen Volumens, und Verzerrungen aufgrund von angeregten Zuständen. Simulationen mit nahezu physikalischer Pionmasse und kontrollierten systematischen Unsicherheiten gehören zum heutigen Stand der Technik. Wir präsentieren die Ergebnisse einer solchen Rechnung für verschiedene hadronische Matrixelemente mittels $\mathcal{O}(a)$-verbesserter Wilson-Fermionen mit zwei leichten Quarks. Die Schwerpunkte dieser Arbeit sind die axiale Ladung des Nukleons, die elektromagnetischen Formfaktoren des Nukleons und die führenden hadronischen Beiträge zum anomalen magnetischen Moment des Muons.

Gitterrechnungen unterschätzen typischerweise die axiale Ladung des Nukleons um etwa $5-10\%$. Wir zeigen dass durch die Berücksichtigung von angeregten Zustände mittels der „summed operator insertion“ Methode Übereinstimmung mit dem experimentellen Wert erreicht werden kann. Untersuchungen der systematischen Unsicherheiten zeigen nur wenige Diskretisierungseffekte. Die elektromagnetischen Formfaktoren des Nukleons zeigen ähnliche Verschiebungen durch angeregte Zustände wie die axiale Ladung. Die elektromagnetischen Radien können aus Fits an die Impulsabhängigkeit der Formfaktoren extrahiert werden, und wir sehen für diese keine Anzeichen für Diskretisierungseffekte oder Effekte aufgrund des endlichen Volumens. Sofern wir die angeregten Zustände durch die „summed operator insertion“ Methode berücksichtigen, erreichen wir eine bessere Übereinstimmung mit dem Experiment.

Das anomale magnetische Moment des Myons kann mit sehr hoher Präzision gemessen und berechnet werden. In den theoretischen Berechnungen tragen starke, schwache und elektromagnetische Wechselwirkungen bei, wobei die Beiträge der starken Wechselwirkung die Unsicherheiten dominieren. Eine seit langem stabile Abweichung von mehr als drei Standardabweichungen zwischen dem Experiment und theoretischen Vorhersagen kann als Hinweis für Physik jenseits des Standard Modells aufgefasst werden. Wir präsentieren eine Gitterrechnung des verbunden Anteils der hadronischen Vakuumpolarisation des Myons. Die Wahl von „partially twisted“ Randbedingungen führen zu einer Verbesserung der Auflösung kleiner Impulsüberträge, welche besonders für die Bestimmung der hadronischen Vakuumpolarisation wichtig ist.

CONTENTS

I LATTICE QCD 1

1 OVERVIEW 3
1.1 Lattice regularisation . . . 4
1.2 Discretisation of the QCD action . . . 5
1.3 Quantisation and numerical simulations . . . 9
1.4 Gauge configurations . . . 10
1.5 Quark bi-linears and currents . . . 11
1.6 Partially twisted boundary conditions . . . 14

II FORM FACTORS OF THE NUCLEON 17

2 INTRODUCTION 19

3 LATTICE CALCULATION 25
3.1 Two-point function of the pion . . . 26
3.2 Two-point function of the nucleon . . . 28
3.3 Three-point function of the nucleon . . . 31
3.4 Smearing . . . 34
3.5 Ratios . . . 36
3.6 Excited states . . . 38
3.7 Momentum dependence . . . 41

4 THE AXIAL CHARGE OF THE NUCLEON 45
4.1 Chiral behaviour . . . 45
4.2 Cutoff effects . . . 49
4.3 Finite-size effects . . . 49

5 NUCLEON ELECTRO-MAGNETIC FORM FACTORS 53
5.1 Chiral behaviour . . . 57
5.2 Cutoff and finite-size effects . . . 60

6 CONCLUSIONS AND OUTLOOK 63

III HADRONIC VACUUM POLARISATION FOR $(g-2)_\mu$ 67

7 INTRODUCTION 69
7.1 Experimental determination . . . 69
7.2 Standard Model prediction for a_μ . . . 71
7.2.1 Electro-magnetic contributions . . . 71
7.2.2 Weak contributions . . . 72
7.2.3 Strong contributions . . . 73
7.3 Comparison of theory and experiment . . . 75

8 LATTICE CALCULATIONS 77
8.1 Vacuum polarisation . . . 78

8.2 Partially twisted boundary conditions . . . 80
8.3 Ward-Takahashi identities . . . 82
8.4 Fitting procedure . . . 84
8.5 Numerical integration . . . 87
9 RESULTS 89
9.1 Hadronic vacuum polarisation in $N_f = 2$ . . . 89
9.2 Hadronic vacuum polarisation in $N_f = 2 + 1_Q$ . . . 90
9.3 Chiral behaviour . . . 91
9.4 Cutoff effects . . . 95
9.5 Finite-size effects . . . 97
9.6 Fit uncertainties - Q^2 dependence . . . 98
10 CONCLUSIONS AND OUTLOOK 101

IV APPENDIX 105
A APPENDIX 107
A.1 Gamma matrices . . . 107
A.2 Heavy Baryon chiral perturbation theory fit . . . 108

BIBLIOGRAPHY 115

PUBLICATIONS

Parts of this work have already appeared in the following publications:

A. Francis, B. Jäger, H. B. Meyer, and H. Wittig, *A new representation of the Adler function for lattice QCD*, *Phys.Rev.* D88 (2013) 054502, arXiv:1306.2532.

G. M. von Hippel, B. Jäger, T. D. Rae, and H. Wittig, *The Shape of Covariantly Smeared Sources in Lattice QCD*, *JHEP* 1309 (2013) 014, arXiv:1306.1440.

M. Della Morte, B. Jäger, T. D. Rae, and H. Wittig, *Improved interpolating fields for hadrons at non-zero momentum*, *Eur.Phys.J.* A48 (2012) 139, arXiv:1208.0189.

S. Capitani, M. Della Morte, G. von Hippel, B. Jäger, A. Jüttner, et al., *The nucleon axial charge from lattice QCD with controlled errors*, *Phys.Rev.* D86 (2012) 074502, arXiv:1205.0180.

M. Della Morte, B. Jäger, A. Jüttner, and H. Wittig, *Towards a precise lattice determination of the leading hadronic contribution to* $(g-2)_\mu$, *JHEP* 1203 (2012) 055, arXiv:1112.2894.

S. Capitani, M. Della Morte, D. Djukanovic, G. von Hippel, B. Jäger, et al., *A high-statistics study of the nucleon EM form factors, axial charge and quark momentum fraction*, *PoS* (Lattice 2013) 272, arXiv:1311.5804.

A. Francis, B. Jäger, H. B. Meyer, and H. Wittig, *Adler function and hadronic vacuum polarization from lattice vector correlation functions in the time-momentum representation*, *PoS* (Lattice 2013) 305, arXiv:1311.3285.

G. von Hippel, J. Hua, B. Jäger, H. Meyer, T. D. Rae, et al., *Fitting strategies to extract the axial charge of the nucleon from lattice QCD*, *PoS* (Lattice 2013) 446.

G. M. von Hippel, B. Jäger, T. Rae, and H. Wittig, *Getting Covariantly Smeared Sources into Better Shape*, *PoS* (Lattice 2013) 424.

M. Della Morte, G. Herdoiza, H. Horch, B. Jäger, A. Jüttner, et al., *Computing the Adler function from the vacuum polarization function*, *PoS* (Lattice 2013) 304.

M. Della Morte, G. Herdoiza, H. Horch, B. Jäger, A. Jüttner, et al., *Fitting the Lattice Vacuum Polarisation Function to Perturbation Theory*, *PoS* (Lattice 2013) 444.

S. Capitani, M. Della Morte, G. von Hippel, B. Jäger, B. Knippschild, et al., *Excited state systematics in extracting nucleon electro-magnetic form factors from the lattice*, *PoS* ConfinementX (2012) 321.

M. Della Morte, B. Jäger, T. D. Rae, and H. Wittig, *Improved interpolating fields for hadrons at non-vanishing momentum*, *PoS* (Lattice 2012) 260, arXiv:1211.1288.

S. Capitani, M. Della Morte, G. von Hippel, B. Jäger, B. Knippschild, et al., *Excited state systematics in extracting nucleon electro-magnetic form factors*, *PoS* (Lattice 2012) 177, arXiv:1211.1282.

M. Della Morte, B. Jäger, A. Jüttner, and H. Wittig, *Lattice calculations of the leading hadronic contribution to* $(g-2)_\mu$, *PoS* (Lattice 2012) 175, arXiv:1211.1159.

B. Brandt, M. Della Morte, B. Jäger, A. Jüttner, and H. Wittig, *Hadronic contribution to the lepton anomalous magnetic moment and pion form factor in lattice QCD*, *Prog.Part.Nucl.Phys.*67 (2012) 223–227.

M. Della Morte, B. Jäger, H. Wittig, and A. Jüttner, *Lattice Determination of the Anomalous Magnetic Moment of the Muon*, *PoS* (Lattice 2011) 161, arXiv:1111.2193.

M. Della Morte, B. Jäger, A. Jüttner, and H. Wittig, *The leading hadronic vacuum polarisation on the lattice*, *AIP Conf.Proc.* 1343 (2011) 337–339, arXiv:1011.5793.

B. B. Brandt, S. Capitani, D. Djukanovic, G. von Hippel, B. Jäger, et al., *Wilson fermions at fine lattice spacings: scale setting, pion form factors and* $(g-2)_\mu$, *PoS* (Lattice 2010) 164, arXiv:1010.2390.

Part I

LATTICE QCD

1

OVERVIEW

Quantum ChromoDynamics (QCD), the theory of the strong interactions, is a non-Abelian gauge theory, which describes the interaction of quarks and gluons. The quarks are the fermionic building blocks of QCD, occurring in six different flavours: up, down, charm, strange, top, and bottom. Quarks carry, in addition to an electric and weak charge, a strong charge, which appears in three different states (red, green, blue). The strong force is mediated by massless gluons, which carry also, in contrast to photons, a colour and an anti-colour charge. The self-coupling of the gluons generates the non-Abelian character of QCD. In this work, we use natural units

$$\hbar = c = 1 \tag{1}$$

and employ Einstein's summation convention. The Lagrangian of QCD can be written, in analogy to QED, as

$$\mathscr{L} = -\frac{1}{2g_0^2}\mathrm{Tr}(F_{\mu\nu}F^{\mu\nu}) + \sum_f \overline{\psi}_f(\gamma_\mu D^\mu + m_f)\psi_f, \tag{2}$$

where the field-strength tensor is given by

$$F_{\mu\nu} = \partial_\mu A_\nu - \partial_\nu A_\mu + [A_\mu, A_\nu]\,. \tag{3}$$

The non-vanishing commutator in equation (3) accounts for the self-interaction of the gluons, which is depicted in figure 1. The covariant derivative in equation (2) couples quarks and gluons and is defined as

$$D_\mu = \partial_\mu + \mathrm{i}A_\mu. \tag{4}$$

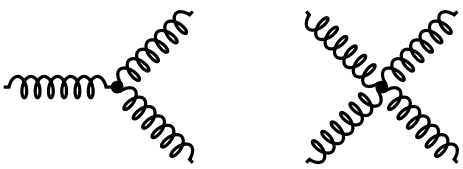

Figure 1: Schematic of self-interaction of gluons.

The parameters of QCD are the bare coupling constant g_0 and the masses m_f of the quarks. Due to *asymptotic freedom*, the theoretical treatment of QCD differs in the low- and high-energy regimes. For small momentum transfer, the coupling constant scales to ~ 1, so that perturbation theory is not applicable. Quarks are bound into colour-neutral hadrons, which is known as *confinement* and explains why free quarks cannot be observed. Hadrons are classified as mesons ($\overline{q}q$), consisting of a quark and an anti-quark, and baryons (qqq), which are made up of three quarks. At large energies, the coupling constant decreases and QCD becomes asymptotically free, which allows perturbation theory to be used. For the discovery of asymptotic freedom [1], Gross, Politzer and Wilczek received the Nobel prize in 2004.

Lattice QCD provides a non-perturbative treatment of QCD in the low-energy regime. In the following section, a brief introduction to lattice QCD is presented. A complete discussion is beyond the scope of this thesis and more details can be found in a variety of textbooks and reviews [2–6]. Following the lines of [5, 6], Lattice QCD can be summarised by the procedure:

1. Discretise Euclidean space-time by a hyper-cubic lattice Λ,
2. Construct a discrete version of the QCD Lagrangian,
3. Quantise QCD using Euclidean path integrals,
4. Calculate expectation values using Monte Carlo techniques.

1.1 LATTICE REGULARISATION

The Euclidean metric, i.e. the replacement of $g_{\mu\nu}$ by $\delta_{\mu\nu}$, can be realised by a Wick rotation to imaginary times $t \to -it$, which removes the distinction between co- and contra-variant vectors. Euclidean space-time can be discretised by introducing a four-dimensional grid of points, which are separated by the lattice spacing a,

$$\Lambda = \left\{ n \in \mathbb{R}^4 \,\middle|\, {}^{n_0}/_a = 0, \dots, N_T \,;\, {}^{n_i}/_a = 0, \dots, N_L \right\}. \tag{5}$$

The extent of the simulation box is finite in time and space,

$$T = aN_T,\ L = aN_L. \tag{6}$$

A pictorial representation of the lattice Λ is shown in figure 2. The quark fields,

$$\overline{\psi}_f(n)^a_\alpha \quad \text{and} \quad \psi_f(n)^a_\alpha, \tag{7}$$

are associated with the lattice sites n and the indices: colour a, flavour f, and Dirac spinor α. To simplify the notation, we suppress all indices except

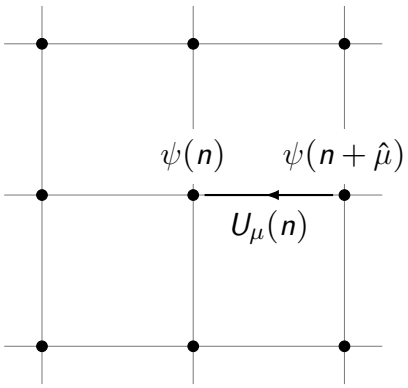

Figure 2: Pictorial representation of the lattice Λ.

the space-time coordinate, $\psi(n)$. Usually periodic or anti-periodic boundary conditions are imposed to mimic an infinite geometry,

$$\psi(n + L\,\hat{e}_k) = \psi(n). \tag{8}$$

The dual lattice can be obtained by a Fourier transformation, which leads to discrete momenta,

$$\Lambda^* = \left\{ p \in \mathbb{R}^4 \,\middle|\, p_0 = \frac{2\pi}{T} n_0\,;\; p_i = \frac{2\pi}{L} n_i \right\}. \tag{9}$$

We rewrite the gauge fields $A_\mu(z)$ in terms of a parallel transporter connecting two space-time points x and y by a path-ordered product,

$$U(x,y) = P \exp\left(-\int_y^x \mathrm{d}z\, A_\mu(z) \right). \tag{10}$$

The *Link variable* is defined as the parallel transporter connecting two neighbouring lattice sites n and $n+\hat{\mu}$ along a straight line,

$$U_\mu(n) := U(n, n+\hat{\mu}). \tag{11}$$

These gauge links are elements of $SU(3)$, which can be connected to the algebra-valued gauge fields by

$$U_\mu(n) = \exp(iaA_\mu(n)). \tag{12}$$

1.2 DISCRETISATION OF THE QCD ACTION

The gluonic part of the action QCD can be constructed from the gauge links $U_\mu(n)$, building the so-called *plaquette*

$$P_{\mu\nu}(n) = U_\mu(n) U_\nu(n+\hat{\mu}) U_\mu^\dagger(n+\hat{\mu}) U_\nu^\dagger(n), \tag{13}$$

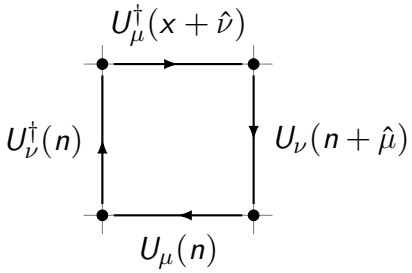

Figure 3: Pictorial representation of the plaquette $P_{\mu\nu}$.

which is the smallest closed gauge loop and is shown in figure 3. With these definitions, the *Wilson plaquette action* is given by

$$S_G = \frac{2}{g_0^2} \sum_n \sum_{\mu<\nu} \mathrm{Re}\,\mathrm{Tr}\,(1 - P_{\mu\nu}(n))\,. \tag{14}$$

It can be shown [6], that the Wilson gauge action approaches the continuum action in the limit of $a \to 0$,

$$\frac{2}{g_0^2} \sum_n \sum_{\mu<\nu} \mathrm{Re}\,\mathrm{Tr}\,(1 - P_{\mu\nu}) = \frac{a^4}{2g_0^2} \sum_n \sum_{\mu,\nu} \mathrm{Tr}\,(F_{\mu\nu}F_{\mu\nu}) + \mathscr{O}(a^6). \tag{15}$$

The choice of the gluonic action is not unique, so that different gauge action are used in lattice simulations. The so-called *Iwasaki action* [7] is, in addition to the Wilson plaquette action, commonly used by various lattice collaborations. The fermionic part of the action QCD is discretised by replacing the covariant derivative by

$$D_\mu\psi(x) \to \frac{1}{2a}\left(U_\mu(n)\psi(n+\hat{\mu}) - U_\mu^\dagger(n-\hat{\mu})\psi(n-\hat{\mu})\right), \tag{16}$$

where $U_\mu(n)$ ensures the gauge invariance of the Lagrangian and couples quark and gluons. Gauge invariance is an intrinsic property of the lattice formulation and is realised by transforming the spinor fields under a colour gauge transformation $g(n) \in \mathrm{SU}(3)$ as

$$\psi(n) \to g(n)\psi(n) \quad \text{and} \quad \overline{\psi}(n) \to \overline{\psi}(n)g(n)^\dagger. \tag{17}$$

Gauge invariance implies that the link-variables $U_\mu(n)$ transform as

$$U_\mu(n) \to g(n)U_\mu(n)g(n+\hat{\mu})^{-1}. \tag{18}$$

With these transformations, the gluonic and fermionic action remain, per construction, invariant. The so-called *naïve fermionic action* [6] is defined by

$$S_N = a^4 \sum_n \Big[\overline{\psi}(n)\frac{\gamma_\mu}{2a}\left(U_\mu(n)\psi(n+\hat{\mu}) - U_\mu^\dagger(n-\hat{\mu})\psi(n-\hat{\mu})\right) + m_0\,\overline{\psi}(n)\psi(n)\Big]. \tag{19}$$

As the Wilson plaquette action, the naïve fermionic action recovers its continuum counterpart in the limit $a \to 0$ and both parts of the action show discretisation effects of order $\mathcal{O}(a^2)$. The *Dirac operator* can be read off from the fermionic part of the action,

$$S_N = a^4 \sum_{n,m} \overline{\psi}(n) D(n,m) \psi(m) \tag{20}$$

with

$$D(n,m) = \frac{\gamma_\mu}{2a} \left(U_\mu(n) \delta_{n+\hat{\mu},m} - U_\mu^\dagger(n-\hat{\mu}) \delta_{n-\hat{\mu},m} \right) + m_0 \, \delta_{n,m}. \tag{21}$$

A Fourier transformation of equation (21) shows that the Dirac operator of the Naïve fermion action

$$\widetilde{D}(q,p) = \delta(p-q) \left(m_0 + \frac{\mathrm{i}}{a} \gamma_\mu \sin(p_\mu a) \right) \tag{22}$$

vanishes, in addition to the expected pole at $p = 0$, for $p_\mu = \frac{\pi}{a}$. This issue leads to 16 fermions in the simulation and is known as the *fermion doubling problem*. Wilson suggested in [8] to add a two-derivative term to the naïve Dirac operator, which removes the additional doublers and vanishes in the limit $a \to 0$. The *Wilson Fermion action* is defined as

$$\begin{aligned} S_W = a^4 \sum_n \Big[& -\frac{\kappa}{a} \overline{\psi}(n)(r - \gamma_\mu) U_\mu(n) \psi(n+\hat{\mu}) \\ & + \frac{\kappa}{a} \overline{\psi}(n)(r + \gamma_\mu) U_\mu^\dagger(n-\hat{\mu}) \psi(n-\hat{\mu}) + \overline{\psi}(n)\psi(n) \Big] \\ & + \frac{\beta}{3} \sum_n \sum_{\mu<\nu} \mathrm{Re}\,\mathrm{Tr}\left(1 - P_{\mu\nu}(n)\right), \end{aligned} \tag{23}$$

where we have rewritten the quark masses and the bare coupling constant g_0 in terms of the numerical parameters

$$\begin{aligned} \beta &= \frac{6}{g_0^2}, \\ \kappa &= \frac{1}{2am_0 + 8r}. \end{aligned} \tag{24}$$

The Wilson term explicitly breaks chiral symmetry,

$$\left\{ D_W, \gamma_5 \right\} \neq 0, \tag{25}$$

and its coefficient r is usually set to one. The *No-Go-Theorem* [9] by Nielsen and Ninomiya states that any local lattice regularisation cannot be free of doublers whilst preserving chiral symmetry. The Wilson term in equation (23) generates an additive renormalisation for the quark mass m and the *hopping parameter* κ,

$$m = \frac{1}{2a} \left(\frac{1}{\kappa} - \frac{1}{\kappa_c} \right) = m_0 - m_c. \tag{26}$$

The critical hopping parameter κ_c can, for instance, be obtained at the point where the pion mass vanishes. For the Wilson action, discretisation effects enter at the level $\mathcal{O}(a)$ in contrast to the naïve and the gauge action. Symanzik [10, 11] has shown that the leading discretisation effects can be removed by adding an appropriate counter-term to the action. By applying Symanzik's formalism to Wilson fermions, Sheikholeslami and Wohlert [12] have derived the following expression

$$S_{SW} = S_W + c_{SW}\, a^5 \sum_n \sum_{\mu<\nu} \frac{1}{2} \overline{\psi}(n) \sigma_{\mu\nu} \widehat{F}_{\mu\nu} \psi(n) + \mathcal{O}(a^2), \tag{27}$$

which requires the tuning of the parameter c_{SW} to remove leading lattice artefacts. We use the non-perturbatively determined improvement coefficients c_{SW} for the two-flavour theory in [13]. The field strength tensor in equation (27),

$$\widehat{F}_{\mu\nu}(n) = -\frac{\mathrm{i}}{8a^2} \left(Q_{\mu\nu}(n) - Q_{\nu\mu}(n) \right), \tag{28}$$

can be constructed from the so-called "*clover leaves*"

$$Q_{\mu\nu}(n) = P_{\mu\nu}(n) + P_{\mu\nu}(n - \hat{\mu}) + P_{\mu\nu}(n - \hat{\nu}) + P_{\mu\nu}(n - \hat{\mu} - \hat{\nu}), \tag{29}$$

where each consists of four plaquettes as shown in figure 4.

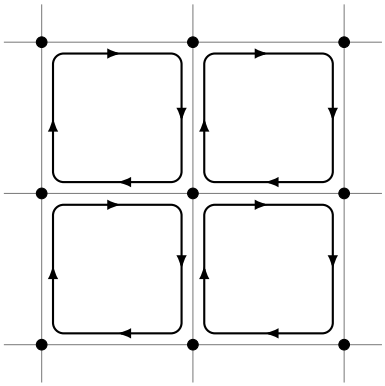

Figure 4: Pictorial representation of the clover-leaf $Q_{\mu\nu}$

The choice of the fermionic and gluonic action is not unique, so that various discretisations show different properties concerning for instance cutoff effects and chiral symmetry. In the limit $a \to 0$, all actions should reproduce the continuum definition. In the literature, *Wilson* [8], *Staggered* [14], *Overlap* [15, 16], *Domain Wall* [17] and *Twisted Mass* [18] are commonly used. A comparison amongst these action allows to check the consistency of the lattice approach. The Flavour Lattice Averaging Group (FLAG) [19, 20] provides a world average of low-energy results computed by various lattice calculations.

1.3 QUANTISATION AND NUMERICAL SIMULATIONS

The quantisation of the lattice formulation is achieved by using *Euclidean path integrals*. Integrating over all possible field configurations allows us to construct the expectation value of an operator A in the following way

$$\langle A \rangle = \frac{1}{Z} \int D[U] D[\psi, \overline{\psi}] A[U, \psi, \overline{\psi}] \, e^{-S_G[U]} e^{-S_F[U, \psi, \overline{\psi}]}. \tag{30}$$

Since the lattice introduces a finite set of variables, the path integral in equation (30) is mathematically well-defined. The operator A can be build from bi-linear combination of the spinor fields ψ and $\overline{\psi}$, and the gauge links U_μ. The fermionic degrees of freedom are represented by so-called *Grassmann variables*, which respect the anti-commuting properties of fermions. These fields can be integrated out since the action is bilinear in $\overline{\psi}$ and ψ:

$$\langle A \rangle = \frac{1}{Z} \int \prod_{n,\mu} \mathrm{d}U_\mu(n) \widetilde{A}[U] \left(\det D[U]\right)^{N_f} e^{-S_G[U]}, \tag{31}$$

where $\widetilde{A}$ denotes the operator, in which the fermionic degrees of freedom have been integrated out. The fermionic part reduces to a determinant with the number of degenerate quark flavours N_f. For many years, simulations were performed in the *quenched* approximation, in which contributions from the fermion determinant were neglected, $N_f = 0$. The quenched formulation leads to an uncontrolled approximation of QCD, which is not suited for a true ab initio calculation of QCD. The remaining gluonic integration is performed over the group SU(3) by the so-called *Haar measure*. The partition function Z of equation (31) is defined as

$$Z = \int \prod_{n,\mu} \mathrm{d}U_\mu(n) \left(\det D[U]\right)^{N_f} e^{-S_G[U]}. \tag{32}$$

Monte Carlo integration is advantageous in the case of very high-dimensional integrals, such as the integrals in equation (31), which in our case have more than $\mathcal{O}(10^7)$ degrees of freedom. A *configuration* of gauge fields is defined as the combination of all gauge links on the lattice Λ

$$\left\{ U_\mu(n) \,\middle|\, n \in \Lambda \,,\ \mu = 0, \ldots 3 \right\}. \tag{33}$$

A set of several configurations is called *ensemble*. To enable numerical simulation, we use the concept of *importance sampling* and compute the expectation value of an operator on a set of configurations, which are distributed according to the weight

$$W = \frac{1}{Z} \left(\det D[U]\right)^{N_f} e^{-S_G[U]}. \tag{34}$$

An estimate for the operator A can be obtained by its mean

$$\overline{A} = \frac{1}{N_{\mathrm{cfg}}} \sum_{i=1}^{N_{\mathrm{cfg}}} A_i, \tag{35}$$

assuming the configurations respect the weight in equation (34). The estimate $\overline{A}$ has an intrinsic statistical uncertainty, which will vanish in the limit of $N_{\text{cfg}} \to \infty$. In this work, we obtain the estimate and its statistical uncertainty using the so-called *Bootstrap* resampling method [21]. For a set of N configurations, a Bootstrap sample can be computed by the mean of N randomly chosen configurations $\{A\}$,

$$\widehat{A}_k = \frac{1}{N} \sum \{A\}. \tag{36}$$

Configurations might appear more than once in this set. We compute a large number of different bootstrap samples to estimate the real expectation value by the median of the distribution of these bootstrap samples

$$\langle A \rangle \sim \widetilde{A} = \text{median}\{\hat{A}_k\}. \tag{37}$$

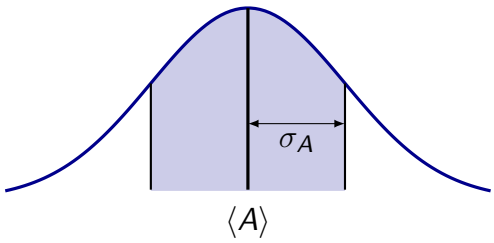

Figure 5: Schematic of the Bootstrap estimate and error.

The statistical uncertainty σ_A can be estimated by half of the width of the central 68 percentile, which is shown in figure 5. The uncertainty of a derived quantity $B = f(A)$ can be obtained identically by computing B for each individual bootstrap sample

$$\widehat{B}_k = f(\widehat{A}_k). \tag{38}$$

The estimate of B is again given by the median and half of the central 68%

$$f(\widetilde{A}) \pm \sigma_B. \tag{39}$$

In practice, we use 1000 bootstrap samples to estimate the statistical uncertainty, which we have cross-checked by the Jackknife error procedure [22, 23].

1.4 GAUGE CONFIGURATIONS

In this thesis, we use the gauge configurations generated by the CLS (Coordinated Lattice Simulations) initiative [25]. These configurations have been generated using the deflation accelerated DD-HMC [26–28] and MP-HMC [29] algorithm. Both simulation codes are based on the concept of the *Hybrid Monte Carlo (HMC)* algorithm [30] and combine several techniques to improve the

Labels	β	κ	size	a [fm]	L [fm]	m_π [MeV]	$m_\pi L$
A3	5.20	0.13580	64×32^3	0.079	2.5	473	6.0
A4	5.20	0.13590	64×32^3	0.079	2.5	363	4.7
A5	5.20	0.13594	64×32^3	0.079	2.5	312	4.0
B6	5.20	0.13597	96×48^3	0.079	3.8	267	5.1
E5	5.30	0.13625	64×32^3	0.063	2.0	456	4.7
F6	5.30	0.13635	96×48^3	0.063	3.0	325	5.0
F7	5.30	0.13638	96×48^3	0.063	3.0	277	4.2
G8	5.30	0.13642	128×64^3	0.063	4.0	193	4.0
N5	5.50	0.13660	96×48^3	0.050	2.4	430	5.2
N6	5.50	0.13667	96×48^3	0.050	2.4	332	4.1
O7	5.50	0.13671	128×64^3	0.050	3.2	261	4.4

Table 1: Summary of the gauge configurations used in this study. The lattice spacings have been taken from [24].

simulation speed, such as mass preconditioning (MP) [31] and domain decomposition (DD) [27]. The parameters and some properties of the configurations are listed in table 1. The lattice spacing can be obtained by relating, for instance, an experimentally determined hadron mass to its counterpart simulated using lattice QCD

$$a[\text{fm}] = \frac{a m_\Omega^{\text{lat}}}{m_\Omega^{\text{phys}}[\text{MeV}]} \hbar c \tag{40}$$

Here we use the lattice spacings from [24], which have been obtained using the Ω baryon. Figure 6 shows a graphical assessment how well our gauge ensemble reproduce the physical situation. The determination of the pion mass will be discussed in a later chapter. The physical point, to which lattice results have to be extrapolated, is indicated by an orange point. The black line in the right panel of figure 6 indicates the threshold for the rule of thumb of $m_\pi L \geq 4$, for which finitie-size effects are expected to be small [6]. The set of ensembles allows us to perform the necessary chiral extrapolation to the physical pion mass and estimate the size of finite-size and cutoff effects.

1.5 QUARK BI-LINEARS AND CURRENTS

In this work we study the axial charge of the nucleon, the electro-magnetic form factors of the nucleon, and the leading hadronic contributions to the anomalous magnetic moment of the muon. All these quantities are obtained from hadronic matrix elements, which involve vector or axial currents in the

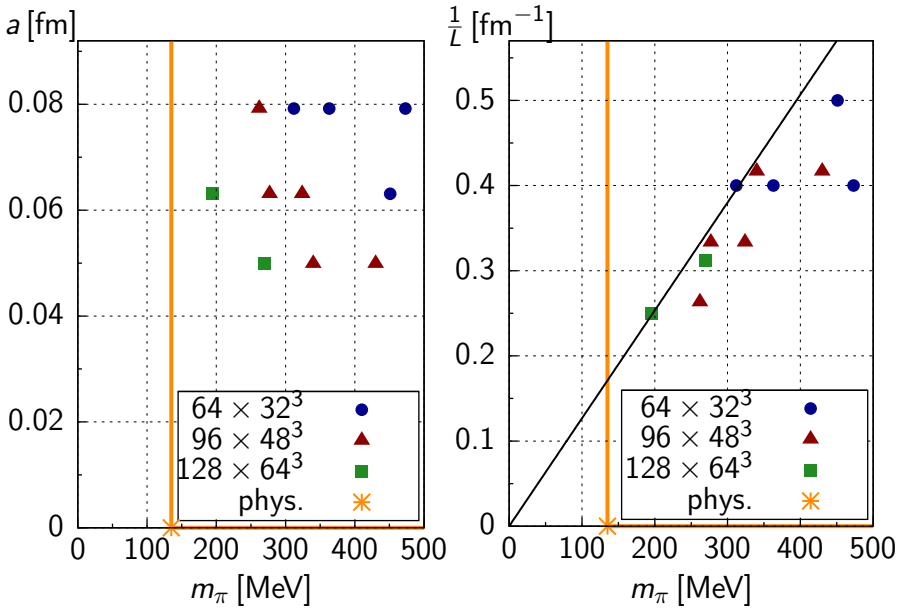

Figure 6: Overview of the gauge configurations used in this work. The orange point indicate the physical point. Left: Comparison of the lattice spacing a and the pion mass. Right: Illustration of the volumes of the ensembles. The black line shows the threshold for the rule of thumb, $m_\pi L = 4$.

necessary operators. Details of the exact definition and implementation will be discussed in a later chapter. In the case of the Wilson lattice formulation, the naïve vector current,

$$J^l_\mu(n) = \overline{\psi}(n)\,\gamma_\mu\,\psi(n), \tag{41}$$

and the local axial current

$$A_\mu(n) = \overline{\psi}(n)\gamma_\mu\gamma_5\psi(n), \tag{42}$$

are not conserved. This is a consequence of the explicit breaking of chiral symmetry by the Wilson term. Both currents can be non-perturbatively renormalised to restore the current conservation,

$$(J^l_\mu)_R(n) = Z_V(1 + b_V\, am)J^l_\mu(n), \tag{43}$$
$$(A_\mu)_R(n) = Z_A(1 + b_A\, am)A_\mu(n). \tag{44}$$

The vector current renormalisation constant Z_V has to be determined independently, for which we use the non-perturbatively obtained values in [32]. For the axial current, we use the non-perturbatively determined renormalisation constant Z_A obtained in [33]. The factors b_V and b_A are taken from a tadpole-improved estimate in [34]. Since the contribution from the quark masses are at the sub-percent level [35], the unknown systematics arising from b_V and b_A can be neglected.

With Noether's theorem, we can construct a conserved vector current for the Wilson action. The so-called *point-split vector current* can be obtained by considering the following transformations [36],

$$\psi'(n) = \mathrm{e}^{-\mathrm{i}\epsilon}\,\psi(n) \qquad \text{and} \qquad \overline{\psi}'(n) = \overline{\psi}(n)\,\mathrm{e}^{\mathrm{i}\epsilon}, \tag{45}$$

which are a symmetry of the lattice action and therefore leave the partition function Z invariant. By promoting the transformation to a local transformation,

$$\psi'(n) = \psi(n)\,(1 - \mathrm{i}\epsilon(n)) \;\text{ and }\; \overline{\psi}'(n) = \overline{\psi}(n)\,(1 + \mathrm{i}\epsilon(n))\,, \tag{46}$$

the conserved current can be derived by demanding that all additional terms in the partition function vanish,

$$0 \stackrel{!}{=} \mathrm{i}\int D[\psi,\overline{\psi}]e^{-S}\left(\sum_n\left(\frac{\partial S}{\partial\psi(n)}\epsilon(n)\psi(n) - \overline{\psi}(n)\epsilon(n)\frac{\partial S}{\partial\overline{\psi}(n)}\right)\right). \tag{47}$$

Equation (47) has to be valid for any choice of $\epsilon(n)$, which implies

$$\partial_\mu J^c_\mu(n) = \left(\frac{\partial S}{\partial\psi(n)}\psi(n) - \overline{\psi}(n)\frac{\partial S}{\partial\overline{\psi}(n)}\right) = 0, \tag{48}$$

from which the conserved vector current $J^c_\mu(n)$ can be extracted:

$$\begin{aligned} J^c_\mu(n) = \frac{1}{2}\Big(&\overline{\psi}(n+a\hat{\mu})(r+\gamma_\mu)U^+_\mu(n)\psi(n) \\ &- \overline{\psi}(n)(r-\gamma_\mu)U_\mu(n)\psi(n+a\hat{\mu})\Big). \end{aligned} \tag{49}$$

With this definition, the Ward-Takahashi identity [37, 38]

$$q_\mu\, J^c_\mu(q) = 0 \tag{50}$$

is fulfilled, which can be seen by Fourier transforming equation (48).

Although our action is non-perturbatively $\mathcal{O}(a)$ improved, hadronic matrix elements receive contributions from leading lattice artefacts, since these operators contain vector or axial currents. These current can be $\mathcal{O}(a)$ improved by adding a suitable counter-term [6],

$$J^{\mathrm{imp}}_\mu(n) = J_\mu(n) + a\,c_V\,\partial_\nu T_{\mu\nu}(n), \tag{51}$$

$$A^{\mathrm{imp}}_\mu(n) = A_\mu(n) + a\,c_A\,\partial_\mu P(n). \tag{52}$$

The coefficients c_V and c_A of the tensor $T_{\mu\nu}$ and pseudo-scalar P quark densities require an appropriate tuning to remove the leading lattice artefacts. The pseudo-scalar and the tensor operator are defined as

$$P(n) = \overline{\psi}(n)\,\gamma_5\,\psi(n), \tag{53}$$

$$T_{\mu\nu}(n) = \overline{\psi}(n)\,\gamma_\mu\gamma_\nu\,\psi(n), \tag{54}$$

Currently, we have not included the improvement terms in our calculations, but we expect cutoff effects to be small, which needs to be checked numerically.

1.6 PARTIALLY TWISTED BOUNDARY CONDITIONS

In lattice simulations, one usually imposes periodic boundary conditions

$$\psi(n + L\,\hat{e}_k) = \psi(n), \tag{55}$$

in space, and anti-periodic boundary conditions in the time direction,

$$\psi(n + T\,\hat{e}_0) = -\psi(n). \tag{56}$$

Via these conditions, the simulation box is aligned to copies of itself and forms a four-dimensional torus. With this choice of geometry, boundary effects are avoided, but the volume still needs to be sufficiently large to suppress long-ranged interactions across boundaries. By imposing periodic or anti-periodic boundary conditions, the accessible momenta in lattice simulations become discrete

$$p_k = \frac{2\pi}{L} n_k \text{ and } p_0 = \frac{2\pi}{T} n_0 \text{ with } n_\mu \in \mathbb{Z}, \tag{57}$$

which can be seen by the Fourier transform of equation (55),

$$\int \mathrm{d}^4 p\; \mathrm{e}^{-\mathrm{i}p\left(n+L\,\hat{k}\right)}\; \widetilde{\psi}(p) = \int \mathrm{d}^4 p\, e^{-\mathrm{i}pn}\; \widetilde{\psi}(p). \tag{58}$$

Equation (57) shows that the accessible momenta are related to the geometry of the simulation box, and that even with today's lattice sizes the smallest non-zero momentum is around $200 - 300\,\mathrm{MeV}$. The discrete momentum spectrum limits the calculation of momentum dependent quantities such as form factors.

Modified boundary conditions, so called *twisted boundary conditions*, have been proposed in [39–41],

$$\psi(n + L\,\hat{e}_k) = \mathrm{e}^{\mathrm{i}\Theta_k}\,\psi(n), \tag{59}$$

which adds a phase-shift to the quarks at the boundaries of the lattice. It can be shown that twisted boundary conditions are equivalent to modifying the covariant derivative,

$$\widetilde{D}_k = D_k + i\frac{\Theta_k}{L}, \tag{60}$$

which implies that the momentum of the quark-propagator is changed to

$$p_i = \frac{2\pi n_i}{L} + \frac{\Theta_i}{L}. \tag{61}$$

The momentum can be controlled by the 'twist angles' Θ_k and tuned to, in principle, any value. The quark fields ψ can be redefined,

$$\psi(n) = \mathrm{e}^{\mathrm{i}\frac{\Theta_k}{L} n_k} \widetilde{\psi}(n), \tag{62}$$

such that periodic boundary conditions are fulfilled by the new fields $\widetilde{\psi}(n)$. Twisted boundary conditions can be achieved by inserting equation (62) into the action,

$$a^4 \sum_n \Big[\overline{\widetilde{\psi}}(n) e^{\mathrm{i}\frac{\Theta_k}{L}} U_k(n)(r-\gamma_k)\widetilde{\psi}(n+k) + \overline{\widetilde{\psi}}(n) e^{-\mathrm{i}\frac{\Theta_k}{L}} U_k^\dagger(n-k)(r+\gamma_k)\widetilde{\psi}(n+k)\Big], \tag{63}$$

where the phases cancel exactly, except in the spatial hopping part of the action. With these definitions, twisted boundary conditions can be practically implemented by the transformation

$$U_k(n) \to \mathrm{e}^{\mathrm{i}\frac{\Theta_k}{L}} U_k(n). \tag{64}$$

The gluonic part of the action remains unchanged, since the transformations cancel in closed gauge loops. *Partially* twisted boundary conditions can be achieved by applying the twist only to the valence quarks in the simulation. Partial twisting of the valence quarks adds a finite-size effect to the simulation, which however is expected to be exponentially suppressed [41].

Part II

FORM FACTORS OF THE NUCLEON

2

INTRODUCTION

Measurements at SLAC in 1969 [42] have first shown that the proton is not a point-like particle, and today we know that the proton and neutron consist of quarks bound by gluons. Understanding the composition of protons and neutrons in terms of the distribution of charge and momentum from a purely theoretical approach is clearly desirable and allows QCD to be tested. In this part, we will present a lattice calculation of the axial charge and the electromagnetic form factors of the nucleon. This is the first step in a wider program for computing quantities, which describe structural properties of hadrons. The aim of such calculations is a first principle calculation of hadron structure observables, which are difficult to measure in experiments.

Experimentally, the electric and magnetic structure of protons and neutrons can be probed by scattering experiments with electrons. The electron is an ideal candidate, since it is an elementary particle and the electro-magnetic interaction is understood very well. The elastic differential cross-section of an electron interacting with an extended spin-$\frac{1}{2}$ target can be expressed by the the Rosenbluth separation formula [43]

$$\left(\frac{d\sigma}{d\Omega}\right) \sim \left(\frac{G_E^2(Q^2) + \tau G_M^2(Q^2)}{1+\tau} + 2\tau G_M^2(Q^2) \tan^2\frac{\Theta}{2}\right), \tag{65}$$

with

$$\tau = \frac{Q^2}{4m_N}. \tag{66}$$

The functions $G_E(Q^2)$ and $G_M(Q^2)$ are the electric and magnetic Sachs form factors, which contain information about the electro-magnetic charges inside a hadron. The electric form factor $G_E(Q^2)$, for example, can be interpreted as the Fourier transform of the electric charge distribution,

$$G_E(Q^2) = \int \mathrm{e}^{i\vec{q}\vec{r}}\rho(r)\,\mathrm{d}r. \tag{67}$$

Recent measurements, for example, at MAMI [44] in Mainz, have determined the Sachs form factors $G_E(Q^2)$ and $G_M(Q^2)$ very precisely. Figure 7 shows

the ratio of $G_E(Q^2)$ over the "standard" dipole parametrisation, from which the mean square radius

$$\langle r^2 \rangle = -\frac{6}{G(0)} \frac{\partial G(Q^2)}{\partial Q^2}\bigg|_{Q^2=0} \tag{68}$$

can be extracted from the slope at the origin. More details about the experimental determination can be found in [44]. Measurements using muonic hydrogen [45] lead to a discrepancy larger than 5σ for the radius of the proton compared to the world average in [46].

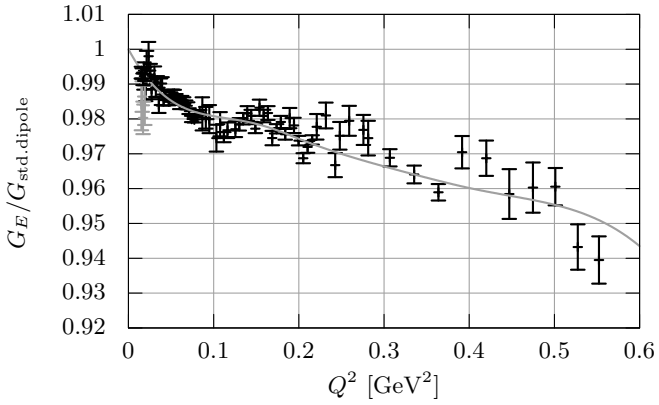

Figure 7: Experimental determination of $G_E(Q^2)$ taken from [44].

The axial charge g_A, technically the ratio of the axial and vector charges g_A/g_V, probes the inner structure of proton and neutron via the weak interaction. It can be measured precisely using the neutron beta decay [47], which leads to:

$$g_A = 1.2701(25). \tag{69}$$

At the Lattice conference in 2013, Syritsyn presented an overview of hadron structure calculations using lattice QCD [48]. The nucleon axial charge, shown in figure 8, is determined by various lattice collaborations [35, 48–70], where the lattice results typically show a tendency for underestimating the axial charge by $5-10\%$. In addition, the chiral behaviour provides no explanation of this discrepancy. Only recently, lattice results seem to agree with the phenomenology once a proper treatment of the contamination from excited states is taken into account. The axial charge of the nucleon can be considered a benchmark quantity for lattice calculations [35]: The hadronic matrix element can be computed by a simple fermion bi-linear without derivatives. The initial and final states are at rest, which normally leads to a good statistical signal. Moreover, disconnected diagrams cancel in the case of iso-vector quantities such as the axial charge.

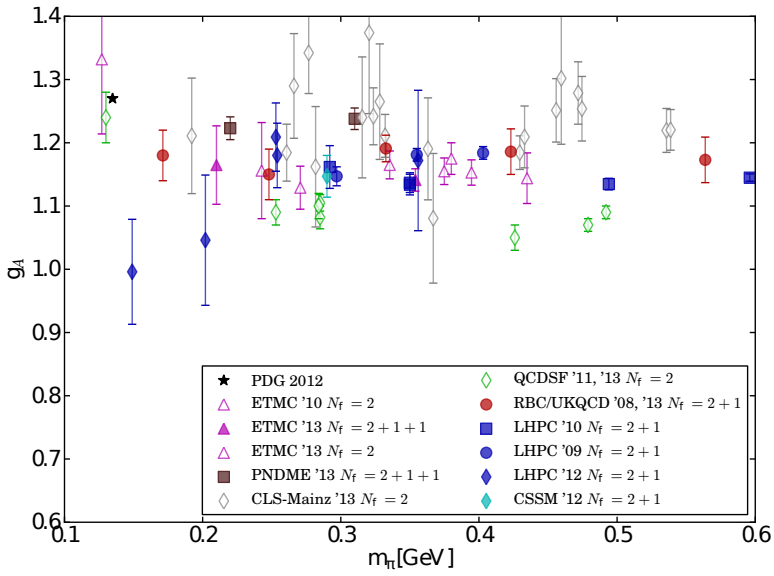

Figure 8: Compilation of lattice data for the nucleon axial charge taken from [48].

In lattice calculations, the electro-magnetic form factors are more commonly written in terms of the Dirac and Pauli form factors $F_1(Q^2)$ and $F_2(Q^2)$, which are related to the Sachs form factors via

$$G_E(Q^2) = F_1(Q^2) - \frac{Q^2}{4m_N^2} F_2(Q^2), \qquad (70)$$
$$G_M(Q^2) = F_1(Q^2) + F_2(Q^2).$$

Figure 9 shows a compilation of results for the Pauli radius r_1 computed by different lattice groups [48, 71–77], and a similar discrepancy as for the axial charge is seen in the majority of lattice simulations. The anomalous magnetic moment of the nucleon κ in figure 10 shows better agreement with the experimental determination. A thorough study of all systematic uncertainties such as contamination from excited states, lattice artefacts, and finite-size effects is needed to obtain a reliable estimate of structure properties of the nucleon.

The average quark momentum fraction of the nucleon, $\langle x \rangle_{u-d}$, is another quantity, which is considered as a benchmark quantity for lattice calculation, since it can be directly computed from a ratio of three- and two point functions at vanishing momentum transfer, which involves one derivative in the corresponding three-point function. Figure 11 shows a compilation of $\langle x \rangle_{u-d}$ determined by various lattice collaborations [48, 58, 61, 64, 78–83]. At the moment, most lattice calculation tend to overestimate the average quark momentum fraction of the nucleon.

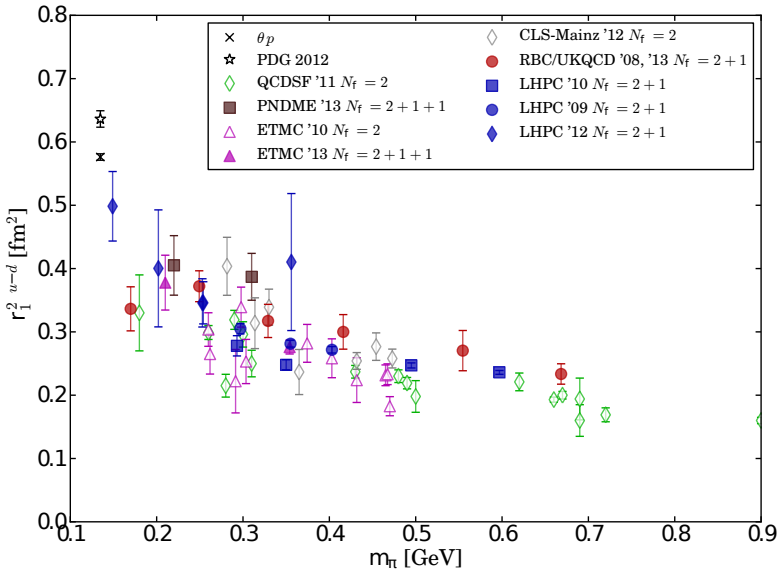

Figure 9: Compilation of lattice r_1 calculations taken from [48].

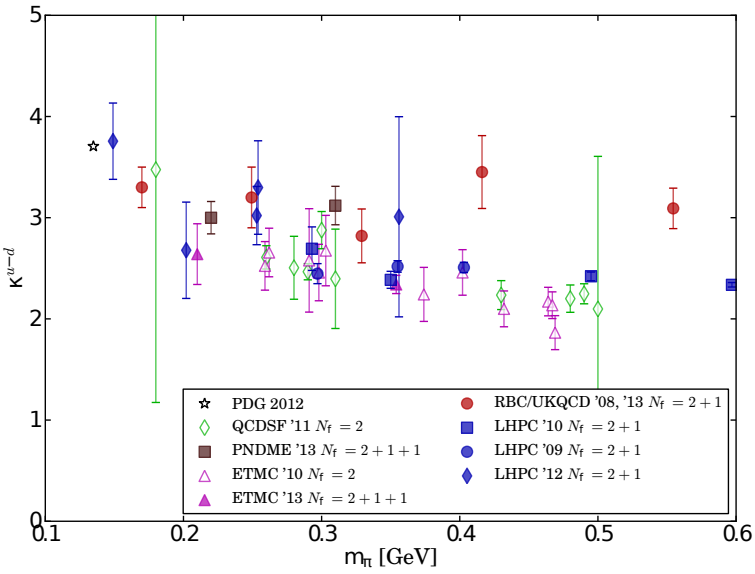

Figure 10: Compilation of lattice data for the anomalous magnetic moment of the nucleon taken from [48].

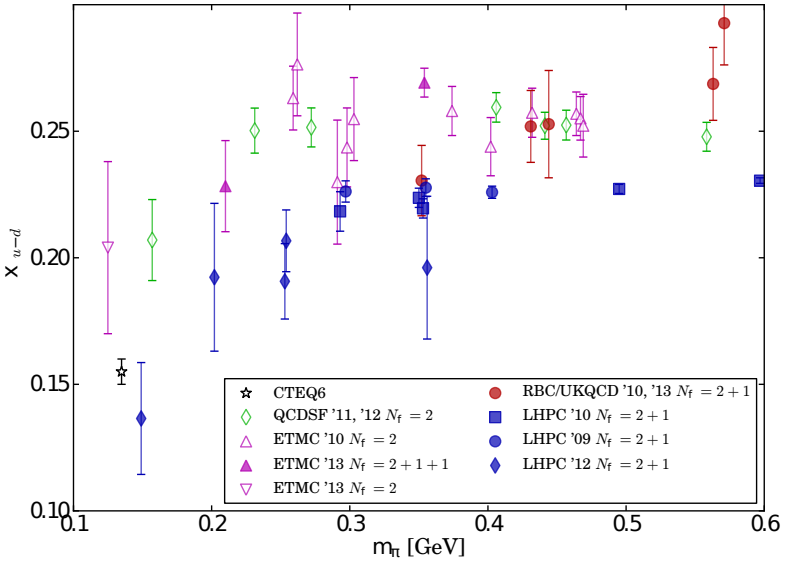

Figure 11: Overview over lattice calculations of the average quark momentum fraction of the nucleon taken from [48].

3

LATTICE CALCULATION

We present in the following the necessary steps for the computation of the axial charge g_A and the electro-magnetic form factors G_E and G_M of the nucleon using lattice QCD. Each of these quantities can be extracted from a ratio of three-point and two-point functions.

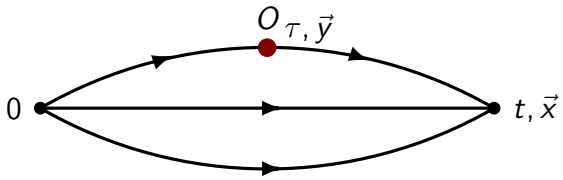

Figure 12: Schematic of a three-point function with a generic operator O at the insertion point $(\tau, \vec{y})$.

Figure 12 shows a generic three-point function of the nucleon with an operator O inserted at $(\tau, \vec{y})$. Depending on the choice of the operator, we are able to extract different matrix elements. For the choice of the conserved electro-magnetic vector current (compare section 1.5),

$$O = J^c_\mu(x) = \frac{1}{2}\Big(\overline{\psi}(x + a\hat{\mu})(r + \gamma_\mu)U^+_\mu(x)\psi(x) - \overline{\psi}(x)(r - \gamma_\mu)U_\mu(x)\psi(x + a\hat{\mu})\Big), \tag{71}$$

the hadronic matrix element can be decomposed into the Pauli $F_1(Q^2)$ and Dirac $F_2(Q^2)$ form factors in the following way:

$$\left\langle p', s' \right| J^c_\mu \left| p, s \right\rangle = \overline{u}(p, s)\left(\gamma_\mu F_1(Q^2) + \mathrm{i}\sigma_{\mu\nu}\frac{Q_\nu}{2m}F_2(Q^2)\right)u(p, s). \tag{72}$$

The functions $F_1(Q^2)$ and $F_2(Q^2)$ depend solely on the momentum transfer Q^2, which is given by

$$Q^2 = -\left(E_{p'} - E_p\right)^2 + (\vec{p}' - \vec{p})^2. \tag{73}$$

The Pauli and Dirac form factors can be related to the electric and magnetic Sachs form factors via equation (70). These form factors contain information about the electric charge,

$$G_E(0) = 1, \tag{74}$$

and the magnetic moment,

$$G_M(0) = \mu, \tag{75}$$

of the nucleon. The electric charge of the proton in equation (74) can be used to test our implementation of the operators. If we use the local vector current,

$$O = J^l_\mu(x) = \overline{\psi}(x)\gamma_\mu\psi(x), \tag{76}$$

instead of the conserved vector current $J^c_\mu(x)$, we can determine the renormalisation constant Z_V of the local vector current by taking a ratio of

$$Z_V = \frac{\left\langle p', s' \right| J^l_\mu \left| p, s \right\rangle}{\left\langle p', s' \right| J^c_\mu \left| p, s \right\rangle}. \tag{77}$$

If we choose the local axial current for the operator O,

$$O = A_\mu(x) = \overline{\psi}(x)\gamma_\mu\gamma_5\psi(x), \tag{78}$$

we can extract the axial form factor $G_A(Q^2)$ and the induced pseudoscalar form factor $G_P(Q^2)$ from

$$\begin{aligned} &\left\langle p', s' \right| A_\mu \left| p, s \right\rangle = \\ &\overline{u}(p,s)\left(\gamma_\mu\gamma_5 G_A^{\text{bare}}(Q^2) + \gamma_5\frac{Q_\mu}{2m}G_P^{\text{bare}}(Q^2)\right)u(p,s), \end{aligned} \tag{79}$$

up to a necessary renormalisation of the current. The axial charge of the nucleon can be obtained from the axial form factor at vanishing momentum transfer

$$G_A(0) = g_A. \tag{80}$$

In the next sections, we will present details of the computation the axial charge and the electro-magnetic form factors, which can be extracted from ratios of three- and two-point functions. We start with the two-point function of the pion, which is the most simple quantity in lattice simulations.

3.1 TWO-POINT FUNCTION OF THE PION

The mass of a particle can be obtained by studying the Euclidean time dependence of a two-point correlation functions. We choose an interpolating field of

$$P(x) = \overline{d}(x)\,\gamma_5\,u(x), \tag{81}$$

which has the quantum numbers and flavour content of a pseudoscalar meson [6] and allows us to construct the correlation function

$$C_2^\pi(\vec{p},t) = \left\langle P(t,\vec{x})\,\overline{P}(0)\right\rangle \tag{82}$$

by creating a pion at the origin 0 and annihilating it at $(t,\vec{x})$. A schematic view of such a correlation function is displayed in figure 13.

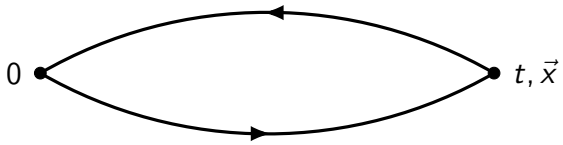

Figure 13: Schematic of the two-point function of the pion

Including the projection to a definite spatial momentum $\vec{p}$, we can relate the two-point correlation function to a product of two propagators

$$\begin{aligned} C_2^\pi(\vec{p},t) &= \sum_{\vec{x}} \mathrm{e}^{\mathrm{i}\vec{p}\,\vec{x}}\left\langle P(t,\vec{x})\,\overline{P}(0)\right\rangle = \sum_{\vec{x}} \mathrm{e}^{\mathrm{i}\vec{p}\,\vec{x}}\left\langle \overline{d}(x)\gamma_5 u(x)\overline{u}(0)\gamma_5 d(0)\right\rangle \\ &= \sum_{\vec{x}} \mathrm{e}^{\mathrm{i}\vec{p}\,\vec{x}}\left(\overline{d_\alpha^a}(x)(\gamma_5)_{\alpha\beta}u_\beta^a(x)\overline{u_\gamma^b}(0)(\gamma_5)_{\gamma\delta}d_\delta^b(0)\right) \\ &= \sum_{\vec{x}} \mathrm{e}^{\mathrm{i}\vec{p}\,\vec{x}}\left((\gamma_5)_{\alpha\beta}S_u(x,0)^{ab}_{\beta\gamma}(\gamma_5)_{\gamma\delta}S_d(0,x)^{ba}_{\delta\alpha}\right) \\ &= \sum_{\vec{x}} \mathrm{e}^{\mathrm{i}\vec{p}\,\vec{x}}\left(S(x,0)^{ab}_{\alpha\beta}\,S^\dagger(x,0)^{ba}_{\beta\alpha}\right). \end{aligned} \tag{83}$$

Equation (83) is the starting point for our implementation, where in the last step the γ_5-hermiticity $S(0,x) = \gamma_5 S^\dagger(x,0)\gamma_5$ has been used to write everything explicitly in terms of the point-to-all propagator $S(0,x)$. Looking at the two-point function on a hadronic level, we can study the Euclidean time dependence by inserting a complete set of states $1 = \sum_n |n\rangle\langle n|$ and using the translation operator, $P(x) = \mathrm{e}^{\mathrm{i}px}P(0)\,\mathrm{e}^{-\mathrm{i}px}$,

$$\begin{aligned} C_2^\pi(\vec{p},t) &= \left\langle P(t,\vec{x})\,\overline{P}(0)\right\rangle = \sum_n \left\langle 0\middle|P\middle|n\right\rangle\left\langle n\middle|P^\dagger\middle|0\right\rangle \mathrm{e}^{-E_n(\vec{p})\,t} \\ &= A_0\,\mathrm{e}^{-E_0(\vec{p})\,t} + A_1\,\mathrm{e}^{-E_1(\vec{p})\,t} + \ldots \underset{t\to\infty}{=} A_0\,\mathrm{e}^{-E_0(\vec{p})\,t}. \end{aligned} \tag{84}$$

The interpolating field $P(x)$ creates, in addition to the pion, excited states, which have the same quantum numbers as the interpolating operator. Equation (84) shows that excited states with larger energies ($E_0 < E_1 < \ldots$) decay more quickly than the ground state, so that after a sufficiently large time separation t only the term proportional to $E_0(\vec{p})$ remains. The coefficient $\left\langle 0\middle|P\middle|n\right\rangle$ determines the projection of the operator P with a particular state n to the vacuum. We use a finite simulation box with anti-periodic boundary condi-

tions in time, so that the backward propagating part of the pion needs to be included, which leads to

$$A_0\,\mathrm{e}^{-E_0(\vec{p})t} + A_0\,\mathrm{e}^{-E_0(\vec{p})(T-t)} = 2A_0\,\mathrm{e}^{-E_0(\vec{p})\frac{T}{2}}\cosh\left(\left(\frac{T}{2}-t\right)E_0(\vec{p})\right). \tag{85}$$

We consider the following ratio of two-point functions in order to extract the ground state,

$$\frac{C_2^\pi(\vec{p},t)}{C_2^\pi(\vec{p},t+1)} = \frac{\cosh\left(aE_{\mathrm{eff}}(\vec{p})\left(t-\frac{T}{2}\right)\right)}{\cosh\left(aE_{\mathrm{eff}}(\vec{p})\left(t+1-\frac{T}{2}\right)\right)}, \tag{86}$$

which we solve numerically for the effective energy $aE_{\mathrm{eff}}(\vec{p})$.

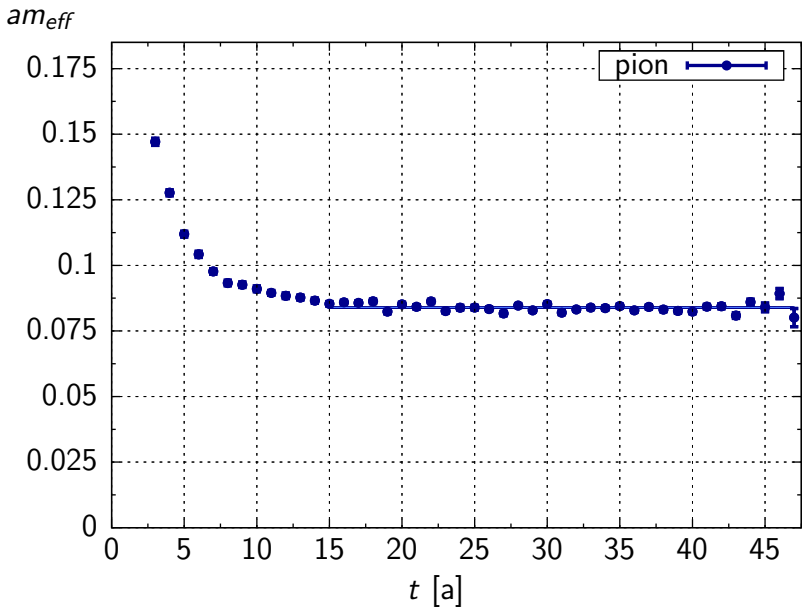

Figure 14: Effective mass of the pion measured on the N6 ensemble

The effective mass $am_{\mathrm{eff}} = aE_{\mathrm{eff}}(\vec{0})$ determined on the N6 ensemble is shown in figure 14 using a "smeared" interpolating operator at source and sink. Details of the smearing procedure will follow in a later section. A constant fit to the effective mass, starting at timeslice $t = 15$, results in a very precise (2‰) estimate of the pion mass

$$am_\pi = 0.08390(16). \tag{87}$$

The statistical error is obtained using 1000 bootstrap samples in the uncorrelated fit.

3.2 TWO-POINT FUNCTION OF THE NUCLEON

With an appropriate interpolating operator,

$$N_\alpha(x) = \epsilon_{abc}\left(u^a_\beta(x)(C\gamma_5)_{\beta\gamma}\,d^b_\gamma(x)\right)u^c_\alpha(x), \tag{88}$$

we can construct the two-point function of the nucleon similarly as for the pion. Schematically this is shown in figure 15, where the nucleon is created at the origin and annihilated at $(t, \vec{x})$.

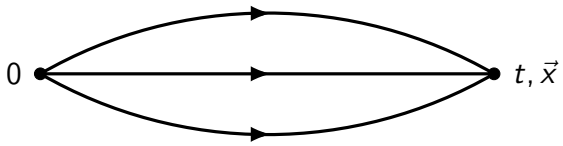

Figure 15: Schematic of the two-point function of the nucleon

The matrix C in equation (88) is the charge conjugation matrix, which can be written in terms of Dirac matrices, $C = \mathrm{i}\gamma_0\gamma_2$. Note that the interpolating operator of the nucleon $N_\alpha(x)$ has an open Dirac index, which we will use to project to the correct parity. In this work, we choose

$$\Gamma = \frac{1}{4}\left(1+\gamma_0\right)\left(1+\mathrm{i}\gamma_5\gamma_3\right). \tag{89}$$

With these definitions, we can construct the nucleon two-point function and express it in terms of point-to-all propagators:

$$\begin{aligned} C_2^N(\vec{p},t) &= \sum_{\vec{x}} \mathrm{e}^{\mathrm{i}\vec{p}\,\vec{x}}\Gamma_{\alpha\beta}\Big\langle N_\alpha(t,\vec{x})\,\overline{N}_\beta(0)\Big\rangle \\ &= -\sum_{\vec{x}} \mathrm{e}^{\mathrm{i}\vec{p}\,\vec{x}}\epsilon_{abc}\,\epsilon_{def}\left(u^a_\gamma(x)(C\gamma_5)_{\gamma\delta}\,d^b_\delta(x)\right)u^c_\alpha(x)\,\Gamma_{\alpha\beta}\times \\ &\qquad\qquad \overline{u^d_\beta}(0)\left(\overline{d^e_\epsilon}(0)(C\gamma_5)_{\epsilon\kappa}\,\overline{u^f_\kappa}(0)\right) \\ &= -\sum_{\vec{x}} \mathrm{e}^{\mathrm{i}\vec{p}\,\vec{x}}\epsilon_{abc}\,\epsilon_{def}\,\Gamma_{\alpha\beta}\,(C\gamma_5)_{\gamma\delta}\,(C\gamma_5)_{\epsilon\kappa}\,S_d(x,0)^{be}_{\delta\epsilon}\times \\ &\qquad\qquad \left(S_u(x,0)^{af}_{\gamma\kappa}\,S_u(x,0)^{cd}_{\alpha\beta} - S_u(x,0)^{ad}_{\gamma\beta}\,S_u(x,0)^{cf}_{\alpha\kappa}\right). \end{aligned} \tag{90}$$

As for the pion, the two-point function of the nucleon can be expanded by inserting a complete set of states $1 = \sum_{n,s}|n,s\rangle\langle n,s|$ and applying the translation operator:

$$\begin{aligned} C_2^N(\vec{p},t) &= \sum_{\vec{x}} \mathrm{e}^{\mathrm{i}\vec{p}\,\vec{x}}\Gamma_{\alpha\beta}\Big\langle N_\alpha(t,\vec{x})\,\overline{N}_\beta(0)\Big\rangle \\ &= \sum_{n,s}\Big\langle 0\Big|N\Big|n,s\Big\rangle\Big\langle n,s\Big|N^\dagger\Big|0\Big\rangle\,\mathrm{e}^{-E_n(\vec{p})\,t} \\ &= A_0\,\mathrm{e}^{-E_0(\vec{p})\,t} + A_1\,\mathrm{e}^{-E_1(\vec{p})\,t} + \ldots \underset{t\to\infty}{=} A_0\,\mathrm{e}^{-E_0(\vec{p})\,t}. \end{aligned} \tag{91}$$

The matrix element $\Big\langle 0\Big|N\Big|n,s\Big\rangle$ can be expressed in terms of a Dirac spinor u, the energies E and an a priori unknown factor Z,

$$\Big\langle 0\Big|N\Big|n,s\Big\rangle = \frac{Z}{\sqrt{2E(\vec{p})}}u(p,s). \tag{92}$$

The effective energy can be obtained by a ratio of the correlation function at different Euclidean times,

$$a\,E_{\text{eff}}(\vec{p}) = \ln\left(\frac{C(t)}{C(t+1)}\right). \tag{93}$$

In a finite simulation box, the nucleon propagating backwards in time corresponds to the parity partner of the nucleon, N^*, which has a different Euclidean time behaviour.

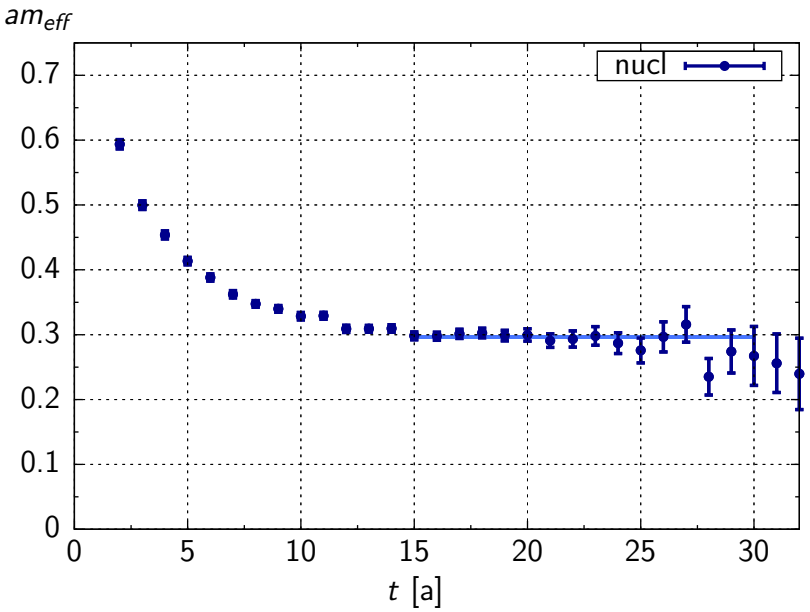

Figure 16: Effective mass of the nucleon measured on the N6 ensemble

Figure 16 shows the effective mass of the nucleon computed on the N6 ensemble using a smeared interpolating operator at source and sink. For small Euclidean times, excited states are still visible but die out quickly, so that a constant fit, starting at $t = 15$, results in

$$am_N = 0.2972(29). \tag{94}$$

For large Euclidean times, the error grows significantly, in fact exponentially. This can be understood by looking at the variance of the nucleon correlator

$$\sigma_N^2 \sim \left\langle (C_2^N)^\dagger (C_2^N) \right\rangle - \left\langle C_2^N \right\rangle^2. \tag{95}$$

The first term of equation (95) corresponds to a product of three forward- and three backward-propagators, which can be combined to three pions. The combined mass of the pions is smaller than the one of the nucleon, so that the signal-to-noise ratio decays exponentially,

$$\frac{\left\langle C_2^N \right\rangle}{\sigma_N} \sim \mathrm{e}^{-(m_N - \frac{3}{2}m_\pi)t}. \tag{96}$$

Similar considerations for the pion channel reveal that the signal-to-noise ratio remains constant as t is increased.

3.3 THREE-POINT FUNCTION OF THE NUCLEON

The hadronic matrix element can be extracted from a three-point function with the operator inserted at $(\tau, \vec{y})$, which is illustrated in figure 12. With the appropriate momentum projection, we can write the nucleon three-point function as

$$\begin{aligned} C_3(O, \vec{q}, \vec{p}, \tau, t_s) &= \sum_{\vec{x},\vec{y}} \mathrm{e}^{-\mathrm{i}\vec{q}\vec{y}}\, \mathrm{e}^{-\mathrm{i}\vec{p}\vec{x}} \Gamma_{\alpha\beta} \Big\langle N_\alpha(t_s, \vec{x})\, O(\tau, \vec{y})\, \overline{N}_\beta(0) \Big\rangle \\ &= \sum_{s,s'} \mathrm{e}^{-E_n \tau}\, \mathrm{e}^{-E_n (t_s - \tau)} \Big\langle 0 \Big| N \Big| p', s' \Big\rangle \Big\langle p', s' \Big| O(q) \Big| p, s \Big\rangle \Big\langle p, s \Big| N^\dagger \Big| 0 \Big\rangle. \end{aligned} \tag{97}$$

In the last step of equation (97), we have twice inserted a complete set of states and used the translation operator. The three-point function $C_3(O, \vec{p}', \vec{p}, \tau, t_s)$ is directly proportional to the matrix element highlighted in red. We build ratios of three- and two-point functions to remove the unknown overlap with the vacuum and the Euclidean time dependence. These ratios will be discussed in a later section. At the quark level, we have to distinguish between the operator inserted on a u- or d-quark line,

$$O^u(\tau, \vec{y}) = \overline{u^a_\alpha}(y) O^{ab}_{\alpha\beta}\, u^b_\beta(y) \text{ and } O^d(\tau, \vec{y}) = \overline{d^a_\alpha}(y) O^{ab}_{\alpha\beta}\, d^b_\beta(y). \tag{98}$$

Although we use degenerate light flavours, the Wick contractions with the operator are different. For the operator inserted onto a d-quark line, we obtain

$$\begin{aligned} &\Gamma_{\alpha\beta} \Big\langle N_\alpha(t_s, \vec{x})\, O^d(\tau, \vec{y})\, \overline{N}_\beta(0) \Big\rangle \\ &= -\Gamma_{\alpha\beta}\, \epsilon_{abc}\, \epsilon_{def} \Big(u^a_\gamma(x) (C\gamma_5)_{\gamma\delta}\, d^b_\delta(x) \Big)\, u^c_\alpha(x) \times \\ &\qquad \overline{d^g_\lambda}(y) O^{gl}_{\lambda\mu} d^l_\mu(y)\, \overline{u^d_\beta}(0) \Big(\overline{d^e_\epsilon}(0) (C\gamma_5)_{\epsilon\kappa}\, \overline{u^f_\kappa}(0) \Big) \\ &= -\Gamma_{\alpha\beta}\, \epsilon_{abc}\, \epsilon_{def} (C\gamma_5)_{\gamma\delta} (C\gamma_5)_{\epsilon\kappa} O^{gl}_{\lambda\mu} \times \\ &\qquad \Big(S_u(x,0)^{af}_{\gamma\kappa}\, S_d(x,y)^{bg}_{\delta\lambda}\, S_d(y,0)^{le}_{\mu\epsilon}\, S_u(x,0)^{cd}_{\alpha\beta} \\ &\qquad + S_u(x,0)^{ad}_{\gamma\beta}\, S_d(x,y)^{bg}_{\delta\lambda}\, S_d(y,0)^{le}_{\mu\epsilon}\, S_u(x,0)^{cf}_{\alpha\kappa} \Big). \end{aligned} \tag{99}$$

If we insert the operator onto a u-quark line, we have to perform more Wick contractions, which lead to

$$\begin{aligned} &\Gamma_{\alpha\beta} \Big\langle N_\alpha(t_s, \vec{x})\, O^u(\tau, \vec{y})\, \overline{N}_\beta(0) \Big\rangle \\ &= -\Gamma_{\alpha\beta}\, \epsilon_{abc}\, \epsilon_{def} \Big(u^a_\gamma(x) (C\gamma_5)_{\gamma\delta}\, d^b_\delta(x) \Big)\, u^c_\alpha(x) \times \\ &\qquad \overline{u^g_\lambda}(y) O^{gl}_{\lambda\mu} u^l_\mu(y)\, \overline{u^d_\beta}(0) \Big(\overline{d^e_\epsilon}(0) (C\gamma_5)_{\epsilon\kappa}\, \overline{u^f_\kappa}(0) \Big) \\ &= -\Gamma_{\alpha\beta}\, \epsilon_{abc}\, \epsilon_{def} (C\gamma_5)_{\gamma\delta} (C\gamma_5)_{\epsilon\kappa} O^{gl}_{\lambda\mu} \times \\ &\qquad \Big(S_d(x,0)^{be}_{\delta\epsilon}\, S_u(x,y)^{ag}_{\gamma\lambda}\, S_u(x,0)^{cd}_{\alpha\beta}\, S_u(y,0)^{lf}_{\mu\kappa} \\ &\qquad + S_d(x,0)^{be}_{\delta\epsilon}\, S_u(x,y)^{ag}_{\gamma\lambda}\, S_u(x,0)^{cf}_{\alpha\kappa}\, S_u(y,0)^{ld}_{\mu\beta} \\ &\qquad - S_d(x,0)^{be}_{\delta\epsilon}\, S_u(x,y)^{cg}_{\alpha\lambda}\, S_u(x,0)^{ad}_{\gamma\beta}\, S_u(y,0)^{lf}_{\mu\kappa} \\ &\qquad - S_d(x,0)^{be}_{\delta\epsilon}\, S_u(x,y)^{ag}_{\gamma\lambda}\, S_u(x,0)^{af}_{\gamma\kappa}\, S_u(y,0)^{ld}_{\mu\beta} \Big). \end{aligned} \tag{100}$$

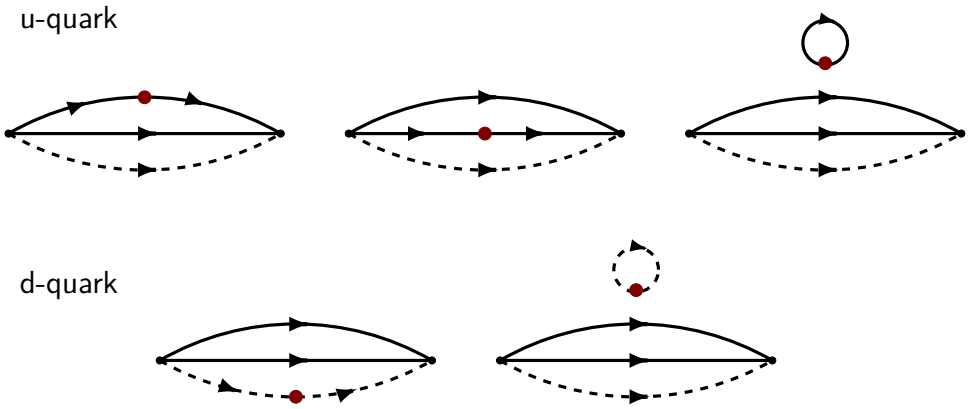

Figure 17: Schematic of the Wick contractions contributing to the nucleon three-point function in the case of a u-type operator (upper panel) and a d-type operator (lower panel). The dotted line indicates a d-quark, the solid line a u-quark.

Figure 17 shows a pictorial representation of the Wick contractions in equations (99) and (100). Disconnected diagrams cancel exactly in the case of iso-vector quantities

$$C_3 := C_3^u - C_3^d \tag{101}$$

with two degenerate light flavours and are already omitted in equations (99) and (100). These equations contain a propagator, $S(x, y)$, from the operator insertion point to the sink. The computation of such an all-to-all propagator is a numerically demanding task, therefore two methods have been proposed to avoid the computation of the all-to-all propagator: either fix the sink [84] or fix the operator [85]. Both methods are sketched in figure 18. The ETMC collaboration has explored in [86] the possibility of computing the all-to-all propagator by a stochastic estimate, which leads to a compatible precision in the three point function.

Figure 18: Computation of the extended propagator (blue) using a fixed sink (left) or a fixed operator (right). The green lines depict the source for the additional inversion.

For a fixed-operator method, one uses a point-to-all propagator and contracts it with the operator at the fixed time τ. This combination is used as source for a new inversion, which provides the extended propagator. Once computed, the location of the operator is fixed, and any additional operator or insertion time

τ requires a new inversion. For the nucleon three-point function the extended propagator needs to be contracted with two standard propagators at the sink t. The position of the sink $(t, \vec{x})$ and the projector Γ can be chosen freely for the fixed-operator method. We intend to study a large set of operators, so it is advantageous to use the fixed-sink method, which is achieved by the four generic steps:

1. Compute point-to-all propagator $S(x, 0)$,
2. Construct nucleon source at t_s,
3. Determine extended propagator $\Sigma_{u,d}(0, y, t_s, \vec{p})$,
4. Combine standard and extended propagator with the operator at τ.

A schematic of these four steps is shown in figure 19.

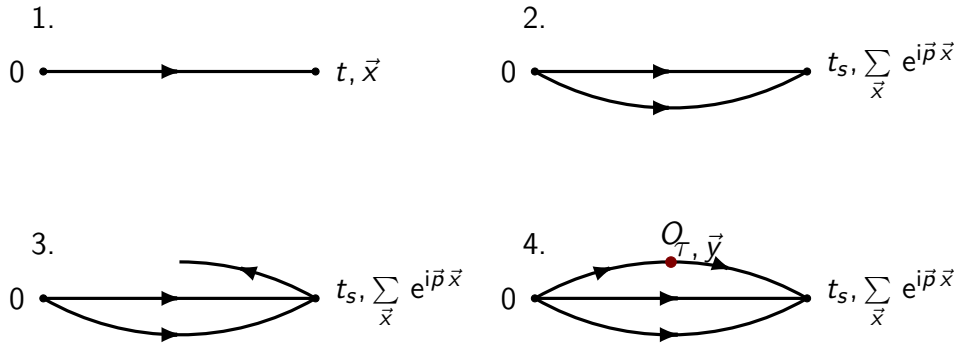

Figure 19: Schematic of the four steps of computing the three-point function of the nucleon.

The disadvantages of the fixed-sink method are that for each source-sink separation t_s and projector Γ we need to perform a new inversion. The extended propagator for a d-type source can be defined as [84]

$$\Sigma_d(0, y, t_s, \vec{p})^{lm}_{\lambda\mu} = -\Gamma_{\alpha\beta}\,\epsilon_{abc}\,\epsilon_{dle}(C\gamma_5)_{\gamma\delta}\,(C\gamma_5)_{\epsilon\lambda}\times \sum_{\vec{x}} e^{-i\vec{p}\vec{x}} S(x, y)^{bm}_{\delta\mu}\left(S(x, 0)^{ad}_{\gamma\epsilon}\,S(x, 0)^{ce}_{\alpha\beta} - S(x, 0)^{ae}_{\gamma\beta}\,S(x, 0)^{cd}_{\alpha\epsilon}\right). \tag{102}$$

For a u-quark, the extended propagator is defined as

$$\begin{aligned}\Sigma_u(0, y, t_s, \vec{p})^{lm}_{\lambda\mu} = &-\Gamma_{\alpha\beta}\,\epsilon_{abc}\,(C\gamma_5)_{\gamma\delta}\sum_{\vec{x}} e^{-i\vec{p}\vec{x}} S(x, y)^{be}_{\delta\epsilon}\times \\ &\Big[\epsilon_{lde}\,(C\gamma_5)_{\lambda\epsilon}\left(S(x, 0)^{am}_{\gamma\mu}\,S(x, 0)^{ce}_{\alpha\beta} - S(x, 0)^{ae}_{\gamma\beta}\,S(x, 0)^{cm}_{\alpha\mu}\right) \\ &+ \epsilon_{del}\,(C\gamma_5)_{\kappa\epsilon}\,\delta_{\beta\lambda}\Big(S(x, 0)^{ad}_{\gamma\kappa}\,S(x, 0)^{cm}_{\alpha\mu} - S(x, 0)^{am}_{\gamma\mu}\,S(x, 0)^{cd}_{\alpha\kappa}\Big)\Big].\end{aligned} \tag{103}$$

The extended propagator can be computed by similar numerical techniques that are used to obtain the "standard" point-to-all propagator $S(x, 0)$,

$$\sum_y D(x, y)^{ab}_{\alpha\beta}\,S(y, z)^{bc}_{\beta\gamma} = \delta^{ac}\delta_{\alpha\gamma}\delta_{z0}. \tag{104}$$

For the d-type source, we need to solve,

$$\sum_y \Sigma_d(0,y,t_x,\vec{p})^{xy}_{\rho\sigma} D(y,z)^{yz}_{\sigma\tau} = -\Gamma_{\alpha\beta}\,\epsilon_{azc}\,\epsilon_{dxe}(C\gamma_5)_{\gamma\tau}(C\gamma_5)_{\epsilon\rho}\times \sum_{\vec{z}} \mathrm{e}^{-\mathrm{i}\vec{p}\vec{z}}\left(S(z,0)^{ad}_{\gamma\epsilon}\,S(z,0)^{ce}_{\alpha\beta} - S(z,0)^{ae}_{\gamma\beta}\,S(z,0)^{cd}_{\alpha\epsilon}\right)\delta_{t_s t_z}, \tag{105}$$

in order to obtain the extended propagator $\Sigma_d(0,y,t_x,\vec{p})^{xy}_{\rho\sigma}$. The computation for the u-quark is analogous and straightforward, by replacing the right hand side of equation (105) with the source of equation (103). With the extended propagator, the three-point function of the nucleon can be computed directly using

$$C_3^{u,d}(O,\vec{q},\vec{p},\tau,t_s) = \sum_{\vec{y}} \mathrm{e}^{-\mathrm{i}\vec{q}\vec{y}}(\gamma_5)_{\alpha\beta}\,\Sigma^{\dagger}_{u,d}(0,y,t_s,\vec{p})^{ab}_{\beta\gamma}\,(\gamma_5)_{\gamma\delta}\,O^{bc}_{\delta\epsilon}\,S(x,0)^{ca}_{\epsilon\alpha}. \tag{106}$$

3.4 SMEARING

Point-like sources typically yield a poor overlap onto the ground state, so we apply the so-called *Jacobi / Gaussian smearing* [87–89] to improve the projection properties of the interpolating operators onto the ground state. The smearing procedure allows us to maximise the spectral weight of the ground state (compare equations (84) and (91)) and reduce contamination from excited states at early Euclidean times. Since the correlation function of the nucleon shows an exponentially decaying signal-to-noise ratio, an improvement at small Euclidean times allows us to extract the nucleon mass from a much longer plateau, which leads to a more reliable estimate of the nucleon mass. In addition, we use APE [90] smeared spatial links,

$$V_k(x) = (1-\alpha)U_k(x) + \frac{\alpha}{6}\sum_{l\neq k}\times \left(U_l(x)U_k(x+\hat{l})U_l^{\dagger}(x+\hat{k}) + U_l^{\dagger}(x-\hat{l})U_k(x-\hat{l})U_l(x-\hat{l}+\hat{k})\right), \tag{107}$$

which are constructed from perpendicular staples of the old gauge links. The updated gauge field $V_k(x)$ must be projected back to $SU(3)$, since these fields are not an element of $SU(3)$. Instead of using a point source in the inversion of the Dirac operator,

$$\sum_y D(x,y)^{ab}_{\alpha\beta}\,S(y,z)^{bc}_{\beta\gamma} = \delta^{ac}\delta_{\alpha\gamma}\delta_{z0}, \tag{108}$$

we apply a Gaussian smearing kernel of the form

$$M(x,y)^{ab}_{\alpha\beta} := \left(\delta_{\alpha\beta}\delta^{ab}\delta_{y,x} + \kappa\sum_k \times \left(V_k(x)^{ab}\,\delta_{\alpha\beta}\,\delta_{y,x+\hat{k}} + V_k^{\dagger}(x-\hat{k})^{ab}\,\delta_{\alpha\beta}\,\delta_{y,x-\hat{k}}\right)\right)^n \tag{109}$$

to the point source and perform an inversion to obtain the "smeared" propagator $\widetilde{S}(x,0)$,

$$\sum_y D(x,y)^{ab}_{\alpha\beta}\,\widetilde{S}(y,z)^{bc}_{\beta\gamma} = M(z,v)^{ae}_{\alpha\epsilon}\,\delta^{ec}\delta_{\epsilon\gamma}\delta_{v0}. \tag{110}$$

The smearing matrix $M(x,y)$ iteratively builds an extended, gauge-invariant object, that has a better overlap with the ground state of the hadron of interest. Still the smearing procedure remains a heuristic procedure, which achieves an improved interpolating operator with fewer excited-state contributions. Figure 20 shows the result of such a source on a particular configuration of the N6 ensemble.

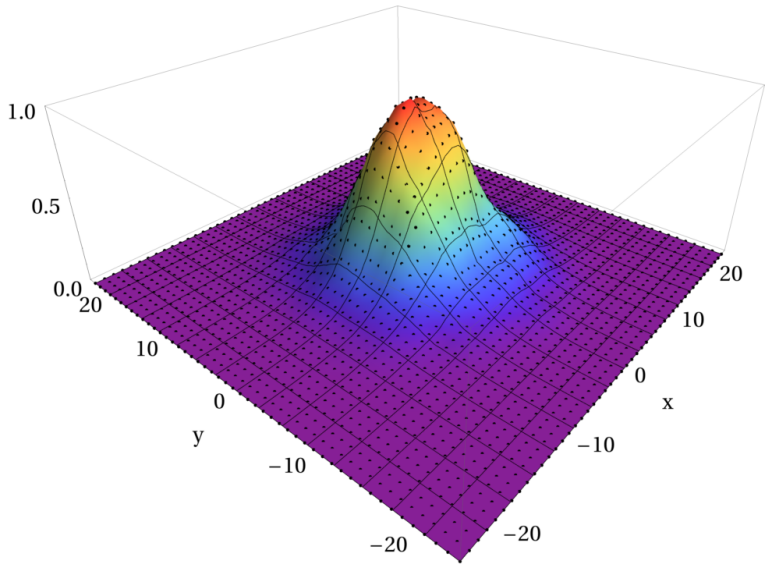

Figure 20: The shape of a smeared source on the N6 ensemble.

In addition to the smearing of the source, we apply the smearing kernel to the propagators at the sink,

$$\widetilde{S'}(x,z)^{ac}_{\alpha\gamma} = M(x,y)^{ab}_{\alpha\beta}\,\widetilde{S}(y,z)^{bc}_{\beta\gamma}. \tag{111}$$

In this way, we achieve a symmetric smearing procedure at the source and sink, which results in identical overlap coefficient in the three-point functions. The parameters κ and n in the smearing kernel $M(x,y)$ influence the size and shape of the "Gaussian" profile, and should be tuned to achieve a best overlap with the ground state. We have chosen different values for the ensembles to achieve a good compromise between the statistical accuracy and the length of the effective mass plateau of a nucleon. A comparison of smeared and point sources can be seen in figure 21, where we show the effective mass of the nucleon computed on the N6 ensemble with 100 configurations. The improvement for small Euclidean times can be clearly seen, which allows us to extract the effective mass from a longer plateau. The reduction of excited

states becomes even more important when we consider three-point functions, in which excited states contribute from the source and the sink. In [91, 92], we have generalised the smearing procedure to produce anisotropic shapes, which show a reduction of the statistical uncertainties, when correlation functions with non-vanishing momentum transfer are studied. In [93, 94], we have extended the smearing of the source to an arbitrary wave function and have studied the influence of the gauge fields on the shapes generated with the iterative smearing. Both methods have not yet been applied to our computations of the form factors, but suggest a further reduction of excited states.

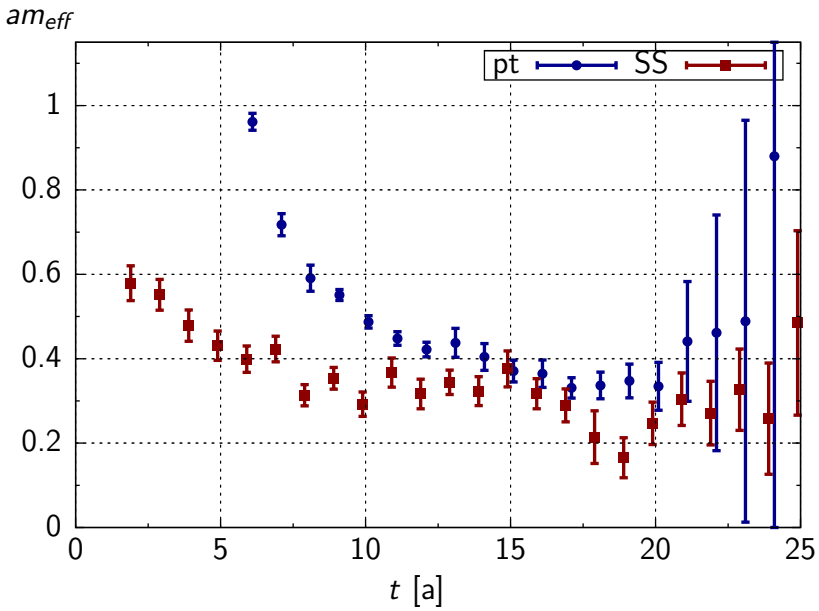

Figure 21: Comparison of the nucleon effective mass computed using a smeared-smeared (SS) or a point-point (pt) correlator. The result is determined using 100 decorrelated N6 configurations.

3.5 RATIOS

The hadronic matrix element can be extracted, as shown before, from the nucleon three-point function

$$C_3(O, \vec{q}, \vec{p}, \tau, t_s) = \sum_{s,s'} \mathrm{e}^{-E_n \tau}\, \mathrm{e}^{-E_n (t_s - \tau)} \left\langle 0 \middle| N \middle| p', s' \right\rangle \left\langle p', s' \middle| O(q) \middle| p, s \right\rangle \left\langle p, s \middle| N^\dagger \middle| 0 \right\rangle. \tag{112}$$

We build ratios of three- and two-point functions, as suggested in [95, 96],

$$R_O(\vec{q}, \tau, t_s) = \frac{C_3(O, \vec{q}, \vec{0}, \tau, t_s)}{C_2(\vec{0}, t_s)} \sqrt{\frac{C_2(\vec{q}, t_s - \tau) C_2(\vec{0}, \tau) C_2(\vec{0}, t_s)}{C_2(\vec{0}, t_s - \tau) C_2(\vec{q}, \tau) C_2(\vec{q}, t_s)}} \tag{113}$$

to cancel the time and energy dependence as well as the remaining overlap factors Z. We compute the three-point function with vanishing momentum at the sink, $\vec{p} = 0$, so that the momentum transfer is directly given by the momentum inserted at the operator $\vec{q}$. For sufficiently large separations of the source, sink, and the operator insertion point, the ratio becomes the matrix element of interest. Any remaining dependence on the operator insertion time τ and source-sink separation t_s outside the statistical accuracy corresponds to contaminations from excited states, which have not been removed by the ratio R and can be parametrised as

$$R_O(\vec{q}, \tau, t_s) = R_O^0(\vec{q}) \times \left(1 + \mathcal{O}(\mathrm{e}^{-\Delta\tau}) + \mathcal{O}(\mathrm{e}^{-\Delta(t_s-\tau)}) + \mathcal{O}(\mathrm{e}^{-\Delta t_s})\right). \tag{114}$$

If we evaluate

$$\frac{m}{2E(p)E(p')} \frac{\langle \Gamma(-\mathrm{i}\not{p}' + m)\, O\, (-\mathrm{i}\not{p} + m)\rangle}{\sqrt{\langle \Gamma(-\mathrm{i}\not{p}' + m)\rangle \langle \Gamma(-\mathrm{i}\not{p} + m)\rangle}} \tag{115}$$

for our choice of the projector, as shown in [77, 97],

$$\Gamma = \frac{1}{4}\,(1 + \gamma_0)\,(1 + \mathrm{i}\gamma_5\gamma_3)\,, \tag{116}$$

the bare nucleon axial charge is given by

$$\mathrm{Im}\, R_{\gamma_5\gamma_3}(\vec{q} = \vec{0}, \tau \gg 1, t_s \gg 1) = g_A^{\mathrm{bare}}. \tag{117}$$

We use the non-perturbatively determined renormalisation constant Z_A obtained in [33] and the improvement term b_A from a tadpole-improved estimate from [34], as discussed in section 1.5,

$$g_A = Z_A(1 + b_A m_q)\, g_A^{\mathrm{bare}}. \tag{118}$$

The electro-magnetic form factors can be extracted from

$$\mathrm{Re}\, R_{\gamma_0}(\vec{q}, \tau \gg 1, t_s \gg 1) = \sqrt{\frac{M+E}{2E}} F_1(Q^2) \tag{119}$$

and

$$\mathrm{Re}\, R_{\gamma_i}(\vec{q}, \tau \gg 1, t_s \gg 1) = \epsilon_{ij} p_j \sqrt{\frac{1}{2E(E+M)}} G_M(Q^2), \tag{120}$$

which are related to the remaining form factors by

$$F_2(Q^2) = G_M(Q^2) - F_1(Q^2), \tag{121}$$

$$G_E(Q^2) = F_1(Q^2) - \frac{Q^2}{4m_N^2} F_2(Q^2). \tag{122}$$

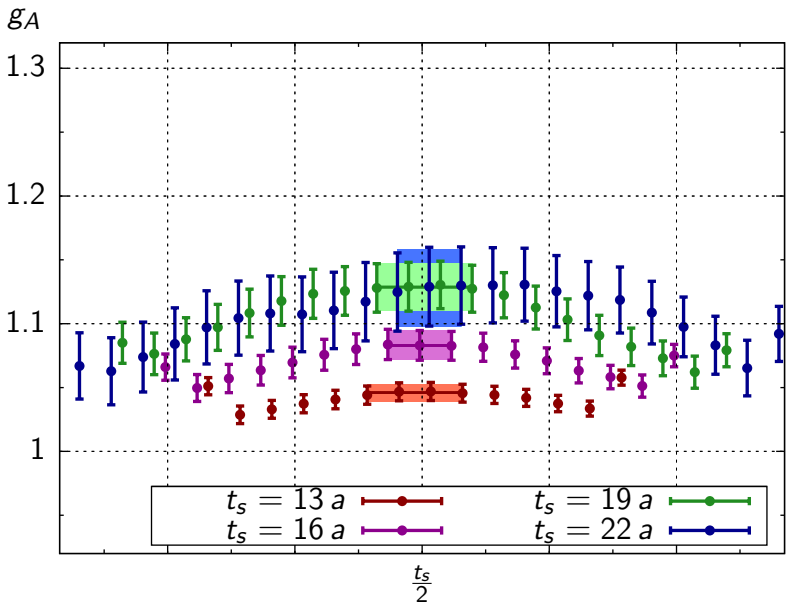

Figure 22: Ratio of the nucleon axial charge for four values of t_s on the N6 ensemble. The values have been shifted symmetrically around $\frac{t_s}{2}$ and include a constant fit to the central part of the plateau.

The renormalisation of the vector current is exactly 1, since we use the conserved vector current in the definition of the operator.

Figure 22 shows the ratio of the nucleon axial charge g_A, computed on the N6 ensemble, for four different source-sink separations t_s (0.65 fm, 0.80 fm, 0.95 fm and 1.1 fm). A small τ and t_s dependence remains, which indicates the presence of excited states. Unfortunately, we cannot extend the source-sink separation any further, since the exponential error growth shows large statistical fluctuation for larger t_s.

3.6 EXCITED STATES

On all our ensembles, we see a similar pattern as in figure 22, which indicates that contributions from excited states are still present. Therefore it cannot be guaranteed that the results for the axial charge do not suffer from a systematic bias. One possible strategy to deal with this problem is a fit ansatz including the expected excited states contribution to fit all four source-sink separations jointly [98],

$$f(\tau, t_s) = G + A\,\mathrm{e}^{-\Delta\tau} + B\,\mathrm{e}^{-\Delta(t_s-\tau)} + C\,\mathrm{e}^{-\Delta t_s}. \tag{123}$$

We assume that the energy gap is dominated by twice the pion mass $\Delta = 2m_\pi$, which will be the largest contribution close to the physical pion mass. We find that such a fit, shown in figure 23 for the axial charge computed on the N6

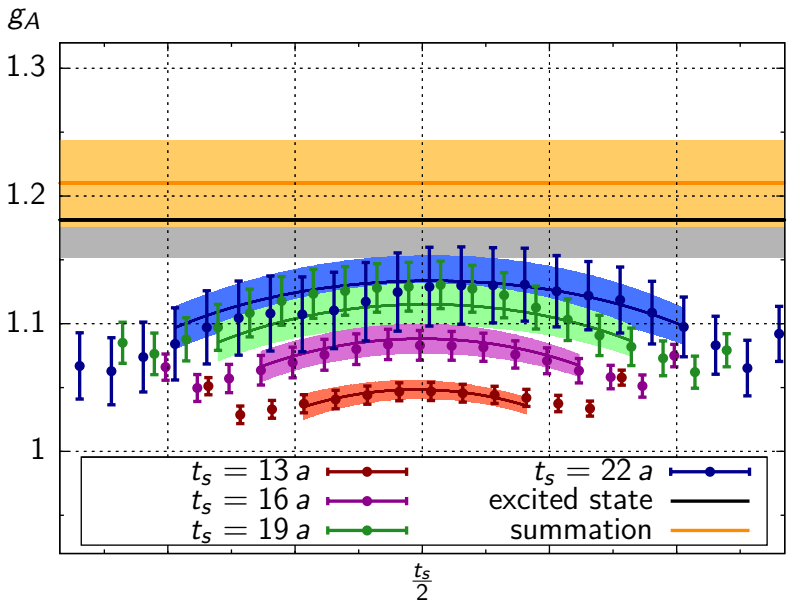

Figure 23: Combined excited-state fit to the different ratios on the N6 ensemble. The solid black and orange lines shows the extracted asymptotic values for g_A using the combined excited-state fit and the summed operator insertion method, respectively.

ensemble, provides a good description of the data points and leads to a higher estimate for the axial charge, which is shown in figure 23 by the grey band. In [35], we have used another strategy to include excited states, the so-called *summed operator insertion method* [87, 99, 100], which we will refer to as "summation method". We sum the ratio R over the full range of the operator insertion times τ, excluding points with potential contact terms, and so we get

$$S_O(\vec{q}, t_s) = \sum_{\tau=1}^{t_s-1} R_O(\vec{q}, \tau, t_s) \to c + t_s \cdot (G + \mathcal{O}(\mathrm{e}^{-\Delta t_s})). \tag{124}$$

With this approach, we suppress excited states further, since t_s is larger than τ or $t_s - \tau$. The asymptotic estimate of the ground state G can be extracted from the slope of a linear fit, which is shown for the axial charge on the N6 ensemble in figure 24. The divergent constant c contains contribution from contact terms and is not relevant for the determination of the asymptotic value. The fit in figure 24 shows a remarkably good description of the data and confirms the leading linear behaviour. The result from the summation method for the axial charge is added to figure 23 as an orange band, which agrees with the value obtained by the excited state fit within the statistical uncertainties. The fit results have been listed in table 2 for completeness. On the N6 ensemble, we have added two larger source sink separations (1.25 fm and 1.40 fm) to check the excited state fit and the summation method. The data for the larger source-sink separation has been omitted in figure 23, since the

large statistical uncertainties would obscure the other data. Although the statistical uncertainties grow significantly, we see the tendency toward the fitted values. Higher estimates for g_A are obtained, when excited states contributions are included in the fit function, or when the summed operator insertion technique is applied, where the latter has parametrically reduced contributions from excited states by construction.

	$t_s = 13\,a$	$t_s = 16\,a$	$t_s = 19\,a$	$t_s = 22\,a$
g_A	1.046(7)	1.083(11)	1.129(18)	1.128(30)
	$t_s = 25\,a$	$t_s = 28\,a$	excited	summation
g_A	1.142(45)	1.178(80)	1.181(30)	1.210(34)

Table 2: Fit results of the axial charge on the individual plateaus, the combined excited state fit and the summation method.

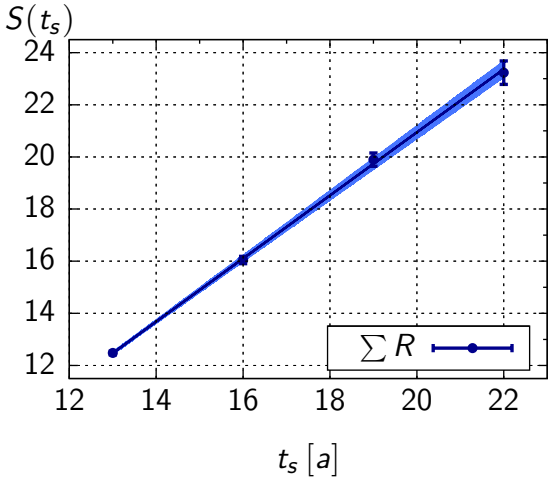

Figure 24: Summed operator insertion method applied to the axial charge on the N6 ensemble.

Higher statistical accuracy exposes contributions from excited states. The statistical precision of the individual data points should to be sufficient large to disentangle the influence of excited states. Figure 25 shows a comparison of the axial charge on the F7 ensemble for an older calculation [35] with a total number of 1000 measurements and updated results for the same ratio using in total 3000 measurements. In our recent determination, we could not see signs of excited-state contaminations, as statistical fluctuations did obscure the trend in the source sink separation. With the new analysis, we see a clear separation of the individual values of t_s, which indicates contamination from excited states. The comparison in figure 25 serves as a warning: insufficient

statistics may lead to the wrong conclusion regarding excited state contamination.

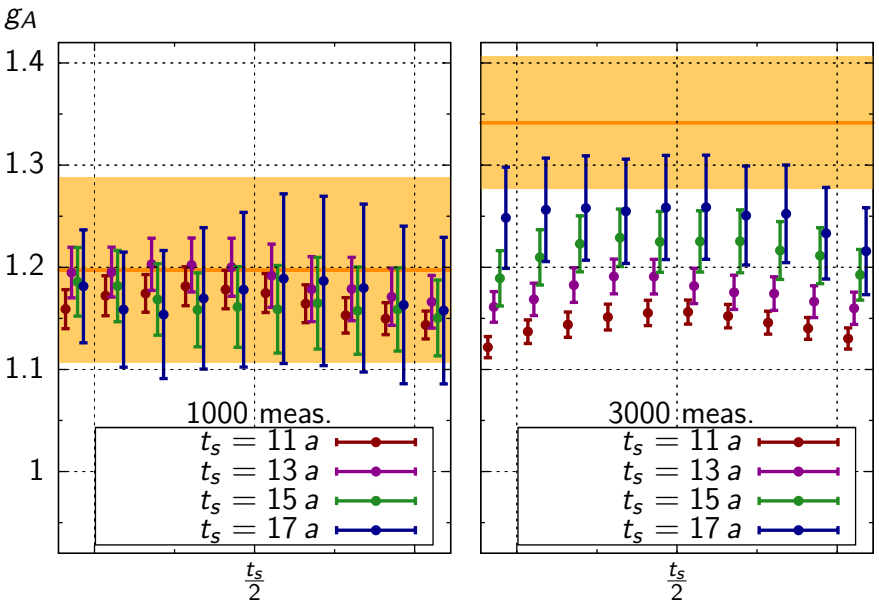

Figure 25: Left: 1000 measurements of the axial charge on the F7 ensemble. Right: 3000 measurements on the same setup.

3.7 MOMENTUM DEPENDENCE

In order to extract the momentum dependence of the form factors, we compute the ratio of three- and two-point functions for a set of momenta. The accessible range of $\vec{q}$ are multiples of $\frac{2\pi}{L}$, since we are using periodic boundary conditions. The final momentum transfer can be computed using the dispersion relation for the energy,

$$E(p) = \sqrt{\left(\frac{2\pi}{L} n_i\right)^2 + m_N^2}. \tag{125}$$

With this, the momentum transfer can be computed using

$$Q^2 = -\left(E(p) - m_N\right)^2 + \left(\frac{2\pi}{L} n_i\right)^2. \tag{126}$$

Figure 26 shows the plateau values for $F_1(Q^2)$ for the different momenta computed on the N6 ensemble. The plateau values corresponds to a source-sink separation of $t_s = 22\,a$, which is equivalent to 1.1 fm. We fit the momentum dependence by a dipole ansatz,

$$G(Q^2) = \frac{G(0)}{\left(1 + \left(\frac{Q}{M}\right)^2\right)^2}, \tag{127}$$

with two parameters $G(0)$ and M. A similar fit ansatz is commonly used in the experimental determination [101]. Figures 27 and 28 show a comparison of dipole fits for $G_E(Q^2)$ or $G_M(Q^2)$ on the N6 ensemble using the values from the plateau and summation method. For illustration, an experimental parametrisation [101] is added to the plot. The summation method produces smaller estimates for $G_E(Q^2)$, which are closer to Kelly's parametrisation of the experimental data. It is important to note that the pion mass of the N6 ensemble is larger than the physical value, so that we do not expect agreement with the curve. From the fit parameter M we can extract the electric / magnetic radius,

$$\langle r^2 \rangle = -\frac{6}{G(0)} \frac{\partial G(Q^2)}{\partial Q^2}\bigg|_{Q^2=0} = \frac{12}{M^2}. \tag{128}$$

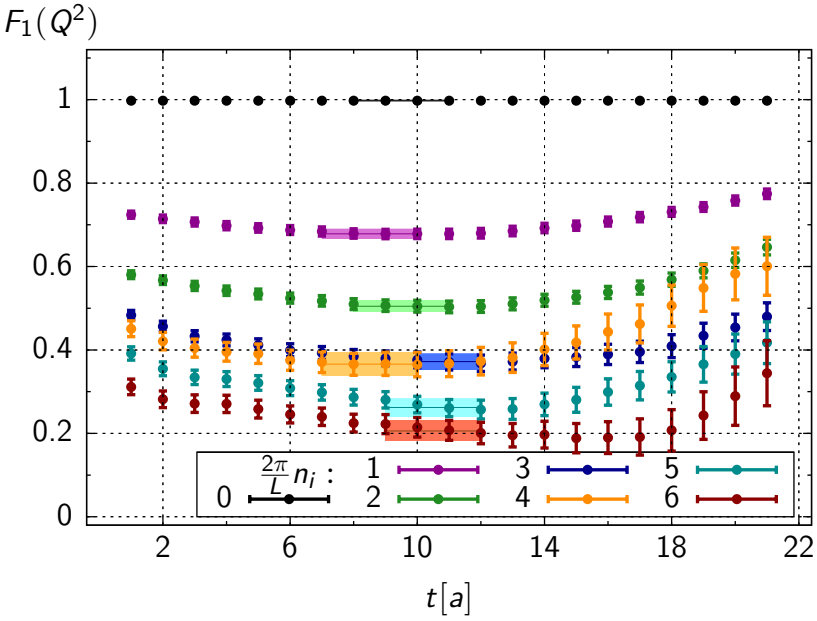

Figure 26: Momentum behaviour of the $F_1(Q^2)$ plateaus computed on the N6 ensemble. The plateaus are shown for the source sink-separation of $t_s = 22\,a$ only.

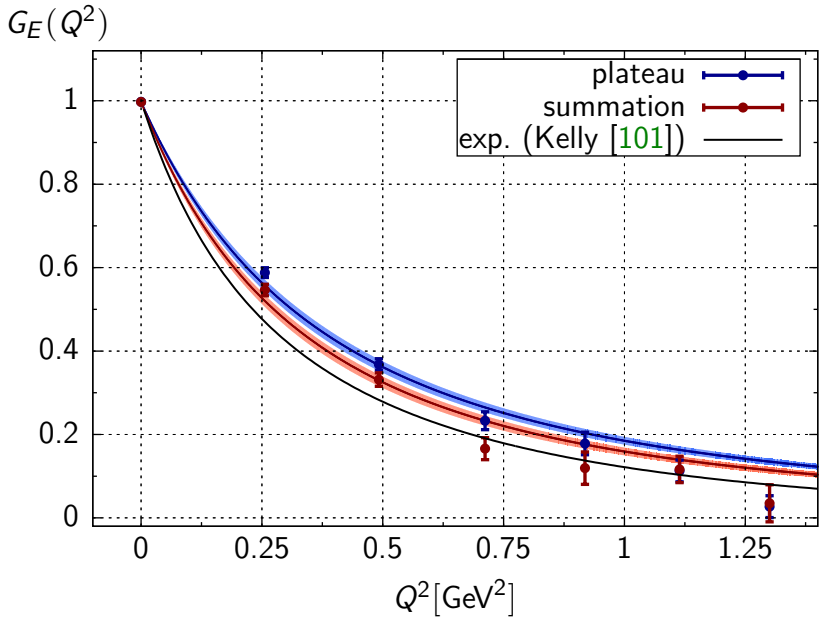

Figure 27: Dipole fit for $G_E(Q^2)$ on the N6 ensemble using the plateau (blue) and summation method (red). The black line shows an experimental parametrisation [101].

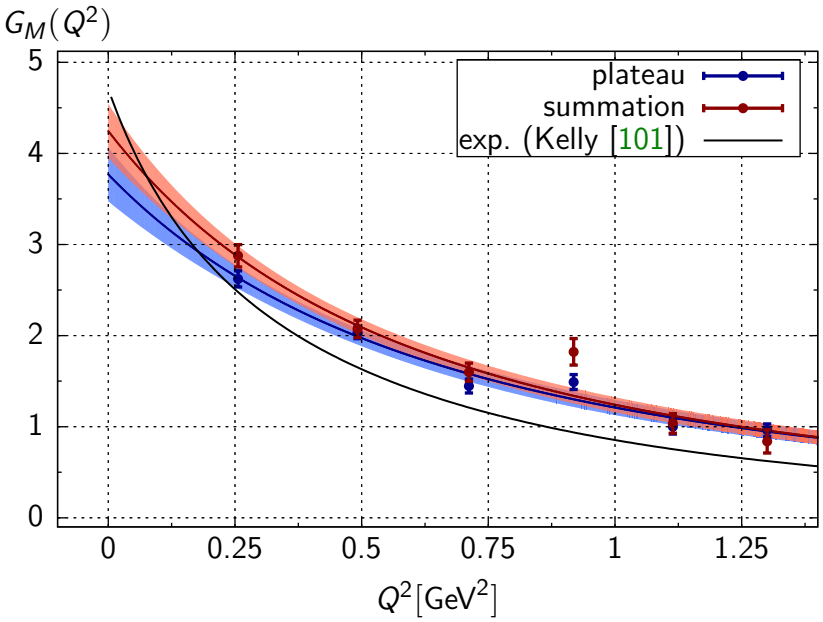

Figure 28: Dipole fit for $G_M(Q^2)$ on the N6 ensemble using the plateau (blue) and summation method (red). The black line shows an experimental parametrisation [101].

4

THE AXIAL CHARGE OF THE NUCLEON

We present results for the axial charge of the nucleon computed on the CLS gauge configurations, which we use to perform the chiral extrapolation and address the remaining lattice uncertainties such as the cutoff and finite-size effects. The input parameters and further details of the ensembles used in this study can be found in table 3. We use the volume corrections computed in *Heavy Baryon Chiral perturbation Theory* (HBChPT) [60, 102], which are for our ensemble in the subpercent level [35]. The upper panel of figure 29 shows the results for the axial charge of the nucleon using the summed operator insertion method, whereas the results from the plateau fits, are shown in the middle panel of figure 29. The results for the axial charge are listed in table 4for completeness. The ratio of the summation method and plateaus fits is shown in the lower part of figure 29, which demonstrates that including contributions from excited states lead to a statistical significant shift. We find clear evidence that the inclusion of excited states via the summation method leads to better agreement with the experimental determination of the axial charge. The values extracted from the plateau method show a significantly smaller value, although we use in most cases the largest available source-sink separation for g_A. For comparison, our results from [35] have been added in grey, which have been obtained with a smaller number of "measurements" and on ensembles with larger pion masses.

4.1 CHIRAL BEHAVIOUR

We have to extrapolate to the physical point, since all our simulations have been performed with an unphysical pion mass. We see a mild dependence on the pion mass in figure 29, so we choose the following set of functions for the chiral extrapolation, which are similar to the ones used in [35]:

Fit A: $g_A(m_\pi) = A$,

Fit B: $g_A(m_\pi) = A + B\, m_\pi^2$,

Fit C: $g_A(m_\pi) = A + B\, m_\pi^2 - C\, m_\pi^2 \ln(\frac{m_\pi^2}{\Lambda^2})$,

Fit D: HBChPT (compare appendix) [102, 103].

Label	a [fm]	m_π [MeV]	smearing (n, κ)	t_s [a]	# meas.
A3	0.079	473	$(120, 0.74)$	10, 12, 14, 16	2128
A4	0.079	363	$(120, 0.74)$	10, 12, 14, 16	3200
A5	0.079	312	$(120, 0.74)$	10, 12, 14, 16	4000
B6	0.079	267	$(120, 0.74)$	10, 12, 14, 16	2544
E5	0.063	456	$(140, 0.74)$	11, 13, 15, 17	4000
F6	0.063	325	$(140, 0.74)$	11, 13, 15, 17	3600
F7	0.063	277	$(140, 0.74)$	11, 13, 15, 17	3000
G8	0.063	193	$(140, 0.74)$	11, 13, 15, 17	4176
N5	0.050	430	$(170, 0.74)$	13, 16, 19, 22	1908
N6	0.050	332	$(170, 0.74)$	13, 16, 19, 22	3784
O7	0.050	261	$(170, 0.74)$	13, 16, 19, 22	1960

Table 3: Summary of lattice and input parameters for the calculation of the axial charge and the electro-magnetic form factors.

Label	a [fm]	m_π [MeV]	$g_A^{\text{plat.}}$	$g_A^{\text{sum.}}$
A3	0.079	473	1.210(26)	1.275(49)
A4	0.079	363	1.157(30)	1.185(80)
A5	0.079	312	1.162(45)	1.231(97)
B6	0.079	267	1.186(43)	1.288(83)
E5	0.063	456	1.191(35)	1.242(50)
F6	0.063	325	1.222(36)	1.240(45)
F7	0.063	277	1.252(49)	1.338(65)
G8	0.063	193	1.176(70)	1.208(91)
N5	0.050	430	1.142(23)	1.180(27)
N6	0.050	332	1.119(30)	1.201(34)
O7	0.050	261	1.097(37)	1.179(46)

Table 4: Result for the axial charge of the nucleon extracted using a plateau fit or the summed operator insertion method.

These fit ansätze are commonly used for the chiral extrapolation of the axial charge of the nucleon. In addition, we apply cuts on the pion mass to check our chiral extrapolations. Figure 30 shows a comparison of Fit B for the complete pion mass range and a cut of $m_\pi < 365\,\text{MeV}$, which agree very well within the statistical precision. The overall agreement between the data and the fit

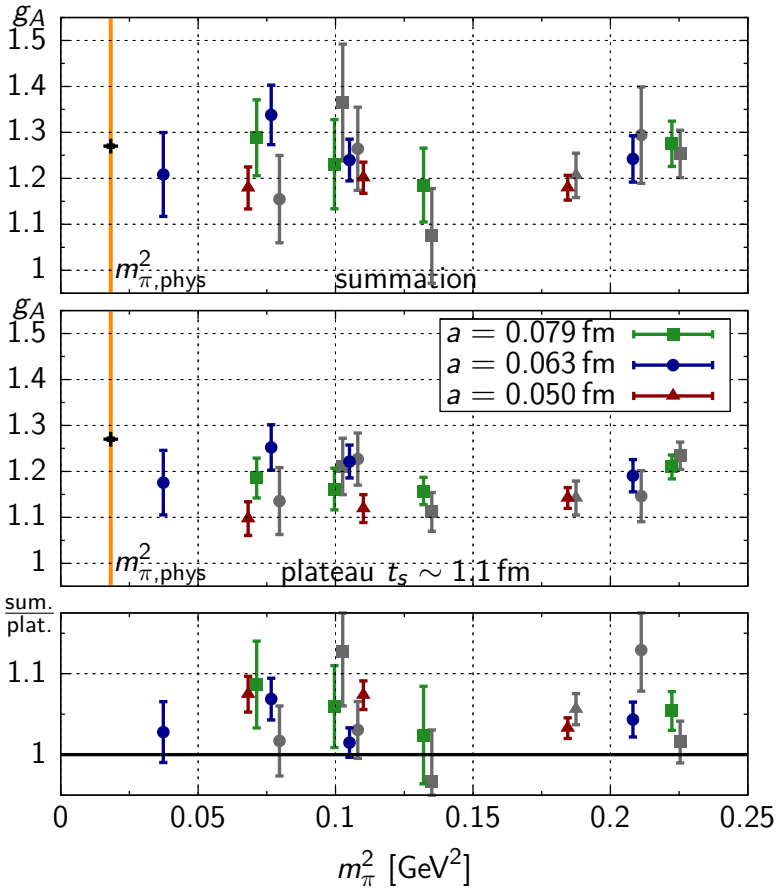

Figure 29: The axial charge of the nucleon determined using the summation method (upper panel) and plateau fits (middle panel). The lower panel shows the ratio of summation method and plateau fits. Our recent results [35] have been added in grey to the same plot and shifted slightly for readability.

is good, only a few points are outside the estimated uncertainties. Figure 31 shows a compilation the chirally extrapolated values of g_A from fits A-D on the the full pion mass range in blue. The open red symbols indicate the fit results on the reduced pion mass range $m_\pi < 365\,\mathrm{MeV}$. Fits A-D show remarkably good agreement among the different fit ansätze and fit ranges. Fit D shows larger statistical fluctuations, although three low-energy constants have been fixed from phenomenology (compare appendix) [60]. Since we do not see any influence of chiral logarithms, we use the linear extrapolation (fit B) as our final value of the axial charge of the nucleon. We take half of the spread, $\frac{1}{2}(\max - \min)$, of fits A-C on the full and reduced pion mass ranges as an estimate for the remaining uncertainty of the chiral extrapolation. If we include excited states using the summed operator insertion method, we end up with a value g_A which is either very close to or compatible with the experimental determination. The extrapolated values from the standard plateau method show a significant ($> 1\sigma$) discrepancy with the PDG value

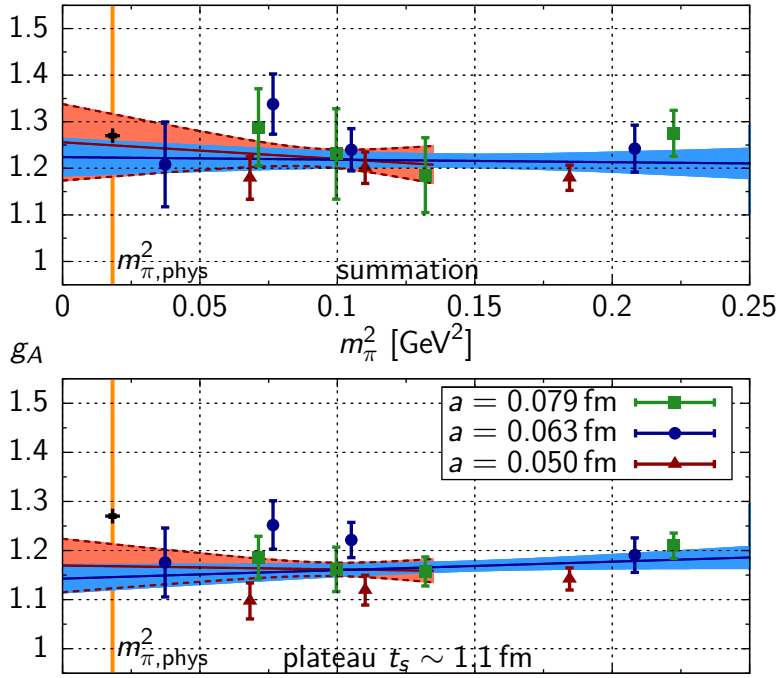

Figure 30: Chiral behaviour of the nucleon axial charge using the summation method (upper panel) and standard plateau fit (lower panel). The chiral fits correspond to Fit B using the complete range of the pion masses (blue) and a cut on the pion mass $m_\pi < 365\,\mathrm{MeV}$ (red).

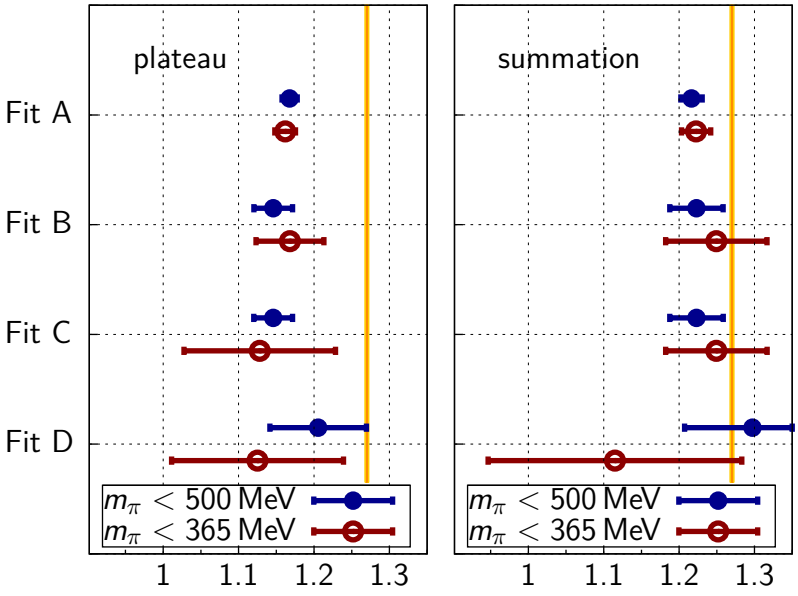

Figure 31: Comparison of the chiral extrapolations (Fit A-D). The open symbols (red) show the results for a cut on the pion mass $m_\pi < 365\,\mathrm{MeV}$.

of g_A. The difference indicates that the treatment of excited states using the summation method can resolve the mismatch seen between lattice simulations and phenomenology.

4.2 CUTOFF EFFECTS

Although we do not use the improved axial current, lattice artefacts enter at the level of $\mathcal{O}(a^2)$, since the spatial components of the local axial current receive $\mathcal{O}(a)$-improvement for vanishing momentum transfer,

$$\overline{\psi}(x)\gamma_5\gamma_3\psi(x) + ac_A\partial_3 P + \mathcal{O}(a^2). \tag{129}$$

We determine the axial charge using a correlators with vanishing momentum transfer, which removes the improvement term in equation (129). We check cutoff effects by a constant fit on the ensembles with a single lattice spacing. We find good agreement among the $\beta = 5.2$ and 5.3 ensembles, but a systematic downward trend for the ensembles with the smallest lattice spacing. A combined fit, which includes a term for the expected lattice artefacts, e.g.

$$g_A(m_\pi, a) = A + B\, m_\pi^2 + D\, a^2, \tag{130}$$

allows us to parametrise cutoff effects. The results of the combined fits are shown in figure 33 by the open green points. The blue points indicate the previously obtained results without cutoff effects included. By adding an additional parameter to the fits, we see an increase of the statistical uncertainties and a systematic trend towards smaller values for g_A. To confirm the influence of lattice artefacts, we need to improve the statistical precision of the individual ensembles, since we see the trend only on the $\beta = 5.5$ ensembles. We use half of the spread of the points shown in figure 33 for fit A-C as an estimate for cutoff effects.

4.3 FINITE-SIZE EFFECTS

In this work, we use ensembles with values of $m_\pi L \geq 4$, so that finite-size effects are empirically expected to be small [6, 104]. Unfortunately, there is no ideal set of ensembles to check for finite-size effects explicitly, since all the ensembles with different spatial extent also differ in the pion mass or the lattice spacing or both. Figure 34 shows the $m_\pi L$ dependence of the axial charge of the nucleon, where no systematic trend is visible. Since we have seen only a mild dependence on the pion mass, we can interpret figure 34 as evidence for small finite-size contributions. We find that the rule of thumb, $m_\pi L \geq 4$, is sufficient in the case of the axial charge. Other lattice collaborations [53, 54, 80] have seen a trend in $m_\pi L$ towards smaller values for the axial charge of the nucleon, especially if $m_\pi L \leq 4$, which we cannot confirm with our data.

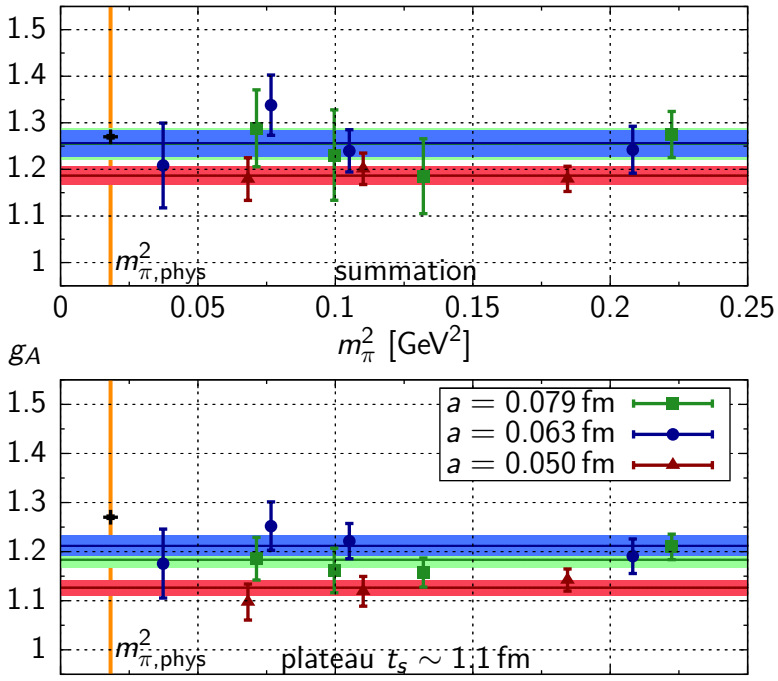

Figure 32: Individual constant chiral fits to the data at a fixed value of the lattice spacing.

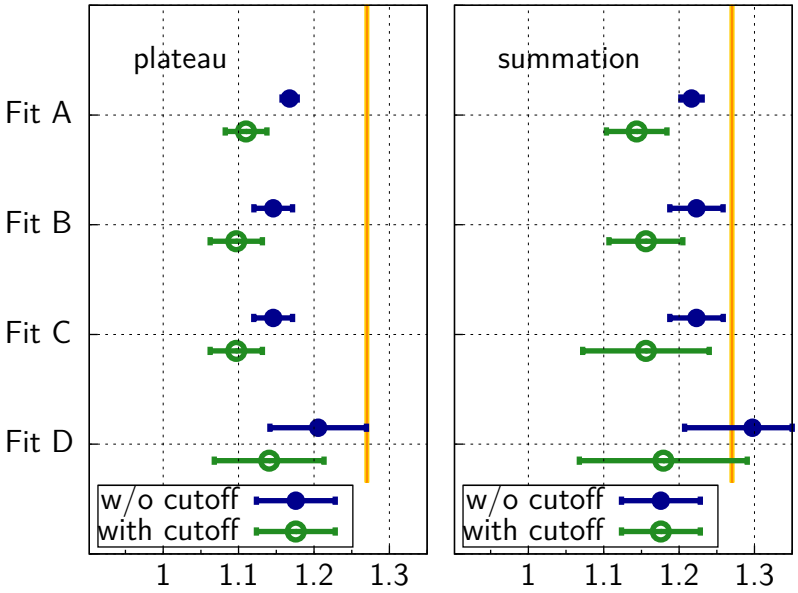

Figure 33: Comparison of the chiral extrapolations (Fit A-D). The open symbols (green) show the results for a combined fit including lattice artefacts.

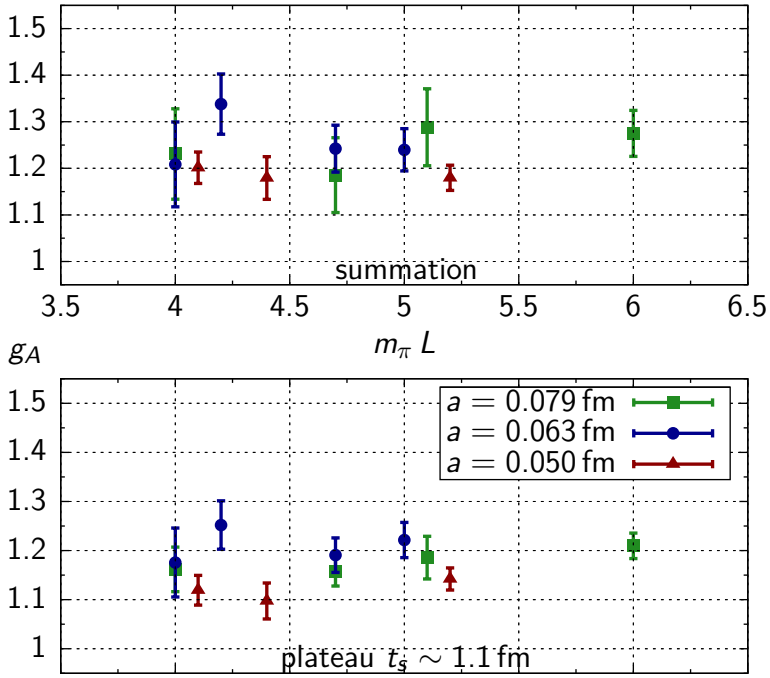

Figure 34: Study of finite-size effects for g_A.

5

NUCLEON ELECTRO-MAGNETIC FORM FACTORS

In this chapter, we present our results for the electro-magnetic form factors [74, 76, 77]. We will present a complete discussion of the main sources of the systematic uncertainties, which might however change slightly in the upcoming publication of these results. The vector form factors have been computed on the same subset of the gauge configurations as the axial charge, where details on the ensembles are listed in table 3. The determination of the form factors requires an additional description of the momentum dependence, for which we use a dipole fit (compare section 3.7),

$$G(Q^2) = \frac{G(0)}{\left(1 + \left(\frac{Q}{M}\right)^2\right)^2}. \tag{131}$$

With these fits we can extract the radius from the fit parameter M,

$$\langle r^2 \rangle = -\frac{6}{G(0)} \frac{\partial G(Q^2)}{\partial Q^2}\bigg|_{Q^2=0} = \frac{12}{M^2}. \tag{132}$$

In the following, we show results for the electric and magnetic Sachs form factors $G_E(Q^2)$, $G_M(Q^2)$ and the anomalous magnetic moment of the nucleon. The Pauli and Dirac form factors $F_1(Q^2)$ and $F_2(Q^2)$ represent a completely equivalent description of the same information. The results of the electric and magnetic radius are listed in table 5. The values of the anomalous magnetic moment of the nucleon can be found in table 6. Figure 35 shows the results for the electric radius $\langle r_E^2 \rangle$ determined by a dipole fit. In the upper panel of figure 35, we display the values obtained by the summed operator insertion method. The fits to the standard plateaus are shown in the middle part of figure 35. The comparison shows that including contaminations from excited states results in an upward shift of the data (compare to the lower panel of figure 35), which leads to better agreement with the experimentally determined value [47]. As seen for the axial charge, the statistical uncertainties become larger when we use the summation method.

The magnetic radius can be extracted in a completely analogous procedure from $G_M(Q^2)$. In contrast to $G_E(Q^2)$, we find little contamination from excited states. Figure 36 shows the results obtained using the summation method

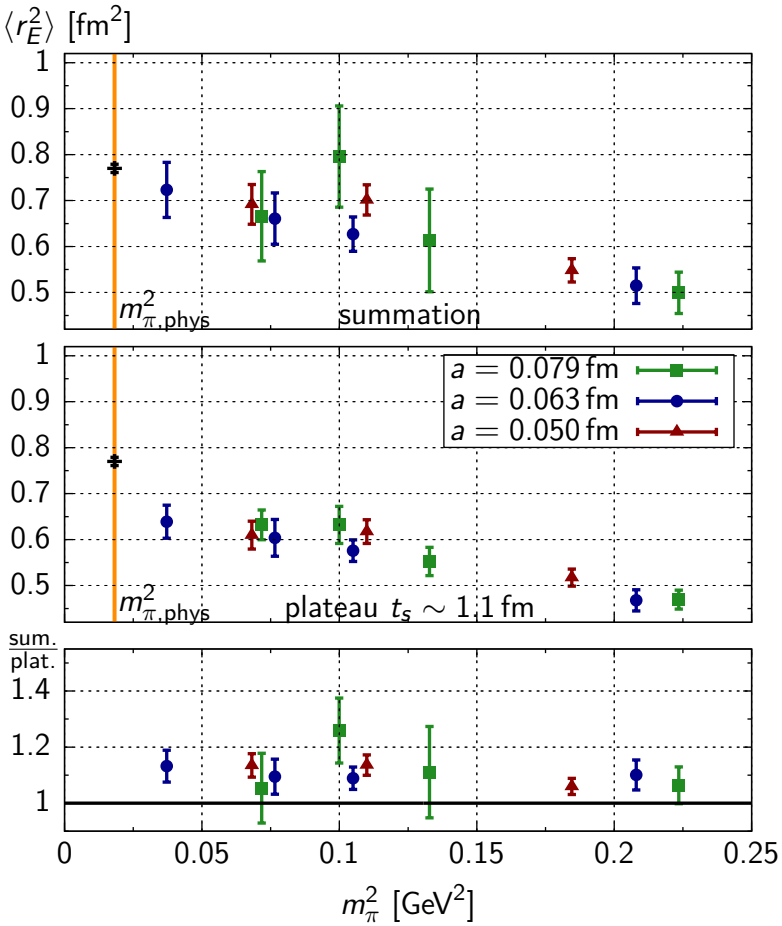

Figure 35: The electric radius $\langle r_E^2 \rangle$ of the nucleon determined using the summation method (upper panel) and plateau fits (middle panel). The ratio of summation method and plateau fits are shown in the lower panel.

(upper panel) and the standard plateau fits (middle panel). The larger statistical uncertainties are caused by the necessary extrapolation to $Q^2 = 0$, since we cannot compute the magnetic form factor directly at vanishing momentum. The larger statistical uncertainties might hide the contamination from excited states, which we have similarly seen for the axial charge in figure 25. Further study should reveal, whether contamination from excited states are small for $G_M(Q^2)$ or if the number of measurements is not sufficient to distinguish contaminations from excited states and statistical fluctuations.

The iso-vector anomalous magnetic moment of the nucleon,

$$\mu := \frac{G_M(0)}{F_1(0)} = \kappa + 1 \tag{133}$$

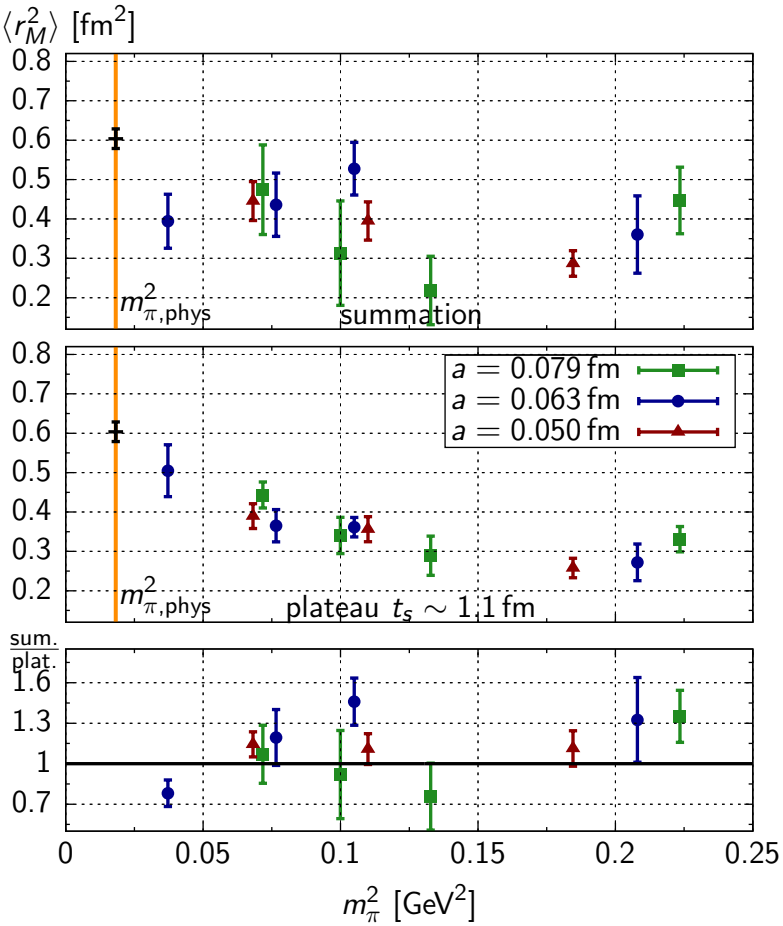

Figure 36: The magnetic radius $\langle r_M^2 \rangle$ of the nucleon determined using the summation method (upper panel) and plateau fits (middle panel). The ratio of summation method and plateau fits are shown in the lower panel.

can be extracted in two ways. We extrapolate either the results of the dipole fit to $G_M(Q^2)$ to vanishing momentum transfer or the ratio of the form factors G_M and F_1:

$$\begin{aligned} &G_M(Q^2 \to 0) \to \mu, \\ &\left.\frac{G_M(Q^2)}{F_1(Q^2)}\right|_{Q^2 \to 0} \to \mu. \end{aligned} \tag{134}$$

We use the second method since the momentum dependence of F_1 and G_M appears to be similar and results in an approximately constant ratio. Figure 37 shows the ratio of G_M and F_1 computed on the N6 ensemble and a constant fit, which give a good description of the ratio. For the magnetic moment, we see a significant shift in figure 38 if we include excited states using the summation method, which leads to a more favourable comparison with experiment.

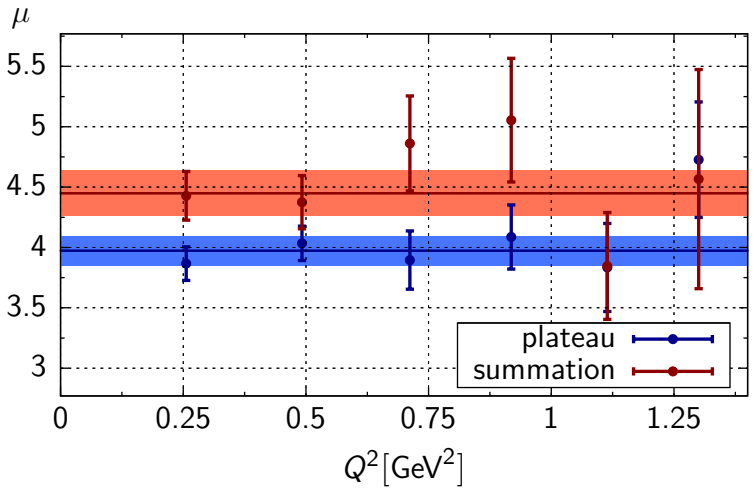

Figure 37: The ratio of G_M and F_1 computed on the N6 ensemble.

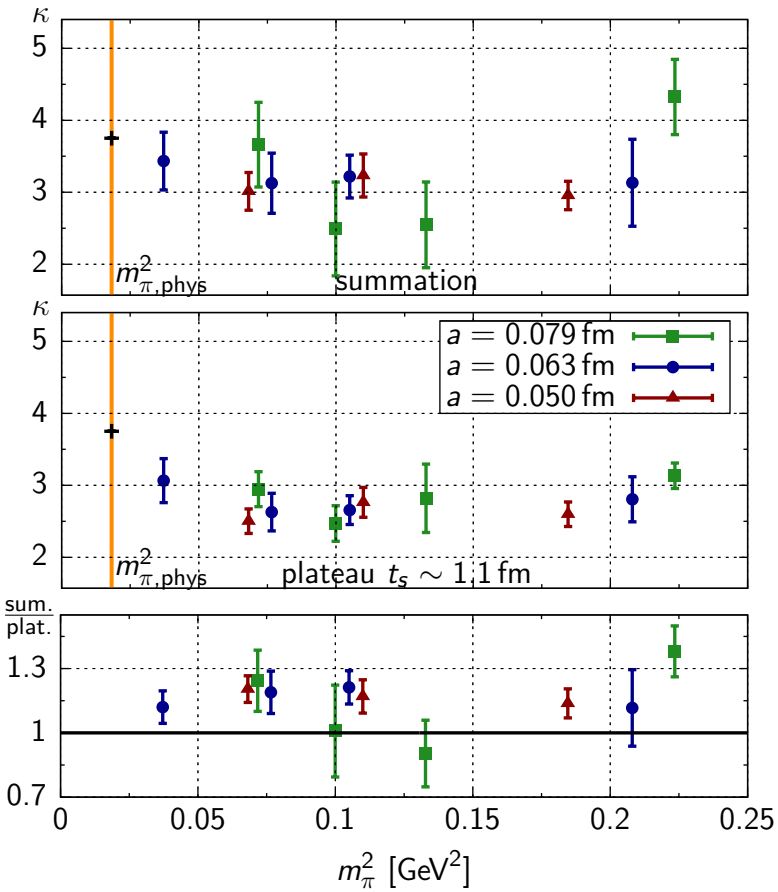

Figure 38: The anomalous magnetic moment κ of the nucleon determined using the summation method (upper panel) and plateau fits (middle panel). The ratio of summation method and plateau fits are shown in the lower panel.

Label	$\langle r_E^2 \rangle_{\text{plat.}}$ [fm^2]	$\langle r_E^2 \rangle_{\text{sum.}}$ [fm^2]	$\langle r_M^2 \rangle_{\text{plat.}}$ [fm^2]	$\langle r_M^2 \rangle_{\text{sum.}}$ [fm^2]
A3	0.469(21)	0.499(45)	0.331(32)	0.447(85)
A4	0.552(31)	0.6133(111)	0.289(50)	0.218(87)
A5	6.320(40)	0.7957(110)	0.341(46)	0.313(133)
B6	0.632(32)	0.6658(97)	0.443(33)	0.474(114)
E5	0.468(22)	0.5148(39)	0.272(47)	0.361(98)
F6	0.604(40)	0.6606(56)	0.365(41)	0.436(81)
F7	0.576(23)	0.6270(37)	0.361(25)	0.528(67)
G8	0.639(36)	0.7232(60)	0.505(66)	0.394(68)
N5	0.517(19)	0.5481(25)	0.258(25)	0.287(32)
N6	0.617(26)	0.7013(33)	0.356(32)	0.395(49)
O7	0.610(30)	0.6916(43)	0.390(32)	0.445(49)

Table 5: Results for the electro-magnetic radii $\langle r_E^2 \rangle$ and $\langle r_M^2 \rangle$.

5.1 CHIRAL BEHAVIOUR

We use similar fit functions for the chiral extrapolation as we have considered for the axial charge. Here we focus on the results from the linear fit. An analysis based on HBChPT fit forms will be considered in a following publication. We extrapolate $\langle r_E^2 \rangle$, $\langle r_M^2 \rangle$ and κ using a linear fit on the full pion mass range and compare it to a reduced pion mass range of $0 < m_\pi < 365\,\text{MeV}$. Figure 39 shows the results for the electric charge radius $\langle r_E^2 \rangle$, for which we find good agreement with the experimental value, provided that we include contaminations from excited states using the summed operator method. In the case of the magnetic radius $\langle r_M^2 \rangle$, we see a significant deviation from the experimental value. The large statistical fluctuations in $\langle r_M^2 \rangle$, which are caused by the necessary extrapolation of G_M to $Q^2 \to 0\,\text{GeV}^2$, prevent us from a systematic study of the contaminations from excited states. Currently, we see only a tendency indicated by the lower panel of figure 36, thus further studies are needed to improve the determination of the magnetic radius. The anomalous magnetic moment of the nucleon κ, shown in figure 41, indicates only a mild dependence on the pion mass. As for the electric radius, we find good agreement with the experimental determination, if we include contaminations from excited states. For the $\langle r_E^2 \rangle$, $\langle r_M^2 \rangle$ and κ, we will incorporate chiral fits motivated by HBChPT [105] to check these extrapolations.

Label	$\kappa_{\text{plat.}}$	$\kappa_{\text{sum.}}$
A3	3.133(18)	4.323(52)
A4	2.821(48)	2.548(60)
A5	2.470(25)	2.491(65)
B6	2.946(24)	3.662(59)
E5	2.806(31)	3.132(60)
F6	2.628(26)	3.126(42)
F7	2.656(20)	3.219(30)
G8	3.065(31)	3.433(40)
N5	2.598(17)	2.955(20)
N6	2.763(21)	3.232(30)
O7	2.502(17)	3.013(26)

Table 6: Results for the anomalous magnetic moment κ of the nucleon.

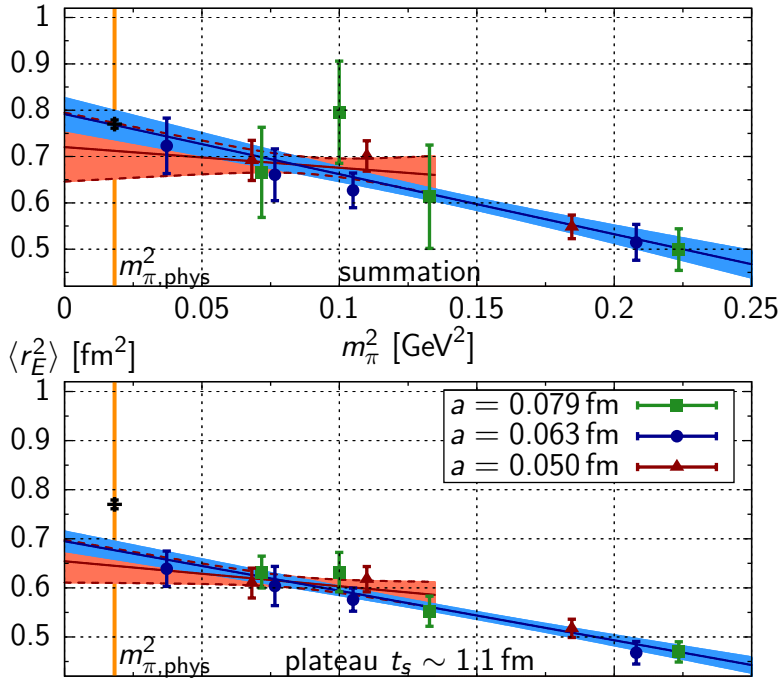

Figure 39: Comparison of the chiral extrapolation for the electric charge radius $\langle r_E^2 \rangle$.

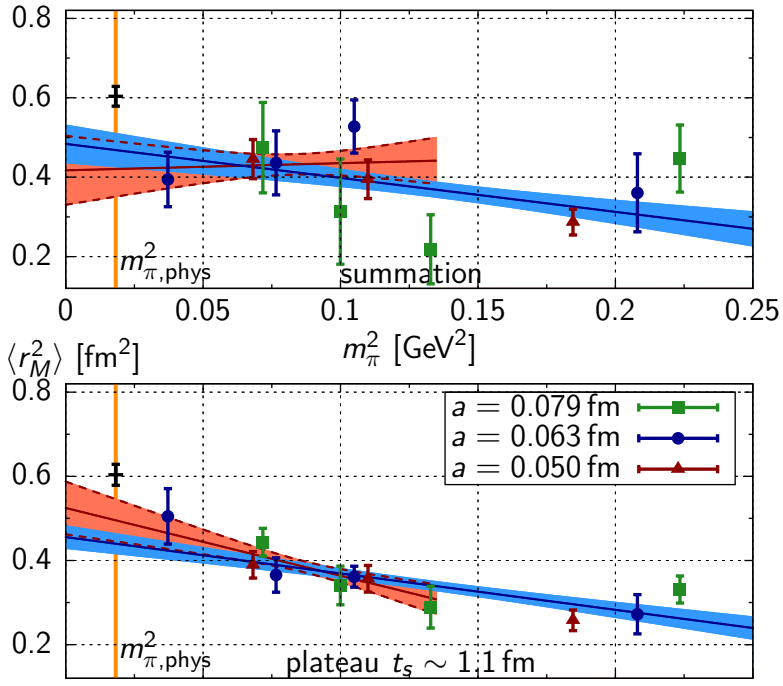

Figure 40: Comparison of the chiral extrapolation for the magnetic radius $\langle r^2_M \rangle$.

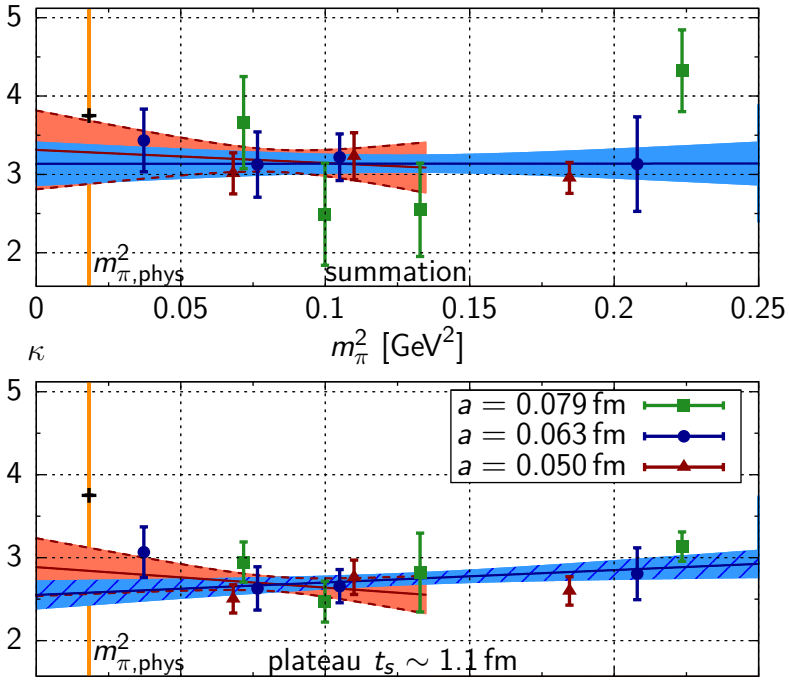

Figure 41: Comparison of the chiral extrapolation of the anomalous magnetic moment κ.

5.2 CUTOFF AND FINITE-SIZE EFFECTS

Cutoff effects are expected to enter at the level of $\mathcal{O}(a)$, although the action is non-pertubatively $\mathcal{O}(a)$ improved, since we did not include the improvement terms in the definition of the operators. Volume effects are expected to be small, since we use ensembles for which $m_\pi L \geq 4$ holds. The data in figures 35, 36 and 38 show no obvious systematic trend for the different lattice spacings or volumes. If we look in detail at the electric form factor $G_E(Q^2)$ on three different ensembles, which have approximately the same pion mass $\sim 260\,\mathrm{MeV}$ (B6, F7, and O7), we can study cutoff and finite-size effects. All three ensembles correspond to different lattice spacings, where two, the F7 and O7 ensemble, have a similar spatial extent. Figure 42 shows the electric form factor computed on these ensembles. The experimental parametrisation [101] has been added for illustration only, since the lattice results still require an extrapolation to the physical pion mass. We can conclude that cutoff and finite-size effects are smaller than our current statistical precision, since no systematic difference appears in figure 42. For the magnetic radius of the nucleon, we see a similar behaviour in figure 43. The absence of cutoff and finite-size effects justifies our strategy of fitting results on all three values of the lattice spacing to a common ansatz.

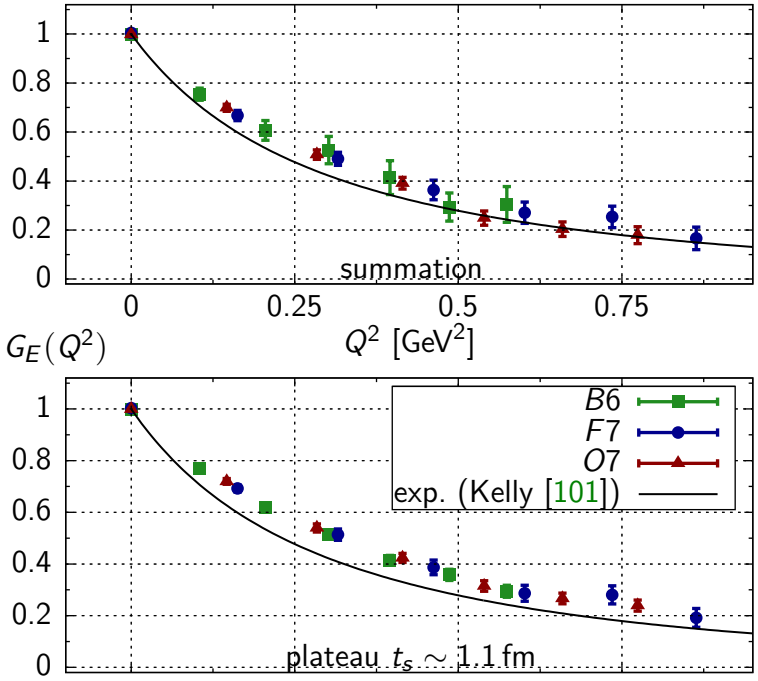

Figure 42: The electric form factor $G_E(Q^2)$ computed on three different ensembles with different lattice spacings and spatial extents. The experimental parametrisation has been added for illustration only.

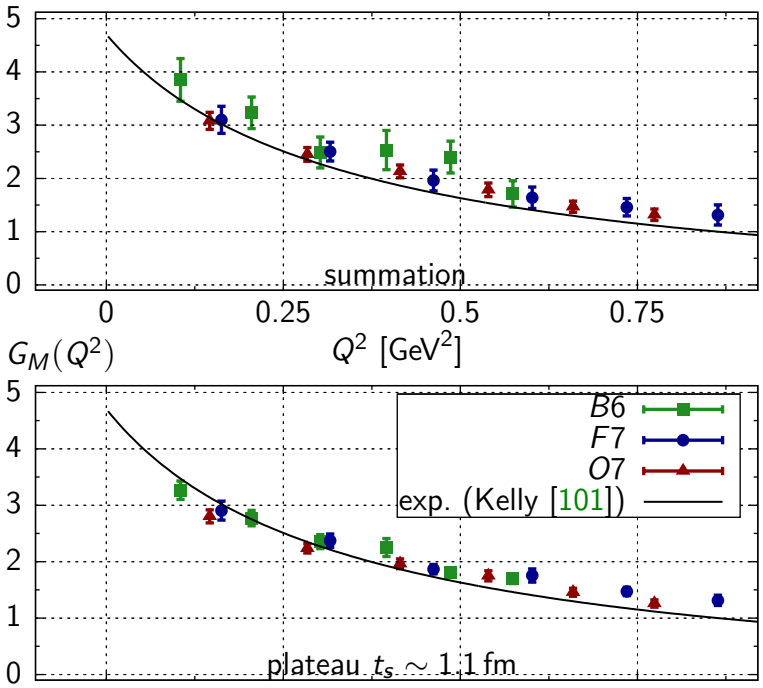

Figure 43: The electric form factor $G_M(Q^2)$ computed on three different ensembles with different lattice spacings and spatial extents. The experimental parametrisation has been added for illustration only.

6

CONCLUSIONS AND OUTLOOK

In the previous chapters, we have presented a lattice calculation of the nucleon axial charge and the electric and magnetic form factors. We have demonstrated that the inclusion of excited states via the summed operator insertion method leads to improved agreement with the experimentally determined values. If we summarise the statistical and systematic uncertainties of the axial charge, we find:

$$g_A[\text{plateau}] = 1.146(26)^{\text{stat}}(20)^{\text{chiral}}(35)^{\text{cutoff}}, \tag{135}$$

$$g_A[\text{summation}] = 1.224(40)^{\text{stat}}(16)^{\text{chiral}}(33)^{\text{cutoff}}. \tag{136}$$

Adding the uncertainties in quadrature, we achieve an accuracy of 4.2% using the standard plateau fit and 4.4% in the case of the summation method.

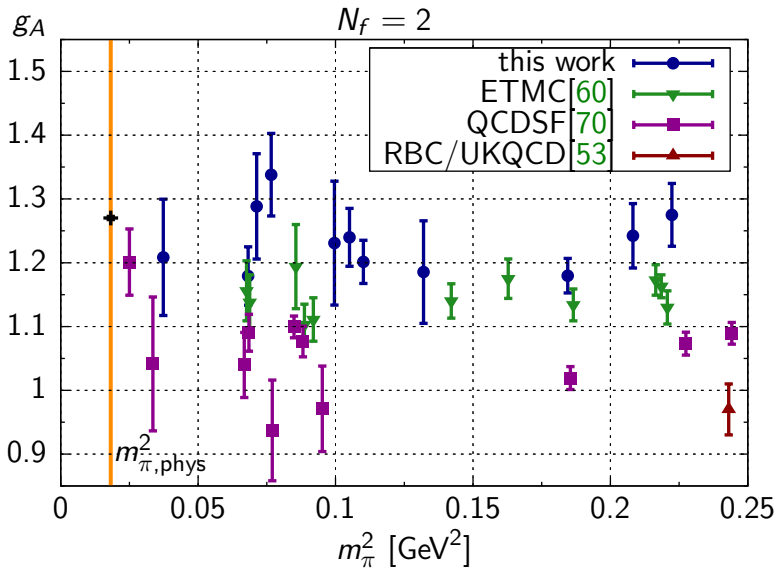

Figure 44: A comparison of the axial charge computed by various lattice groups [53, 60, 70].

The axial charge extracted from the plateau leads to a discrepancy with phenomenology at the level of 2.6σ, whereas including excited states yields agreement within one standard deviation. The largest source of systematic uncertainty is given by cutoff effects, since we see a downward trend for the finest

ensembles. Whether or not this is an accidental statistical fluctuation or a real effect cannot be decided with the current data. We find no consistent pattern of discretisation effects: ensembles with an intermediate lattice spacing tend to larger values, whereas ensembles with the finest lattice spacing result in smaller values. Cutoff effects are expected to be small, since the axial charge is $\mathcal{O}(a)$-improved, which makes a statistical fluctuation more likely. The chiral extrapolation adds another uncertainty, which will improve in the future, if we simulate directly at the physical pion mass. Currently, the CLS collaboration has started the generation of further ensembles, with one matched to the physical pion mass. Figure 44 shows a comparison of our results with other two-flavour lattice calculations [53, 60, 70], where our calculation includes contamination from excited states and find agreement with phenomenology.

The electric form factor and the anomalous magnetic moment show clear evidence of contamination from excited states. For the magnetic form factor, we cannot resolve contributions from excited states with the current statistical precision. As seen for the axial charge (in figure 25), contamination from excited states might still be hidden. If we summarise the statistical and systematic uncertainties for the electro-magnetic radii and anomalous magnetic moment, we find:

$$\langle r_E^2 \rangle = 0.768(32)^{\text{stat}}(28)^{\text{chiral}}\,\text{fm}^2, \tag{137}$$

$$\langle r_M^2 \rangle = 0.468(42)^{\text{stat}}(24)^{\text{chiral}}\,\text{fm}^2, \tag{138}$$

$$\kappa = 3.14(24)^{\text{stat}}(7)^{\text{chiral}} \tag{139}$$

The values have been obtained using the linear fit on the full pion mass range and the data extracted using the summed operator insertion method. The chiral extrapolation adds a systematic uncertainty, which we will check using fits motivated by HBChPT [105]. As discussed in the previous chapters, we see very little influence, if any, from cutoff and finite-size effects. A combined fit of all the form factors will help us to constrain the chiral fits as much as possible. The extraction of the radii depends on a good description of the momentum behaviour, which introduces another systematic uncertainty. Even for our largest ensemble, the smallest non-vanishing momentum is $\sim 0.1\,\text{GeV}^2$, which requires a long extrapolation especially for $G_M(Q^2)$. Partially twisted boundary conditions introduced in section 1.6 offer an alternative, which allows us to tune the momentum transfer to any arbitrary value. So far, partially twisted boundary conditions have been successfully used in mesonic quantities and in the anomalous magnetic moment of the muon, which is presented in the next part. A study in [106] has explored the use of partially twisted boundary conditions in baryonic observables.

The lattice spacing from [24] is used as an input in this calculation, thus additional uncertainties related to the lattice spacing are relevant. In the calculation of the axial charge, the lattice spacing has a minor influence on the

overall value, since it only appears in the conversion of the pion mass into physical unit.

Beyond the axial charge and the electro-magnetic form factors, we have included additional operators in our simulation, which allows us to determine a larger set of observables. The axial form factor $G_A(Q^2)$ and the induced pseudoscalar form factor $G_P(Q^2)$ can be extracted by the same techniques as presented in this work. We have also included operators with one derivative, which allows us to relate the hadron matrix element to the generalised form factors $A_{20}(Q^2)$, $B_{20}(Q^2)$ and $C_{20}(Q^2)$

$$\left\langle p', s' \middle| \gamma_{\{\mu} \overleftrightarrow{D}_{\nu\}} \middle| p, s \right\rangle = \bar{u}(p,s)\Big(\gamma_{\{\mu} Q_{\nu\}} A_{20}(Q^2) + \mathrm{i}\frac{\sigma_{\{\mu\alpha} Q_\alpha p_{\nu\}}}{2m} B_{20}(Q^2) + \frac{1}{m} p_{\{\mu} p_{\nu\}} C_{20}(Q^2)\Big) u(p,s). \tag{140}$$

The average quark momentum fraction $\langle x \rangle_{u-d}$ can be extracted from the form factor

$$A_{20}(0) = \langle x \rangle_{u-d} \tag{141}$$

up to a necessary renormalisation. Figure 45 shows an example of the bare ratio of three- and two-point functions used to the determine the quark momentum fraction $\langle x \rangle_{u-d}$ computed on the N6 ensemble.

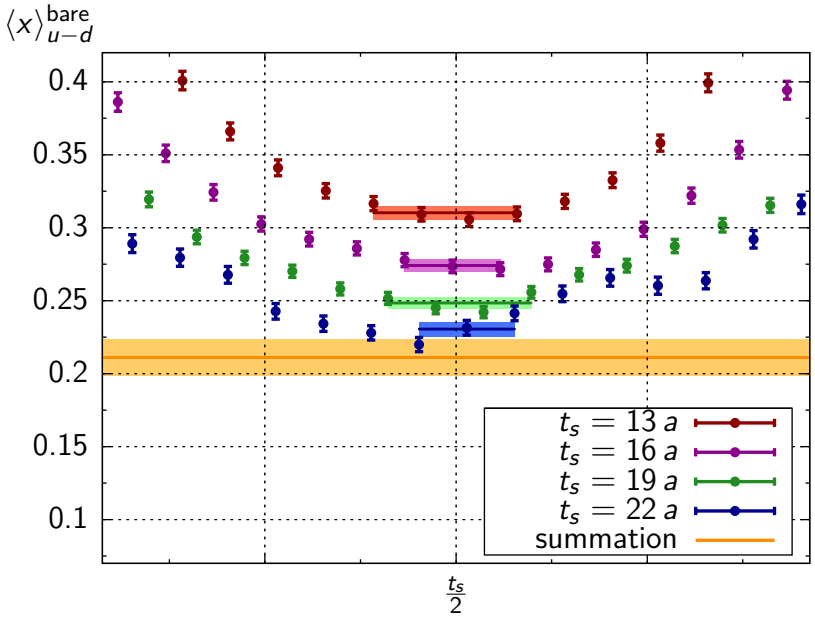

Figure 45: The bare ratio of the average quark momentum fraction $\langle x \rangle_{u-d}$ determined on the N6 ensemble.

Contaminations from excited states appear to be even more pronounced than for the axial charge or the electro-magnetic form factors. Further studies, including the appropriate renormalisation constant, will reveal if the treatment of

excited states can solve the current mismatch seen between lattice simulation and experimental data for the average quark momentum fraction [48]. The LHPC collaboration [64] finds agreement with phenomenology, if contributions from excited states have been included in the determination of $\langle x \rangle_{u-d}$.

Part III

HADRONIC VACUUM POLARISATION FOR $(g-2)_\mu$

7

INTRODUCTION

The *anomalous magnetic moment of the muon*, defined by

$$a_\mu \equiv \frac{g_\mu - 2}{2}, \tag{142}$$

is one of the most precisely measured quantities in physics. The current level of accuracy has reached 0.5 ppm [107]. a_μ receives significant contributions from electro-magnetic, weak, and strong interactions, which can be predicted to a precision compatible with experiments allowing a stringent test of the *Standard Model of Particle Physics* (SM). Indeed, a persistent tension of $\sim 3\sigma$ between theory and experiment [47] is found, which might indicate physics beyond the SM. The anomalous magnetic moment of the muon is more sensitive to potential new physics effects as the one of the electron, because of an enhancement by the mass of the muon $a_\mu/a_e \sim (m_\mu/m_e)^2$ in quantum corrections. Before postulating New Physics, the uncertainties in theory and experiment must be improved to exclude a statistical fluctuation within the SM. The uncertainty of the theoretical predictions is dominated by contributions from the strong interaction, i.e. the hadronic vacuum polarisation and the light-by-light diagrams. In the following sections the experimental methodology and the individual contribution to a_μ from the SM will be presented; more detailed reviews can be found in [47, 108].

7.1 EXPERIMENTAL DETERMINATION

The experimental determination of a_μ started at CERN in 1961, where the anomalous magnetic moment was measured with an 0.4% accuracy [109]. With the more recent E821 experiment in Brookhaven, the uncertainty has been reduced to a level of 0.5 ppm [107]. We will present the basic concepts of the measurement in the following, a more detailed picture of the experimental setup can be found in [47, 107].

In a storage ring with a constant magnetic field B, the muon precesses along a circle with the Larmor frequency

$$\omega_p = \frac{eB}{m_\mu \gamma}, \tag{143}$$

where γ is the Lorentz factor. The anomalous magnetic moment of the muon causes a small change in the precession of the spin,

$$\omega_s = \frac{eB}{m_\mu \gamma} + a_\mu \frac{eB}{m_\mu}. \tag{144}$$

Measuring the difference in the Larmor frequency of spin and momentum

$$\omega_a = \omega_s - \omega_p = \left(\frac{eB}{m_\mu \gamma} + a_\mu \frac{eB}{m_\mu} \right) - \frac{eB}{m_\mu \gamma} = a_\mu \frac{eB}{m_\mu}. \tag{145}$$

directly gives the anomalous magnetic moment of the muon, a_μ. This setup requires the precise knowledge of the magnetic field B and the muon mass m_μ. A schematic of the experiment is shown in figure 46.

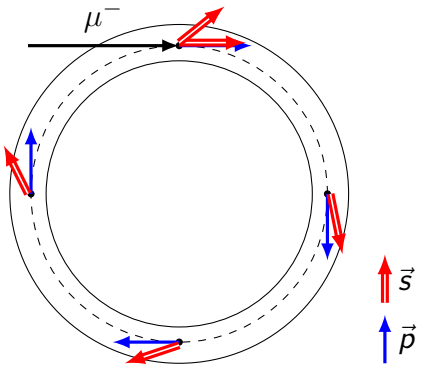

Figure 46: Schematic of experimental setup of the $(g-2)_\mu$ measurement showing the precessing muon $\vec{p}$ and its spin $\vec{s}$ in a constant magnetic field.

To measure the Larmor frequency of the spin, one exploits the decay of the muon, which is shown in figure 47.

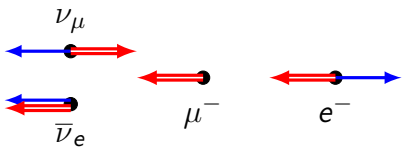

Figure 47: Weak decay pattern of the muon

The momentum of the emerging electron is anti-parallel to the muon spin because of the chiral nature of the weak interaction. The neutrinos involved in this decay are left-handed in the case of the muon neutrino and right-handed for the electron-anti-neutrino. The masses of the neutrinos have small upper bounds, so that the decay shown in figure 47 is strongly preferred.

The E821 collaboration [107] determine the anomalous magnetic moment to be

$$a_{\mu^+}^{\text{exp}} = 11659204(6)(5) \cdot 10^{-10} \tag{146}$$

for the anti-muon and

$$a_{\mu^-}^{\text{exp}} = 11659215(8)(3) \cdot 10^{-10} \tag{147}$$

for the muon. Both measurements show a good agreement and confirm lepton universality. The world average of the muon's anomalous magnetic moment is

$$a_{\mu}^{\text{exp}} = 11659208.9(5.4)(3.3) \cdot 10^{-10}. \tag{148}$$

Currently, the storage ring of the E821 experiment is being moved to Fermilab, so that a cleaner and more intense muon beam can be used. The uncertainty of the experimental value is expected to decrease by a factor 4 [47].

7.2 STANDARD MODEL PREDICTION FOR a_μ

The theory prediction of the anomalous magnetic moment of the muon receives contributions from electro-magnetic, weak and strong interaction, which will be presented in the following.

7.2.1 *Electro-magnetic contributions*

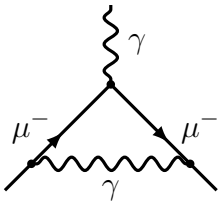

Figure 48: Leading QED contribution to $(g-2)_\mu$

The electro-magnetic interaction can be computed using the theory of Quantum Electrodynamics (QED). Since the fine structure constant [47]

$$\alpha = 7.2973525698(24) \cdot 10^{-3} \ll 1, \tag{149}$$

the electro-magnetic contribution to $(g-2)_\mu$ can be computed using a perturbative expansion in the coupling constant

$$a_\mu^{\text{QED}} = \sum_{n=1}^{\infty} a_\mu^{(2n)} \left(\frac{\alpha}{\pi}\right)^n. \tag{150}$$

The leading QED contribution to the anomalous magnetic moment of the muon can be found in figure 48, which was first computed by Schwinger [110]. Given the experimental precision, the expansion must be extended up to the fifth order in $\left(\frac{\alpha}{\pi}\right)$ to achieve a similar accuracy. The number of diagrams

contributing grows significantly when including higher corrections. Kinoshita et al. [111] have recently succeeded in computing all diagrams entering at the fifth order, finding

$$a_\mu^{\text{QED}} = 0.5\left(\frac{\alpha}{\pi}\right)^1 + 0.765857425(17)\left(\frac{\alpha}{\pi}\right)^2 + 24.05050996(32)\left(\frac{\alpha}{\pi}\right)^3 + 130.8796(63)\left(\frac{\alpha}{\pi}\right)^4 + 753.29(1.04)\left(\frac{\alpha}{\pi}\right)^5 + \ldots \tag{151}$$

The uncertainties listed above include the uncertainties from numerical computations, as well as the uncertainties of the physical parameters such as the fine structure constant and the lepton masses. The leading contribution at the sixth order has been estimated to be [111]

$$a_\mu^{\text{QED}}\,[6-\text{loop}] \sim 0.8 \cdot 10^{-12}, \tag{152}$$

which is approximately twice the size of the uncertainty of the complete fifth order. The QED contribution to the anomalous magnetic moment of the muon up to the fifth order is [111]

$$a_\mu^{\text{QED}} = 11658471.8846(37) \cdot 10^{-10}. \tag{153}$$

The QED calculation has achieved an impressive accuracy of 0.3 ppb.

7.2.2 *Weak contributions*

The weak interaction can be understood as the exchange of massive $W^\pm$ and Z-bosons with the masses of [47].

$$m_{W^\pm} = 80.385(15)\,\text{GeV} \quad \text{and} \quad m_Z = 91.1876(21)\,\text{GeV}. \tag{154}$$

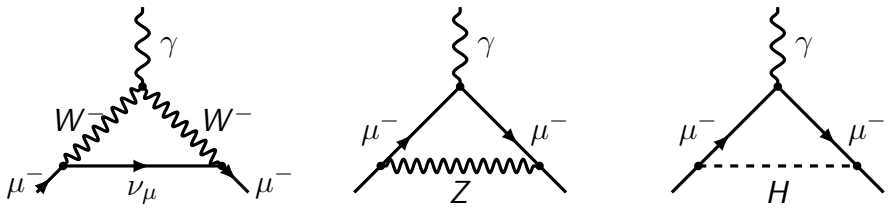

Figure 49: Lowest order diagrams for the weak contribution to $(g-2)_\mu$

The energy scale relevant in the anomalous magnetic moment of the muon is small compared to the masses of the $W^\pm$ and Z-bosons, which allows for a perturbative treatment of the weak interaction. The leading order diagrams can be seen in figure 49, one of which involves the Higgs particle. The 2013 Nobel prize was awarded to Englert and Higgs for the prediction of the Higgs

particle and mechanism [112, 113]. However, a contribution to $(g-2)_\mu$ from the Higgs particle can still be neglected [108]

$$a_\mu^{\text{weak}}\,[\text{Higgs}] \sim 10^{-14}. \tag{155}$$

The remaining weak diagrams at one and two-loop level turn out to be small, but relevant for the required precision [47]:

$$a_\mu^{\text{weak}}\,[1-\text{loop}] = 19.482(2)\cdot 10^{-10}, \tag{156}$$

$$a_\mu^{\text{weak}}\,[2-\text{loop}] = -4.07(21)\cdot 10^{-10}. \tag{157}$$

The leading logarithms for the three-loop contribution have been evaluated [47],

$$a_\mu^{\text{weak}}\,[3-\text{loop}] \sim 10^{-12}. \tag{158}$$

This contribution can be neglected at the current level of accuracy.

7.2.3 *Strong contributions*

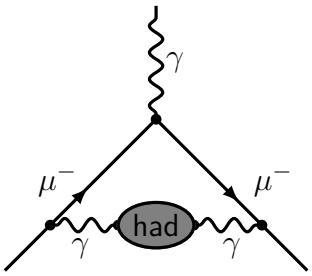

Figure 50: Hadronic vacuum polarisation diagram for $(g-2)_\mu$.

The strong interaction does not directly couple to leptons, but hadronic effects contribute indirectly via loops. The leading diagram can be seen in figure 50, which enters at the level of $\left(\frac{\alpha}{\pi}\right)^2$. The non-perturbative nature of QCD prevents a perturbative treatment of hadronic effects to $(g-2)_\mu$, and therefore a non-perturbative approach is necessary. Currently, the most accurate estimate is obtained using the optical theorem and dispersion relation, which allows one to use $e^+e^- \to$ hadrons measurements to obtain the leading hadronic contribution to the anomalous magnetic moment of the muon.

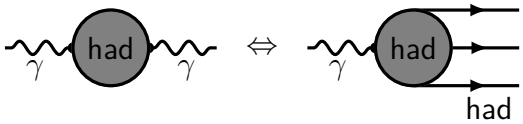

Figure 51: Visualisation of the Optical Theorem: Connecting the imaginary part of the hadronic vacuum polarisation to hadronic total cross section of $e^+e^- \to$ hadrons.

The optical theorem relates the total cross-section of $e^+e^- \to$ hadrons to the imaginary part of the vacuum polarisation $\Pi(s)$:

$$\operatorname{Im}\Pi(s) = \frac{s}{4\pi\alpha_s(s)}\sigma_{\text{tot}}(e^+e^- \to \text{hadrons}) = \frac{\alpha_s(s)}{3}R(s). \tag{159}$$

The contribution to $(g-2)_\mu$ can be obtained by a dispersion integral over the center of mass energy s from the hadronic vacuum polarisation,

$$a_\mu^{\text{hvp}} = \left(\frac{\alpha_s m_\mu}{3\pi}\right)^2 \left(\int_{m_\pi^2}^{E_{\text{cut}}^2} \mathrm{d}s\, \frac{R_{\text{opt}}(s)K(s)}{s^2} + \int_{E_{\text{cut}}^2}^{\infty} \mathrm{d}s\, \frac{R_{\text{per}}(s)K(s)}{s^2} \right). \tag{160}$$

The integral has been split into two separate parts. In the low-energy regime the optical theorem is used to determine the ratio $R_{\text{opt}}(s)$. In the high-energy region ($m_{\text{cut}} \gtrsim 2\,\text{GeV}$), perturbation theory provides a description of the ratio $R_{\text{per}}(s)$. The integration kernel in equation (160) is given by

$$K(s) = \frac{3s}{m_\mu^2}\left(\frac{s^2}{2}(2-s^2) + \frac{(1+s^2)(1+s^2)}{s^2}\left(\ln(1+s) - s + \frac{s^2}{2}\right) + \frac{(1+s)}{(1-s)}s^2\ln(s)\right). \tag{161}$$

The main source of the uncertainty on the hadronic vacuum polarisation is given by the experimental input in equation (159) and the numerical evaluation of the low-energy part of the dispersion integral [47]

$$a_\mu^{\text{hvp}}\,[\alpha^2] = 695.5(4.0)^{\text{opt}}(0.7)^{\text{per}} \cdot 10^{-10}. \tag{162}$$

The uncertainty of the hadronic vacuum polarisation is an order of magnitude larger than the QED and weak uncertainties. Diagrams at the level of $\left(\frac{\alpha}{\pi}\right)^3$ including the hadronic vacuum polarisation can been computed using the same techniques as presented before [108],

$$a_\mu^{\text{hvp}}\,[\alpha^3] = -9.8(0.1) \cdot 10^{-10}. \tag{163}$$

At order $\left(\frac{\alpha}{\pi}\right)^3$, an additional the diagram shown in figure 52 appears, which cannot be computed using the optical theorem. The current estimates of this light-by-light contribution to the anomalous magnetic moment of the muon have been obtained in large-N_C (number of colours) expansions or model calculations. The value quoted in the PDG [47] is

$$a_\mu^{\text{lbl}} = 10.5(2.6) \cdot 10^{-10}. \tag{164}$$

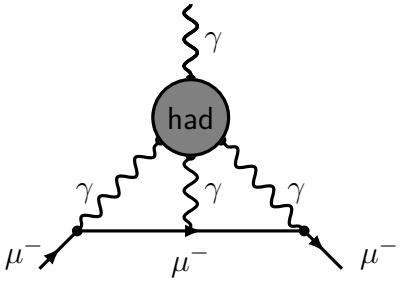

Figure 52: Light-by-light scattering diagram for $(g-2)_\mu$.

7.3 COMPARISON OF THEORY AND EXPERIMENT

Summing up the individual SM contributions leads to the theory prediction, which disagrees with the experimentally determined value for a_μ at the level of 3.2σ [47]:

$$\begin{aligned} a_\mu^{\text{theo}} &= 11659183.5\,(0.004)^{\text{QED}}(0.2)^{\text{weak}}(4.1)^{\text{hvp}}(2.6)^{\text{lbl, }\alpha^3} \cdot 10^{-10}, \\ a_\mu^{\text{exp}} &= 11659208.9\,(5.4)^{\text{stat}}(3.3)^{\text{sys}} \cdot 10^{-10}, \\ \Delta a_\mu &= a_\mu^{\text{exp}} - a_\mu^{\text{theo}} = 25.5(6.3)^{\text{exp.}}(4.9)^{\text{theo.}} \cdot 10^{-10}. \end{aligned} \tag{165}$$

The left panel of figure 53 shows that the anomalous magnetic moment of the muon is dominated by QED contributions. Weak and strong interaction add a small but non-negligible contribution to a_μ. The uncertainties of $(g-2)_\mu$ are shown in the right panel of figure 53, in which hadronic effects clearly dominate by an order of magnitude. Note that the pie chart lists the relative size of the error, if the uncertainties are added in quadrature, the hadronic vacuum polarisation uncertainty will become even more dominant. Currently, the uncertainty of the experimental measurement exceeds the theoretical one. A future experiment at Fermilab is aiming for an improvement of the experimental accuracy by a factor of 4 [47], so that the theory prediction must also be improved.

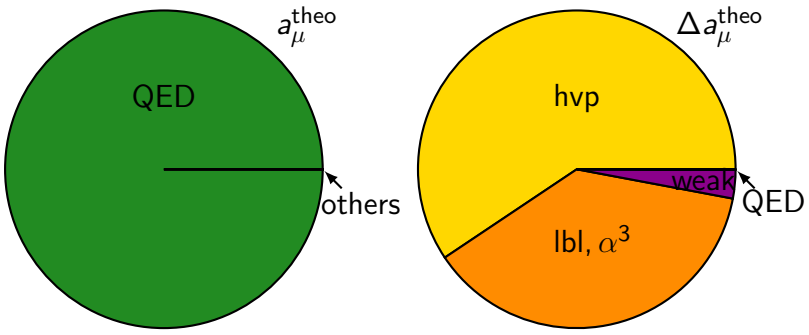

Figure 53: Left: Comparison of the individual Standard Model contribution to a_μ. Right: The size of the individual uncertainties to $(g-2)_\mu$.

8

LATTICE CALCULATIONS

As discussed in the previous chapter, the leading hadronic contribution, shown in figure 54, dominates the uncertainties of the theoretical prediction of the anomalous magnetic moment of the muon. In the following, we will present an ab initio calculation of the hadronic vacuum polarisation using lattice QCD, which has become a very active field of research in the lattice community [114–128].

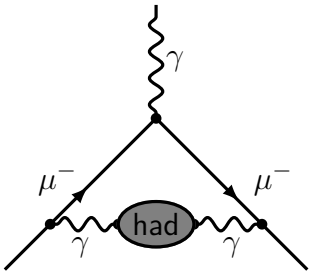

Figure 54: Hadronic vacuum polarisation diagram for $(g-2)_\mu$

The leading hadronic contribution to $(g-2)_\mu$ can be obtained from a convolution integral [129, 130],

$$a_\mu^{\text{hvp}} = \left(\frac{\alpha}{\pi}\right)^2 \int_0^\infty \frac{1}{Q^2} f(Q^2)\, \widehat{\Pi}(Q^2)\, \mathrm{d}Q^2. \tag{166}$$

The integrand is the product of two parts, the subtracted vacuum polarisation

$$\widehat{\Pi}(Q^2) = 4\pi \left(\Pi(0) - \Pi(Q^2)\right) \tag{167}$$

and the kernel $f(Q^2)$, which is known analytically from QED [129, 130],

$$f(Q^2) = \frac{m_\mu^2 Q^4 Z^3 (1 - Q^2 Z)}{1 + m_\mu^2 Q^2 Z^2} \quad \text{with} \quad Z = \frac{Q^2 - \sqrt{Q^4 - 4m_\mu^2 Q^2}}{2m_\mu^2 Q^2}. \tag{168}$$

In the following, we present a lattice calculation of the subtracted vacuum polarisation, which is needed to evaluate the integral in equation (166).

8.1 VACUUM POLARISATION

The Euclidean hadronic vacuum polarisation tensor $\Pi^f_{\mu\nu}(Q)$ can be obtained by a discrete four-dimensional Fourier-transformation of a current-current correlator,

$$\Pi^f_{\mu\nu}(Q) = a^4 \sum_n e^{iQn} \left\langle J^f_\mu(n) J^f_\nu(0) \right\rangle , \tag{169}$$

where $J^f_\mu(n)$ is the electro-magnetic current of flavour f. The vacuum polarisation tensor is a weighted sum over all flavours in the theory,

$$\Pi_{\mu\nu}(Q) = \sum_{f=u,d,s,\ldots} z_f^2 \, \Pi^f_{\mu\nu}(Q), \tag{170}$$

where we drop the quark charges z_f and the sum to simplify the notation. With these definitions the vacuum polarisation $\Pi(Q^2)$ can be extracted from $\Pi_{\mu\nu}(Q)$ via

$$\Pi_{\mu\nu}(Q) = \left(Q_\mu Q_\nu - Q^2 \delta_{\mu\nu} \right) \Pi(Q^2), \tag{171}$$

excluding contributions with vanishing transverse momentum. The momentum transfer Q^2 is obtained by

$$Q^2 = \sum_\mu \frac{4}{a^2} \sin^2 \left(\frac{a \, \hat{p}_\mu}{2} \right) , \tag{172}$$

where $\hat{p}_\mu$ is defined as

$$\hat{p}_\mu = \frac{2\pi}{L} n_\mu . \tag{173}$$

In the lattice formulation, the naïve local vector current $\overline{\psi}(n)\gamma_\mu\psi(n)$ is not conserved, so we use the point-split vector current, which can be derived using Noether's theorem (compare section 1.5). The Wick-contractions of the vector-vector correlator lead to a quark-connected diagram and a quark-disconnected diagram, both shown in figure 55.

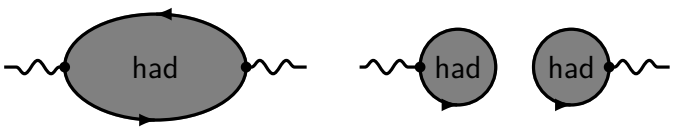

Figure 55: Left: Connected diagram for the hadronic vacuum polarisation. Right: Disconnected diagram for the hadronic vacuum polarization.

In this work, we only consider the connected diagram, since the computation of the disconnected diagram is a computationally demanding task. Nevertheless, Della Morte and Jüttner [131, 132] have estimated, using two-flavour

chiral perturbation theory, that the disconnected diagrams contribute approximately -10% of the connected one. This result has been derived independently in [123].

In [133, 134], we have used two conserved vector currents to construct the vacuum polarisation tensor, which is a sum of

$$\begin{aligned}\Pi^{(1)}_{\mu\nu}(Q) = \frac{a^4}{4}\sum_n e^{iQ(n+a\hat{\mu}/2-a\hat{\nu}/2)} \\ \mathrm{Tr}\Big[&(1+\gamma_\nu)U^\dagger_\nu(0)\gamma_5 S^\dagger(n+a\hat{\mu},0)\gamma_5(1+\gamma_\mu)U^\dagger_\mu(n)S(n,a\hat{\nu}) \\ &-(1-\gamma_\nu)U_\nu(0)\gamma_5 S^\dagger(n+a\hat{\mu},a\hat{\nu})\gamma_5(1+\gamma_\mu)U^\dagger_\mu(n)S(n,0) \\ &-(1+\gamma_\nu)U^\dagger_\nu(0)\gamma_5 S^\dagger(n,0)\gamma_5(1-\gamma_\mu)U_\mu(n)S(n+a\hat{\mu},a\hat{\nu}) \\ &+(1-\gamma_\nu)U_\nu(0)\gamma_5 S^\dagger(n,a\hat{\nu})\gamma_5(1-\gamma_\mu)U_\mu(n)S(n+a\hat{\mu},0)\Big]\end{aligned} \tag{174}$$

and a contact term, which arises from Noether's theorem,

$$\Pi^{(2)}_{\mu\nu}(Q) = \frac{a}{2}\delta_{\mu\nu}\mathrm{Tr}\Big[(1+\gamma_\nu)U^\dagger_\nu(0)S(0,a\hat{\nu}) + (1+\gamma_\nu)U_\nu(0)S^\dagger_\nu(0,a\hat{\nu})\Big]. \tag{175}$$

The determination of the vacuum polarisation tensor thus requires the computation of five propagators, where one starts at the origin $S(m,0)$ and the other four are shifted by one lattice spacing $S(m,a\hat{\nu})$.

In [121], we have exchanged one of the point-split currents by a local vector current, following a strategy by Boyle et al. in [119]. The combination of a local and a conserved vector current allows us to obtain the vacuum polarisation tensor,

$$\begin{aligned}\Pi_{\mu\nu}(Q) = Z_V\,\frac{a^4}{4}\sum_n e^{iQ(n+a\hat{\mu}/2)} \\ \mathrm{Tr}\Big[&\gamma_\nu\gamma_5 S^\dagger(n+a\hat{\mu},0)\gamma_5(1+\gamma_\mu)U^\dagger_\mu(n)S(n,0) \\ &-\gamma_\nu\gamma_5 S^\dagger(n,0)\gamma_5(1-\gamma_\mu)U_\mu(n)S(n+a\hat{\mu},0)\Big],\end{aligned} \tag{176}$$

with one inversion $S(m,0)$, which reduces the numerical effort by a factor of five. The appearance of the local vector current necessitates the multiplication with the renormalisation factor $Z_V(1+b_V\,am)$. The vector current renormalisation constant Z_V can be determined to a very high precision [32]. For our set of ensembles, the accuracy of Z_V is better than 0.7%, which, at the moment, does not limit the overall precision of the vacuum polarisation. Figure 56 shows a comparison of the subtracted vacuum polarisation for the case of two conserved point-split currents and the combination of a local and a point-split current, both determined on the F6 ensemble. The lower panel of figure 56 shows the the relative difference of both choices for the currents,

which indicates that both are compatible within our current statistical precision, although both variants of the vector current might differ by lattice artefacts.

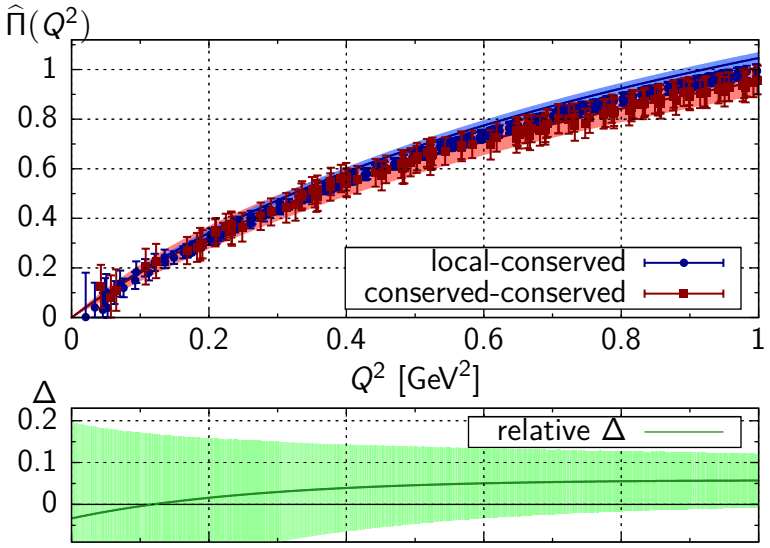

Figure 56: Upper Panel: Comparison of the subtracted vacuum polarisation for the choice of two conserved point-split currents and the combination of a local and point-split current for the vacuum polarisation tensor. Both data sets have been computed on the F6 ensemble with a pion mass of 325 MeV. Lower Panel: Relative difference of both choices for currents

8.2 PARTIALLY TWISTED BOUNDARY CONDITIONS

With periodic boundary conditions, the vacuum polarisation tensor can only be determined on a discrete set of momenta

$$p_i = \frac{2\pi}{L} n_i, p_0 = \frac{2\pi}{T} n_0, \tag{177}$$

which for the largest ensemble (G8), results in a minimal value of the momentum transfer of $Q^2 \sim 0.023\,\text{GeV}^2$. The low momentum region dominates the integral in equation (166), since the kernel $f(Q^2)$ is peaked at small momentum transfer. To achieve a better momentum resolution, we use partially twisted boundary conditions, which were proposed in [39–41] and have already been presented in section 1.6. With partially twisted boundary conditions, the momentum becomes

$$p_i = \frac{2\pi}{L} n_i + \frac{\Theta_i}{L}, \tag{178}$$

which allows us to tune the real-valued parameter Θ_i to achieve, in principle, any momentum transfer. Partially twisted boundary conditions are implemented via a constant $U(1)$ background field, which require a new inversion

of the Dirac operator every time Θ_i is changed. Another feature of twisted boundaries is the removal of the momentum degeneracy: i.e. replacing n_i by $-n_i$ results in a different momentum. Partially twisted boundary conditions are, in principle, only applicable to flavour-non-diagonal quantities, as otherwise the effect of twisting the boundaries cancels. The vacuum polarisation tensor is flavour-diagonal by construction,

$$\Pi_{\mu\nu}(Q) = Z_V \frac{a^4}{4} \sum_n e^{iQ(n+a\hat{\mu}/2)} \operatorname{Tr}\Big[J^c_\mu(n) J^l_\nu(0)\Big] = \tag{179}$$

$$Z_V \frac{a^4}{4} \sum_n e^{iQ(n+a\hat{\mu}/2)} \operatorname{Tr}\Big[\overline{\psi}(n+a\hat{\mu})(1+\gamma_\mu) U^+_\mu(n)\psi(n)\overline{\psi}(0)\gamma_\nu\psi(0)$$

$$- \overline{\psi}(n)(1-\gamma_\mu) U_\mu(n)\psi(x+a\hat{\mu})\overline{\psi}(0)\gamma_\nu\psi(0)\Big].$$

Using iso-spin symmetry, the vacuum polarisation tensor in equation (176) can be reinterpreted as a flavour-non-diagonal object [131, 132]

$$\operatorname{Tr}\Big[J^c_\mu(n) J^l_\nu(0)\Big] = \tag{180}$$

$$= \operatorname{Tr}\Big[\overline{q}_1(n+a\hat{\mu})(1+\gamma_\mu) U^+_\mu(n) q_2(n)\overline{q}_2(0)\gamma_\nu q_1(0)$$

$$- \overline{q}_1(n)(1-\gamma_\mu) U_\mu(n) q_2(x+a\hat{\mu})\overline{q}_2(0)\gamma_\nu q_1(0)\Big]$$

$$= \operatorname{Tr}\Big[\gamma_\nu\gamma_5 S^\dagger_{q_1}(n+a\hat{\mu},0)\gamma_5(1+\gamma_\mu) U^\dagger_\mu(n) S_{q_2}(n,0) \tag{181}$$

$$- \gamma_\nu\gamma_5 S^\dagger_{q_1}(n,0)\gamma_5(1-\gamma_\mu) U_\mu(n) S_{q_2}(n+a\hat{\mu},0)\Big],$$

for which twisted boundary conditions have a non-trivial effect

$$p_i = \frac{2\pi}{L} n_i + \frac{\Theta^i_{q_2} - \Theta^i_{q_1}}{L}. \tag{182}$$

The trick of re-interpreting the currents in terms of different flavours breaks flavour-symmetry and therefore violates the initial condition for the derivation of the point-split current. The associated Ward-Takahashi identities [37, 38] are expected to be violated [135], which will be discussed in the next section. In our implementation, we compute propagators with periodic boundary conditions and use a constant $U(1)$ background field to realise the partially twisted boundary conditions. The propagator $\widetilde{S}_{q_1}(n+a\hat{\mu}, a\hat{\nu})$ is connected to the one with partially twisted boundary conditions $S_{q_1}(n+a\hat{\mu}, a\hat{\nu})$ by a phase

$$\widetilde{S}_{q_1}(n+a\hat{\mu}, a\hat{\nu}) = \exp\left(\mathrm{i}\,\frac{\Theta^\mu_{q_1} - \Theta^\nu_{q_1}}{L}\right) S_{q_1}(n+a\hat{\mu}, a\hat{\nu}). \tag{183}$$

Including the phase factor provides us with the final expression of the vacuum polarisation tensor, which is used in this work:

$$\Pi_{\mu\nu}(Q) = Z_V \frac{a^4}{4} \sum_n e^{iQ(n+a\hat{\mu}/2)} \tag{184}$$
$$\mathrm{Tr}\Big[\exp\left(-\mathrm{i} \frac{\Theta^{\mu}_{q_1}}{L} \right) \gamma_\nu \gamma_5 \widetilde{S}^{\dagger}_{q_1}(n + a\hat{\mu}, 0) \gamma_5 (1+\gamma_\mu) U^{\dagger}_{\mu}(n) \widetilde{S}_{q_2}(n, 0)$$
$$- \exp\left(\mathrm{i} \frac{\Theta^{\mu}_{q_2}}{L} \right) \gamma_\nu \gamma_5 \widetilde{S}^{\dagger}_{q_1}(n, 0) \gamma_5 (1-\gamma_\mu) U_{\mu}(n) \widetilde{S}_{q_2}(n + a\hat{\mu}, 0) \Big].$$

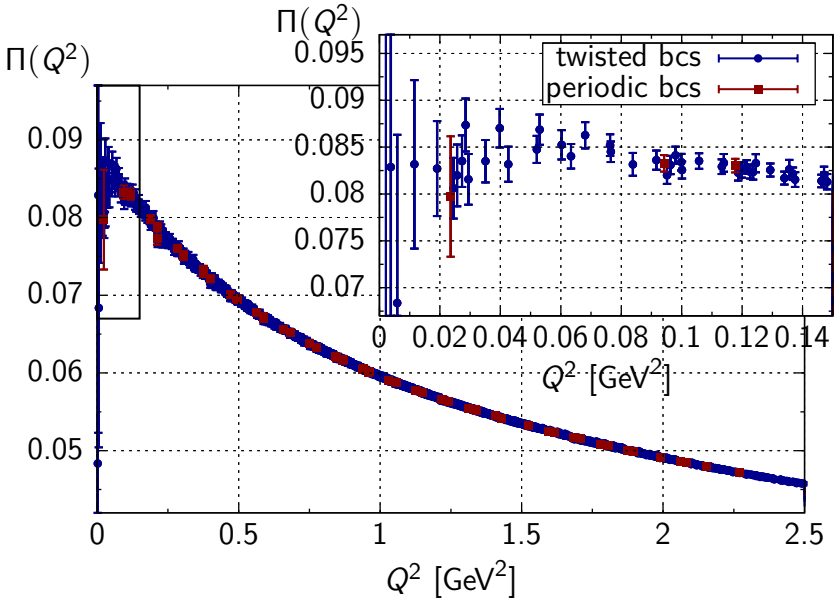

Figure 57: Momentum dependence of the vacuum polarisation using periodic and partially twisted boundary conditions on the G8 ensemble. The inset shows an enlarged image of the low momentum region.

8.3 WARD-TAKAHASHI IDENTITIES

Using two conserved vector currents, $J^c_\mu(n)$ and $J^c_\nu(0)$, in the vacuum polarisation tensor fulfils the Ward-Takahashi identities

$$q_\mu \Pi_{\mu\nu}(Q) = 0 = q_\nu \Pi_{\mu\nu}(Q). \tag{185}$$

For our choice of a local and point-split current in the vacuum polarisation tensor, the Ward-Takahashi identities are still valid for the first index, corresponding to the conserved current. However they are violated by the local current

$$q_\mu \Pi_{\mu\nu}(Q) = 0 \text{ and } q_\nu \Pi_{\mu\nu}(Q) \neq 0. \tag{186}$$

If we combine the point-split vector current with partially twisted boundary conditions, we find that the point-split current is technically not conserved, so we explore the possibility of deriving a conserved vector current in the presence of partially twisted boundary conditions. For this, we consider a general infinitesimal transformation of the fields

$$\psi'(x) = \psi(x)\left(1 - \mathrm{i}\epsilon_\alpha(x)\lambda^\alpha\right) \text{ and } \overline{\psi}'(x) = \overline{\psi}(x)\left(1 + \mathrm{i}\epsilon_\alpha(x)\lambda^\alpha\right), \tag{187}$$

where λ^α is a general flavour matrix. For simplicity, we restrict the following argument to two flavours. Repeating the calculation in section 1.5, a conserved vector current can only be constructed if

$$\left[B_\mu, \lambda^\alpha\right] = 0, \tag{188}$$

where B_μ is the diagonal flavour matrix of the twist applied to the individual flavour

$$B_\mu = \frac{1}{L}\begin{pmatrix} \Theta^1 & 0 \\ 0 & \Theta^2 \end{pmatrix}. \tag{189}$$

The condition in equation (188) implies four choices, for which a conserved vector current can be derived:

(a) $B_\mu \sim \mathbb{1}$,

(b) $\lambda^\alpha = \mathbb{1}$,

(c) $\lambda^\alpha = \left(\begin{smallmatrix} 1 & 0 \\ 0 & -1 \end{smallmatrix}\right)$ and $\lambda^\alpha = \frac{1}{L}\left(\begin{smallmatrix} \Theta^1 & 0 \\ 0 & \Theta^2 \end{smallmatrix}\right)$,

(d) $B_\mu = 0$.

Condition (a) demands that the same twist angle Θ_i is applied equally to all flavours, whilst receiving the freedom of choosing any flavour structure in the vector current. Even with a flavour non-diagonal current, the net effect of twisting will cancel, because all flavours are twisted by the same amount. Condition (b) corresponds to the case of a flavour-diagonal current, in which twisted boundary conditions are not applicable. In case (c), we consider a current with opposite signs in the flavour content, which would result in a vanishing vacuum polarisation tensor for the case of two degenerate quark flavours. The trivial choice (d) is exactly the situation of periodic boundary conditions, in which a flavour-non-diagonal current is conserved and therefore fulfils the Ward-Takahashi identities. We have checked all four conditions numerically. For our calculation, we choose case (b) and re-interpret the current as a flavour-non-diagonal quantity, knowing that this will not give us a strictly conserved current. We calculate the size of the violation of the Ward-Takahashi identities, which is shown in figure 58, determined on the

G8-ensemble using partially twisted boundary conditions with the largest applied twist, i.e. $\Theta = \frac{9}{10}\pi$. The left panel of figure 58 shows the contraction with the first index of the vacuum polarisation tensor, $q_\mu \Pi_{\mu\nu}(Q)$, which corresponds to the conserved vector current. We find that the violation of the Ward-Takahashi identities is in this case statistically compatible with 0 and of the order of $\sim 10^{-5}$. The right part of figure 58 shows the contraction with the index corresponding to the local vector current in the vacuum polarisation tensor, $q_\nu \Pi_{\mu\nu}(Q)$, which violates the Ward-Takahashi identities as expected. The size of this violation is two orders of magnitude larger than for the conserved vector current. With the current statistical precision, an effect of $\sim 10^{-5}$ cannot be resolved, so that our calculation of the vacuum polarisation is not affected.

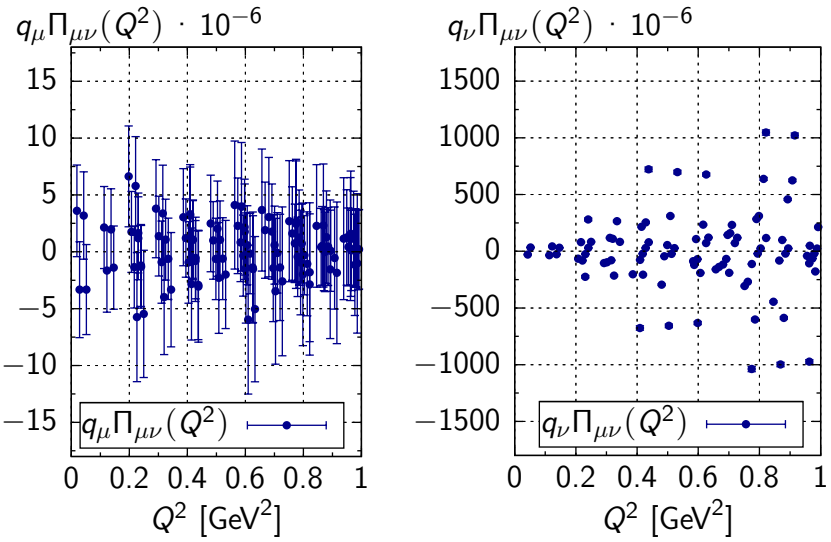

Figure 58: Left: Ward-Takahashi identities for the vacuum polarisation contracted with the conserved point-split vector current. Right: Ward-Takahashi identities in the case of the local vector current.

8.4 FITTING PROCEDURE

The hadronic contribution to the anomalous magnetic moment can be extracted from the convolution integral in equation (166), for which we need a continuous description of the vacuum polarisation, $\Pi(Q^2)$. We use correlated χ^2 fits,

$$\chi^2_{\text{cor}} = \sum_{i=1}^{N_{\text{data}}} \sum_{j=1}^{N_{\text{data}}} \left(f(x_i, \alpha) - y_i\right) C_{ij}^{-1} \left(f(x_j, \alpha) - y_j\right), \tag{190}$$

to model the momentum dependence of the vacuum polarisation in the interval $0 \leq Q^2 \leq Q^2_{\text{max}}$, where Q^2_{max} is the largest momentum obtained in our determination. We vary the fit ansatz to check for systematic differences and use:

Fit A: a model-independent Padé approximation as used in [134, 136] with 6 degrees of freedom (referred to PA[1,2])

$$\Pi(Q^2) = a + Q^2 \left(b + \frac{c}{(Q^2 + d^2)} + \frac{e}{(Q^2 + f^2)} \right), \tag{191}$$

Fit B: a model-independent Padé approximation with a higher number of degrees of freedom and no linear term in the momentum transfer Q^2 (referred to PA[2,2])

$$\Pi(Q^2) = a + Q^2 \left(\frac{b}{(Q^2 + c^2)} + \frac{d}{(Q^2 + e^2)} + \frac{f}{(Q^2 + g^2)} \right), \tag{192}$$

Fit C: a vector dominance model based fit with one mass fixed to the naïve rho-mass, extracted from our simulations, as suggested in [119, 134]

$$\Pi(Q^2) = a + \frac{b}{(Q^2 + m_1^2)} + \frac{c}{(Q^2 + m_\rho^2)}. \tag{193}$$

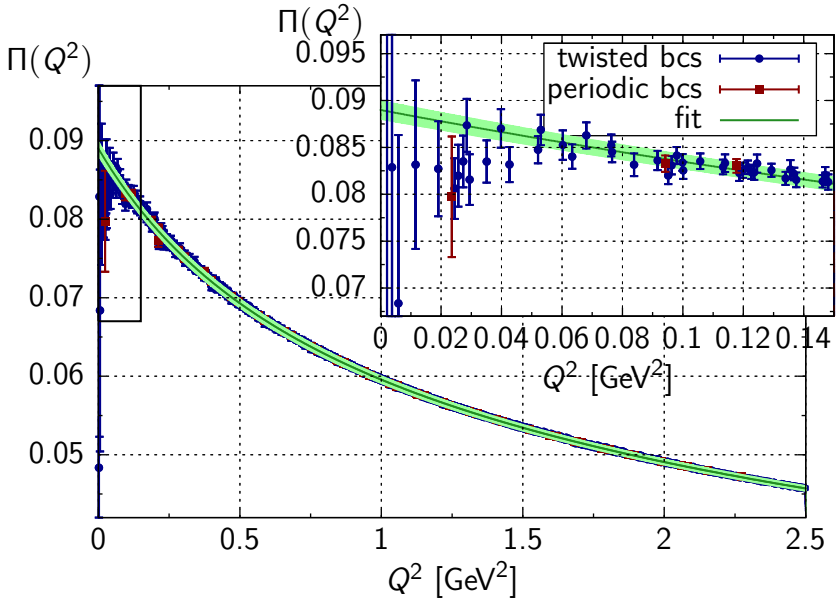

Figure 59: Fit to the momentum dependence of the vacuum polarisation (Fit A) on the G8 ensemble. The upper figure shows an enlarged image of the low momentum region.

We are able to obtain 69 unique momenta using integers in the range of -3 to 3 for the Fourier modes in every direction. Applying three different values for the twist angle Θ, i.e. $\frac{1}{5}\pi$, $\frac{1}{2}\pi$, and $\frac{9}{10}\pi$, we achieve in total six effective twisting angles due to the differences among individual values (compare equation (182)):

$$\frac{2}{10}\pi, \frac{3}{10}\pi, \frac{4}{10}\pi, \frac{5}{10}\pi, \frac{7}{10}\pi \text{ and } \frac{9}{10}\pi. \tag{194}$$

Partially twisted boundary conditions are used in the x-direction only, whereas in all other directions we keep periodic boundary conditions. With this choice, we are able to maintain a good statistical signal for the individual momenta, since part of the momentum degeneracy is preserved. With the six effective twist angles listed in equation (194), we obtain 1581 unique momenta. Correlated fits of such a large number of data points can suffer from instabilities or inconsistencies [137, 138], especially when small eigenvalues of the covariance matrix lead to fits, which do not reproduce the data and therefore correspond to a very large uncorrelated χ^2. Singular value decomposition [139] can help to cut out small eigenvalues, which are statistically not well determined and drive the correlated fit away from the data. In [137], a rule of thumb was suggested to use $M \gtrsim N^2$ for a correlated fit, where M is the number measurements and N the number of degrees of freedom. Therefore, we randomly choose 40 momenta, preferably from the low momentum region, and minimise the corresponding correlated χ^2. We repeat this procedure on different choices of random momenta to check for systematic fluctuations. From a sufficiently large distribution of different fits, we pick the correlated fit, which has the minimal deviation from all 1581 data points. In other words, we select the correlated fit, which corresponds to the minimal uncorrelated χ^2 computed on the full set of data points. Figure 59 shows the result of such a correlated Padé fit for the G8 ensemble, which provides a very good description over the full momentum range. Figure 60 shows the distribution of a_μ^{hvp} for different choices of the 40 random momenta. The red line indicates the preferred fit chosen and the red band represents the statistical uncertainty, estimated using 1000 bootstrap samples. The central part of the distribution is well covered by the error band. Only a few fits lead to values outside the estimated uncertainties, which is expected when we assume a normal distribution for a_μ^{hvp}.

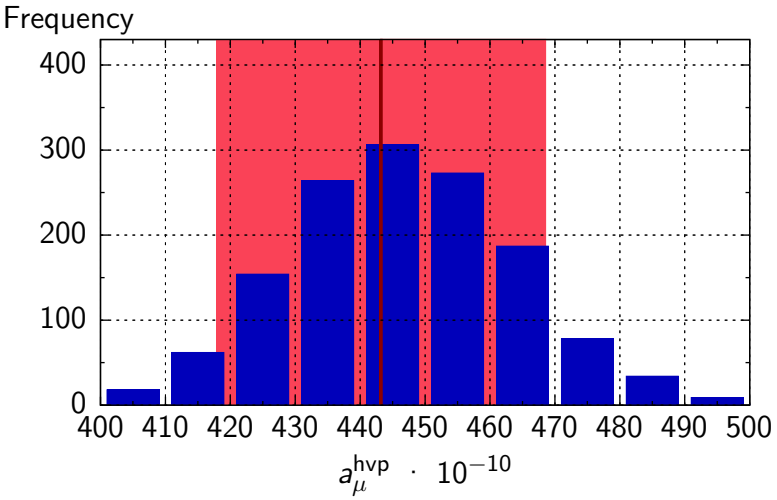

Figure 60: Histogram of the fit results (Fit A) on the G8 ensemble. The red line indicates the chosen fit with the estimated statistical uncertainty.

8.5 NUMERICAL INTEGRATION

The hadronic vacuum polarisation of $(g-2)_\mu$ is determined numerically by evaluating the integral

$$a_\mu^{\text{hvp}} = \left(\frac{\alpha}{\pi}\right)^2 \int_0^\infty \frac{1}{Q^2} f(Q^2)\, \hat{\Pi}(Q^2)\, \mathrm{d}Q^2, \tag{195}$$

where $f(Q^2)$ is given in equation (168). In this work we use the "QAG adaptive integration" routine of the GNU Scientific Library (GSL) [140] with the accuracy criterion set to absolute 10^{-15} or relative 10^{-7} precision, whichever occurs first. The numerical integration has been cross-checked by the "NIntegrate" routine of Mathematica® [141]. In the region of $0 \leq Q^2 \leq 4\,\text{GeV}^2$, we use the correlated fit for the subtracted vacuum polarisation. At larger momenta $Q^2 > 4\,\text{GeV}^2$, we use leading-order perturbation theory [142] in the $\overline{\text{MS}}$-scheme with the scale set to $\mu = 2\,\text{GeV}$. Although perturbation theory is available in next-to-leading order, our intention is to use perturbation theory in the high-Q^2 regime, where the difference between one- and two-loop is negligible. In other words, we do not intend to model the intermediate or small momentum region by perturbation theory. The leading-order expression is straightforward to apply in the case of two light flavours and a partially quenched strange quark, since no internal fermion loops appear. We use the non-perturbatively determined renormalisation factors and $\Lambda_{\overline{\text{MS}}}$ parameter from [33, 143–145] to evaluate the leading-order expression.

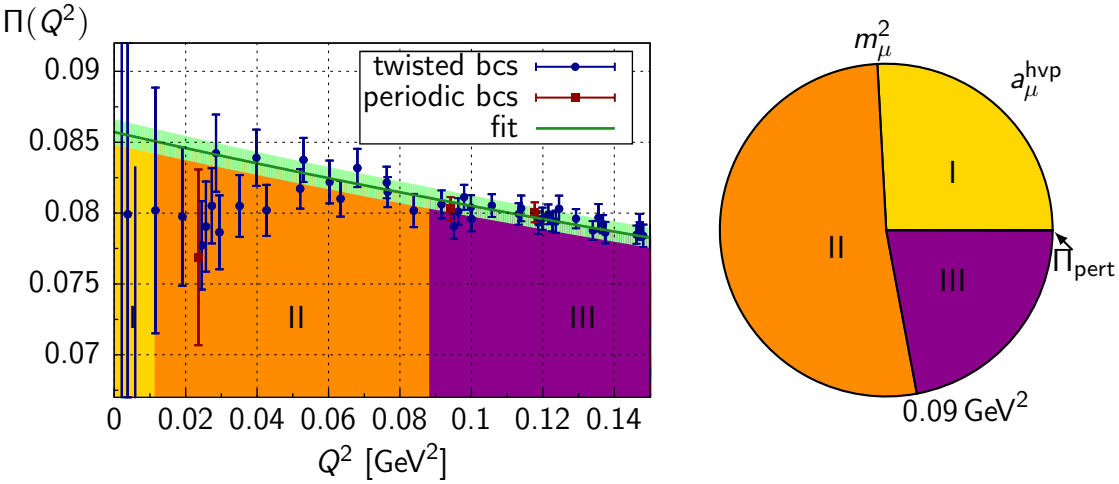

Figure 61: Left: Small-momentum dependence of the vacuum polarisation (Fit A) on the G8 ensemble, separated into different regions (I-III). Right: Pie chart of the corresponding contributions to a_μ^{hvp}

We have divided the momentum range into four separate parts to study the individual contributions to a_μ^{hvp}. The left side of figure 61 shows again the

correlated fit to the vacuum polarisation for the G8-ensemble on the small momentum range (green band). The first region includes the momentum range from 0 to the muon mass squared m_μ^2, which contains only a few data points with rather large statistical uncertainties. The second range (II) is set from m_μ^2 to $0.09\,\mathrm{GeV}^2$, which is dominated by data points using partially twisted boundary conditions. The third region (III) covers the region from $0.09\,\mathrm{GeV}^2$ to $4\,\mathrm{GeV}^2$, in which both choices for boundary conditions result in a good description. From $4\,\mathrm{GeV}^2$ perturbation theory is used to obtain the remaining contribution to a_μ^{hvp}. The pie chart on the right side of figure 61 displays the contribution of each momentum region to a_μ^{hvp}. The full integrand is shown in figure 62, where the points indicate the momenta, which can be reached by either periodic or partially twisted boundary conditions, and do not correspond to actual data. It is clear from both plots that small momenta dominate the overall determination of a_μ^{hvp}. The advantage of twisted boundary conditions consists in a significant gain in the momentum resolution at small momenta. Unfortunately, the statistical accuracy deteriorates for small values of Q^2. Region II is much better constrained thanks to the additional data points provided by partially twisted boundary conditions. The region above $0.1\,\mathrm{GeV}^2$ is sampled by a large number of data points resulting in a reliable description of the vacuum polarisation. The contribution to a_μ^{hvp} from the high momentum region, i.e. above $Q > 2\,\mathrm{GeV}$, is below 0.07% and therefore negligible.

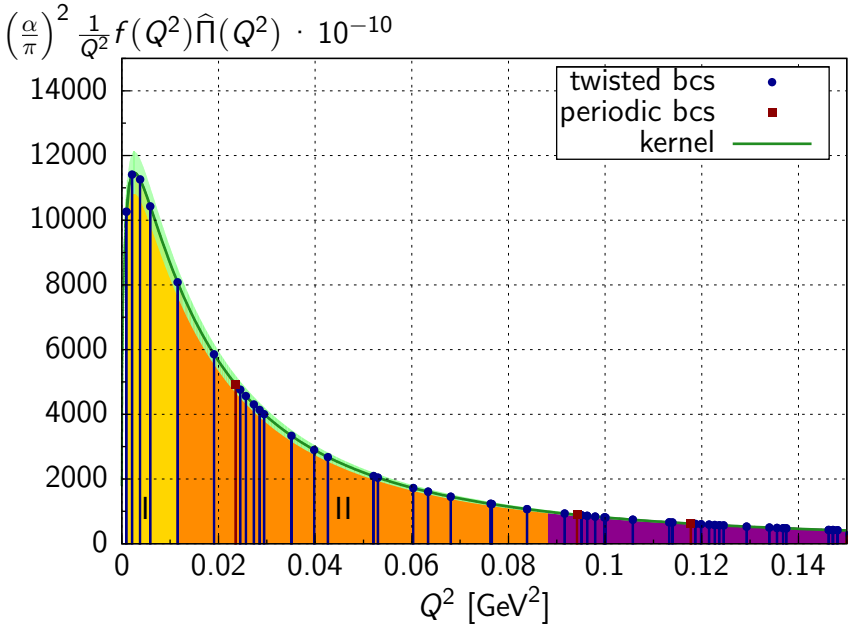

Figure 62: The integrand of equation (195) for the determination of a_μ^{hvp} on the G8 ensemble. The momentum ranges are chosen as in figure 61 and the points only indicate the momenta which can be realised by periodic and partially twisted boundary conditions.

9

RESULTS

The leading hadronic contribution to $(g-2)_\mu$ has been computed on the CLS configurations listed in table 7. These ensembles allow us to perform the chiral extrapolation and estimate the remaining uncertainties such as cutoff and and finite-size effects. We have computed the hadronic vacuum polarisation of the muon using two dynamical light quarks. The contribution of a strange quark to the hadronic vacuum polarisation is determined using a partially quenched strange quark. Results for the two- and three flavour calculations will be shown in the next section.

Label	a [fm]	m_π [MeV]	L [fm]	κ_s	# meas.
A3	0.079	473	2.5	0.135457	260
A4	0.079	363	2.5	0.135312	249
A5	0.079	312	2.5	0.135186	215
E5	0.063	456	2.0	0.135955	1000
F6	0.063	325	3.0	0.135724	294
F7	0.063	277	3.0	0.135708	249
G8	0.063	193	4.0	0.135678	408
N5	0.050	430	2.4	0.136293	179
N6	0.050	332	2.4	0.136220	223
O7	0.050	261	3.2	0.136200	262

Table 7: Summary of lattice and input parameters for $(g-2)_\mu$ calculation. The lattice spacings a and the strange hopping parameters κ_s are taken from [24, 146].

9.1 HADRONIC VACUUM POLARISATION IN $N_f = 2$

Figure 63 and table 8 show the result of the leading hadronic contribution to the anomalous magnetic moment of the muon determined on the ensembles used in this study. The relative statistical accuracy varies from $\sim 2\%$ on the E5

ensemble to $\sim 8\%$ on the F7 ensemble. When approaching the physical pion mass, it becomes more difficult to achieve a statistically precise estimate of the vacuum polarisation for $(g-2)_\mu$, and so more measurements are necessary to achieve a comparable accuracy. The numerical effort increases even further, when we simulate with lighter pion masses and larger volumes. All data points show a good overall agreement. We find an unexpected downward trend for the most chiral ensemble. The G8 ensembles is the only ensemble in our study, in which the rho meson can decay. Further studies are needed in order to asses whether the downwards trend is a systematic effect or a statistical fluctuation.

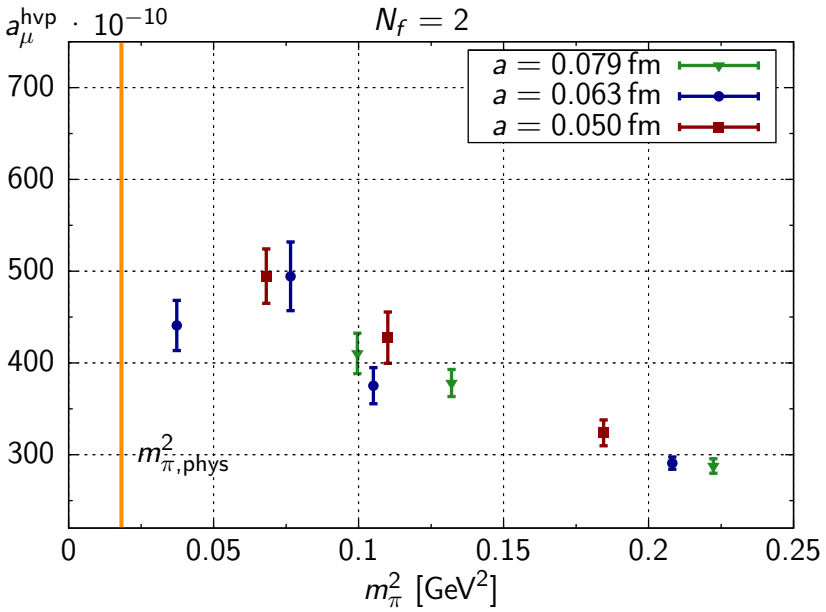

Figure 63: Results for a_μ^{hvp} using two dynamical flavour plotted as function of m_π^2 using Fit A. The colours indicate different lattice spacing.

9.2 HADRONIC VACUUM POLARISATION IN $N_f = 2 + 1_Q$

In order to be relevant for the comparison with the value from phenomenology the hadronic vacuum polarisation must be computed for all quarks. One expects the contribution from the light quarks u, d, and s to dominate. The inclusion of a partially quenched strange quark allows us to estimate the contribution of a strange quark to the anomalous magnetic moment of the muon. The contribution from a charm quark is neglected all-together, but this is expected to be a small effect. We compute the strange quark propagator on a sea of two light quarks, which approximates the three-flavour case. This procedure neglects the contribution of strange quarks from the sea and is called *partial quenching*. The necessary strange hopping parameter κ_s has been determined in [24] and is listed in table 7. Taking the charges of the quarks into account, we expect the contribution of the strange quark to be smaller than $\frac{1}{5}$ of the contribution from the two light flavours, since the strange quark is significantly

$N_f = 2$

	Fit A		Fit B		Fit C	
Labels	a_μ^{hvp}	χ^2_{unc}	a_μ^{hvp}	χ^2_{unc}	a_μ^{hvp}	χ^2_{unc}
A3	283.2(7.8)	0.041	283.7(11.4)	0.042	285.3(6.5)	0.041
A4	373.5(14.6)	0.074	370.3(23.1)	0.100	340.7(10.7)	0.089
A5	405.9(21.8)	0.062	386.0(19.5)	0.063	379.9(12.4)	0.059
E5	287.6(6.6)	0.088	292.9(8.0)	0.084	296.7(5.6)	0.088
F6	360.8(18.9)	0.292	363.4(15.3)	0.241	368.4(12.5)	0.255
F7	476.0(36.1)	0.086	482.6(34.5)	0.089	446.0(17.7)	0.097
G8	424.9(26.3)	0.122	422.2(25.5)	0.122	441.3(20.4)	0.122
N5	319.2(13.9)	0.015	323.4(16.9)	0.016	346.9(10.0)	0.014
N6	422.4(27.7)	0.065	414.8(17.6)	0.071	415.0(10.6)	0.062
O7	489.4(29.3)	0.084	472.2(24.3)	0.087	460.3(16.7)	0.085

Table 8: Result for a_μ^{hvp} for various fits in the two-flavour theory.

heavier than light u- and d-quarks. Figure 64 and table 9 show the corresponding three flavour result. The contribution of a partially quenched strange quark is, as expected, small but not negligible. We find that the relative contribution of the strange quark decreases when the pion mass is lowered. The overall picture of the data is similar to the two flavour case and demonstrates the need for improved statistics in the region of small pion masses.

9.3 CHIRAL BEHAVIOUR

Currently, all our ensembles are simulated with unphysically heavy pion masses, thus an extrapolation to the physical pion mass is required. In [134], we have seen a non-trivial chiral behaviour and therefore used a fit inspired by chiral perturbation theory. In this work, we use the same ansatz and compare it to a linear fit on a reduced pion mass range:

Fit A: $a_\mu^{\text{hvp}}(m_\pi^2) = A + B\, m_\pi^2 + C\, m_\pi^2 \ln(\frac{m_\pi^2}{\Lambda^2})$,

Fit B: $a_\mu^{\text{hvp}}(m_\pi^2) = A + B\, m_\pi^2$, with $m_\pi \leq 365\,\text{MeV}$.

Since further study is needed in our most chiral ensemble, we perform the chiral fits with and without the G8 ensemble and address the differences in the chiral uncertainty. Figure 65 show the results of the chiral fits A and B without the G8 ensemble.

To check systematic differences in the chiral extrapolation, we compare our result to an alternative method of extrapolation towards to the physical point,

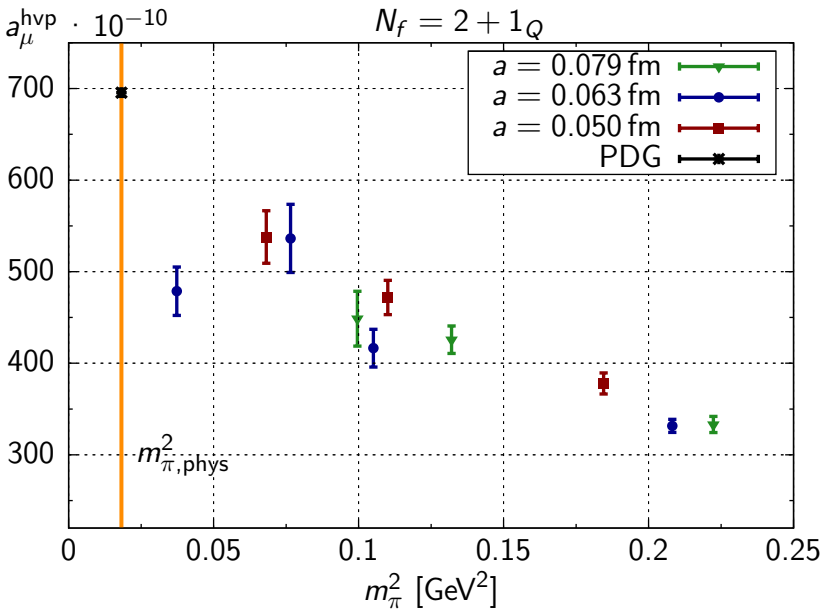

Figure 64: Results (Fit A) for a_μ^{hvp} using two dynamical flavours and a partially quenched strange quark plotted as function of m_π^2. The colours correspond to different lattice spacings. The value from the PDG [47] is plotted for illustration only.

	$N_f = 2+1_Q$					
	Fit A		Fit B		Fit C	
Labels	a_μ^{hvp}	χ^2_{unc}	a_μ^{hvp}	χ^2_{unc}	a_μ^{hvp}	χ^2_{unc}
A3	327.9(8.7)	0.041	329.3(9.3)	0.043	333.0(7.8)	0.041
A4	420.5(14.8)	0.070	426.6(26.3)	0.137	389.0(12.1)	0.078
A5	426.9(25.8)	0.058	425.7(19.3)	0.055	431.5(13.4)	0.057
E5	327.9(7.1)	0.089	331.1(8.5)	0.084	345.5(6.9)	0.092
F6	400.6(19.8)	0.268	403.2(15.1)	0.248	406.8(12.8)	0.199
F7	516.3(35.8)	0.081	526.6(35.6)	0.080	501.1(21.9)	0.088
G8	461.4(25.5)	0.112	479.0(26.2)	0.115	487.6(21.4)	0.115
N5	365.1(11.0)	0.015	371.1(15.3)	0.014	397.9(11.8)	0.015
N6	466.3(18.5)	0.063	466.2(16.7)	0.068	472.6(11.4)	0.061
O7	532.3(28.4)	0.072	513.5(26.7)	0.077	510.4(18.2)	0.069

Table 9: Summary of different fit results for a_μ^{hvp} using the $N_f = 2+1_Q$ calculation.

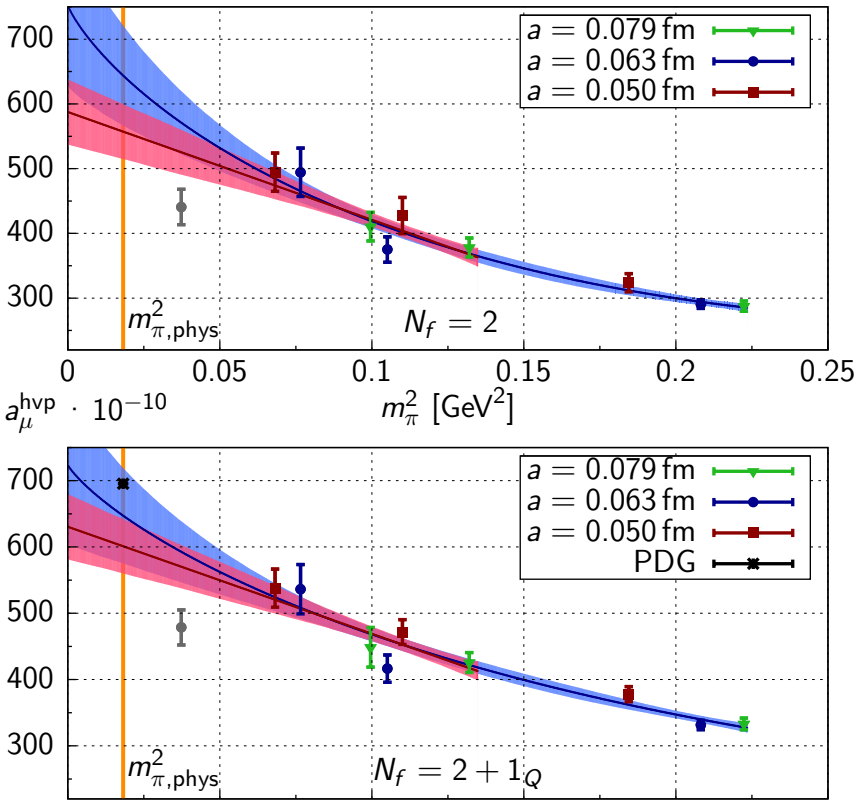

Figure 65: Fit of the chiral behaviour by an ansatz motivated by chiral perturbation theory (Fit A). The top part shows the two flavour results, the lower panel the three flavour result.

which was introduced in [118] with the aim of reducing the pion mass dependence. Following [134], the alternative method can be understood in the context of a vector dominance model. Assuming

$$\hat{\Pi}^{\mathrm{vmd}}(Q^2) \sim g_V^2 \frac{Q^2}{Q^2 + m_V^2(m_\pi^2)} \tag{196}$$

for the subtracted vacuum polarisation, the hadronic vacuum polarisation becomes

$$a^{\mathrm{hvp}}_{\mu,\mathrm{vmd}} \sim \left(\frac{\alpha}{\pi}\right)^2 \int_0^\infty \frac{1}{Q^2} f(Q^2)\, \hat{\Pi}^{\mathrm{vmd}}(Q^2)\, \mathrm{d}Q^2 \sim g_V^2 \frac{m_\mu^2}{m_V^2(m_\pi^2)}. \tag{197}$$

The quantity g_V^2 is the ratio of the decay constant and the mass in the vector and shows a negligible dependence on the pion mass [118]. By transforming the squared momentum via

$$Q'^2 \to Q^2 \frac{m_\rho^2}{m_V^2} \tag{198}$$

in the integration kernel $f(Q^2)$, one can suppress the influence of the pion mass, i.e.,

$$a^{\text{hvp}}_{\mu,\text{vmd}} \sim g_V^2 \frac{m_\mu^2}{m_\rho^2}. \tag{199}$$

It is important to note that in the physical limit $\frac{m_\rho^2}{m_V^2} \to 1$ the hadronic vacuum polarisation approaches the correct physical limit. Using the transformation in equation (198), the explicit dependence on the lattice scale a cancels [118]. Figure 66 shows a comparison of fit B using the standard approach and the rescaled integration for a_μ^{hvp}. As expected, the pion-mass dependence has been reduced.

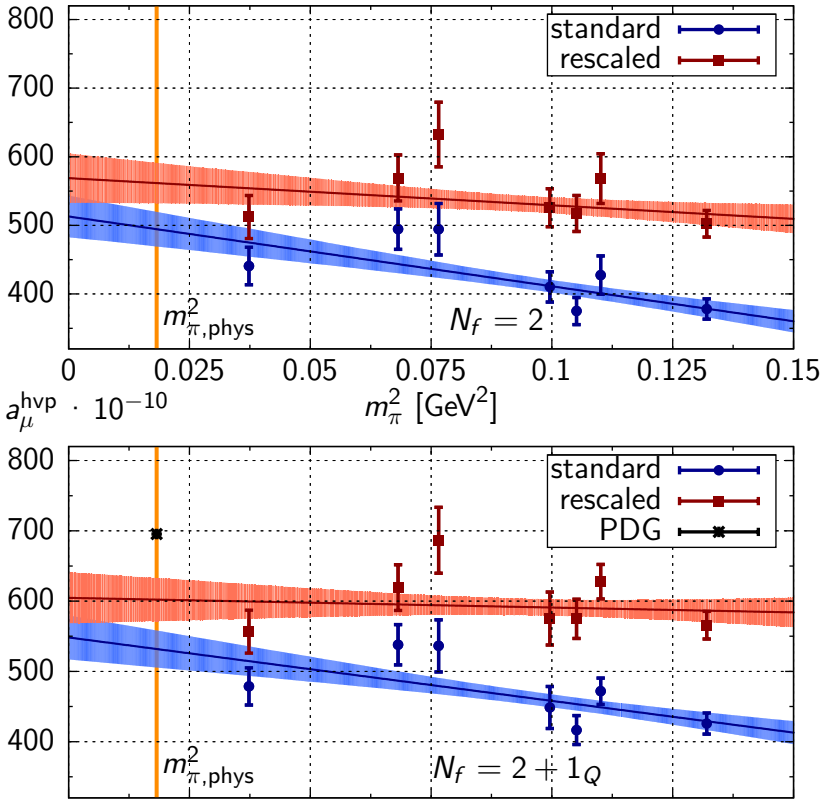

Figure 66: Comparison of two different chiral extrapolations using a fit B in both data set. The "rescaled" values have been obtained by changing the momentum of the integration kernel $f(Q^2)$ by a factor of $\frac{m_\rho^2}{m_V^2}$.

A comparison of the various chiral extrapolations using fits A and B is shown in figure 67. We take half of the difference between the fit A with and without the G8 ensemble as an estimate for the remaining uncertainties from the chiral extrapolation.

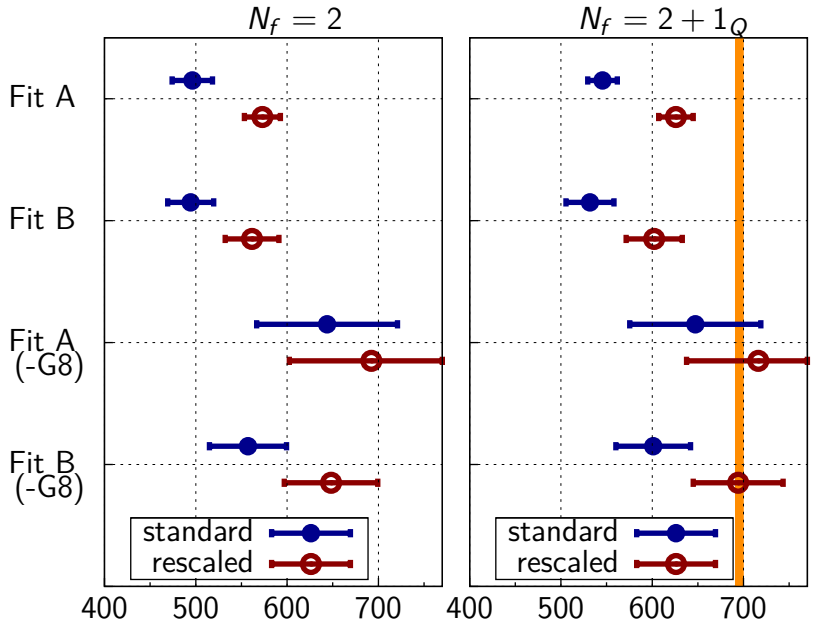

Figure 67: Comparison of the chiral extrapolations using fit A and B with and without the G8 ensemble. The left panel shows the two flavour results, the right panel the three flavour result. The orange line indicates the value from the PDG.

9.4 CUTOFF EFFECTS

We expect the vacuum polarisation tensor to receive $\mathcal{O}(a)$ corrections, although our action is non-perturbatively $\mathcal{O}(a)$ improved, since only on-shell quantities are $\mathcal{O}(a)$ improved [134]. To estimate the size of the remaining cutoff effects, we compare the subtracted vacuum polarisation for two ensembles, which have similar pion masses and volumes. We choose the F7 and O7 ensemble, since we want to study lattice artefacts in the proximity of the physical pion mass. Figure 68 shows in the upper panel the subtracted vacuum polarisation, the corresponding fits and error-bands. The lower panel of figure 68 illustrates the relative difference of the fits to both ensembles. With the current precision, lattice artefacts are negligible for this specific set of ensembles. To check for cutoff effects further, we perform a combined fit to the chiral behaviour and the lattice spacing by adding a linear term in the lattice spacing to the chiral fits, for instance for fit A so we use:

$$a_\mu^{\mathrm{hvp}}(m_\pi^2) = A + B\,(m_\pi)^2 + D\,a. \tag{200}$$

The results of those combined fits are shown in figure 69, in which we plotted the results with $a \to 0$. The combined fit increases the statistical uncertainties, but shows only little indication of cutoff effects. We choose the result from the combined fit B including the G8 ensemble as a final estimate of the leading hadronic contribution to the anomalous magnetic moment of the muon. This

fit is statistically compatible with the other fits shown in figure 69 and includes an estimate of cutoff effects by construction.

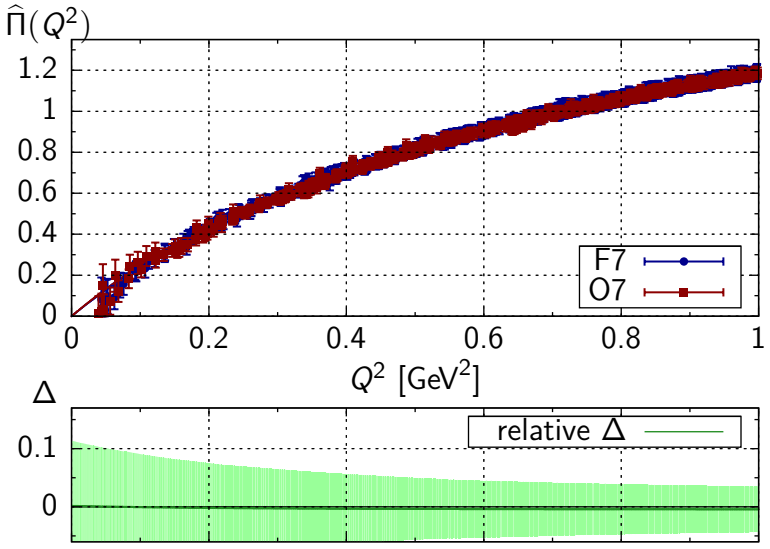

Figure 68: Study of cutoff effects on $\widehat{\Pi}(Q)$ for the F7 and O7 ensemble with similar pion masses and spacial extent.

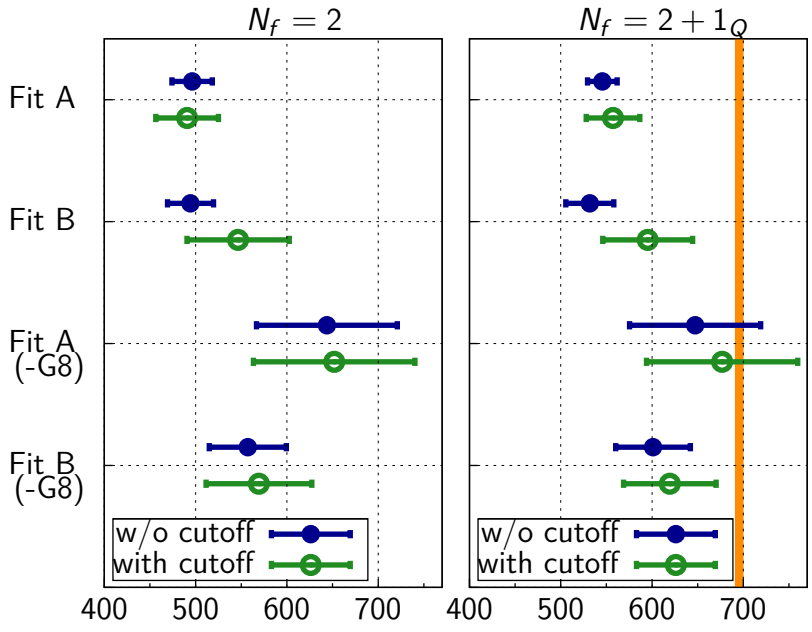

Figure 69: Comparison of the chiral extrapolation with and without a linear term in the lattice spacing. The left panel shows the fit results for the two-flavour calculation and the right part corresponds to the three-flavour calculation.

9.5 FINITE-SIZE EFFECTS

In our determination of the hadronic vacuum polarisation, we only use ensembles which have a value of $m_\pi L \geq 4$ and so finite-size effects are expected to be small [6], but still need to be checked numerically. We check finite-size effects by comparing the subtracted vacuum polarisation for a set of ensembles which only differ in the size of the volume, such as the E5 and $D5$ ensemble, where the $D5$ ensemble is a smaller version ($L = 24 \leftrightarrow L = 32$) of the E5 ensemble. Unfortunately the smaller $D5$ ensemble does not fulfil the condition of $m_\pi L \geq 4$, which indeed leads to a discrepancy of the order of $\sim 10\%$. Figure 70 shows in the upper panel the subtracted vacuum polarisation for both ensembles. In the lower panel of figure 70 the discrepancy is visible. Note that the fit to the smaller volume seems to miss data points in the low-momentum region, which indicates an even stronger discrepancy. The D5 ensemble is not suitable to check finite-size effects, since the volume is small, so that finite size effects are expected. Therefore, we compare the E5 and A3 ensembles in figure 71 which have approximately the same pion mass and different lattice spacings. If we assume small cutoff effects as seen before, we find that finite-size effects are small in this range of pion masses. Ideally, one would like to compare two ensembles close to the physical pion mass with the same setup but different volumes. If both ensembles fulfil the rule of thumb of $m_\pi L \geq 4$, the larger ensemble would be numerically very expensive. Currently, there is no ideal candidate on the CLS ensembles to check volume effects close to the physical pion mass.

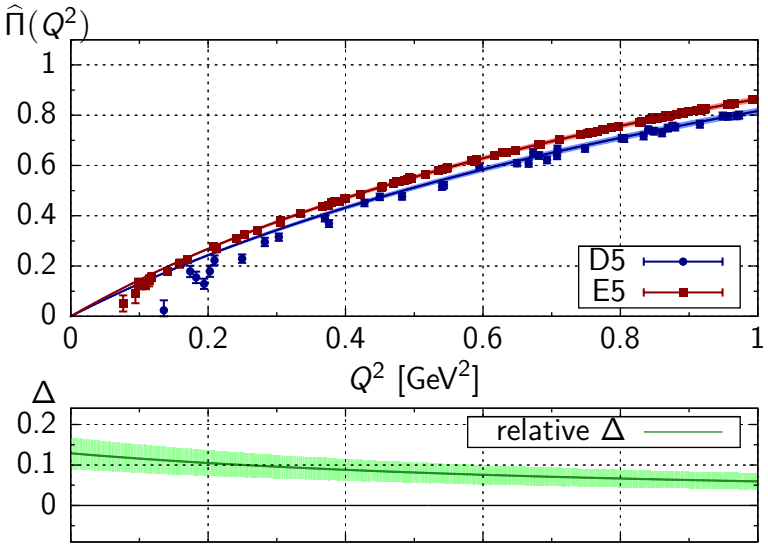

Figure 70: Study of finite-size effects on $\widehat{\Pi}(Q)$ for the E5 and $D5$ ensemble with identical setup but different spacial extent.

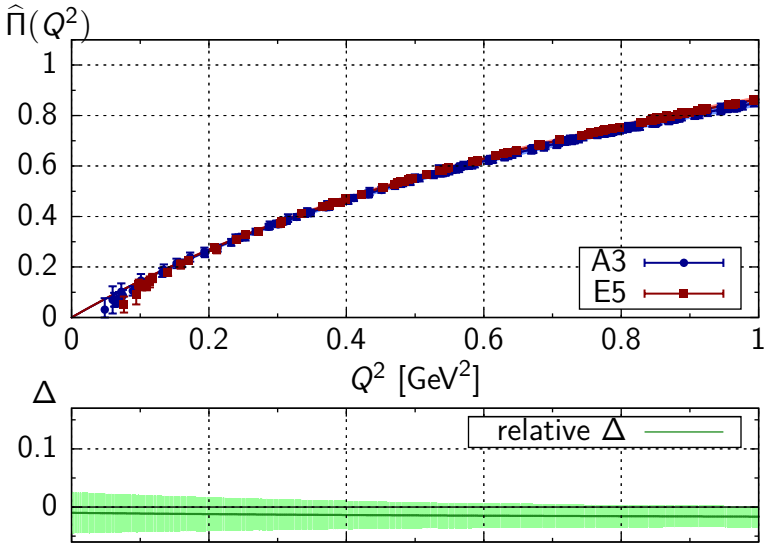

Figure 71: Comparison of the result for $\widehat{\Pi}(Q)$ on the E5 and A3 ensemble, which differ in the spacial extent and the lattice spacing.

9.6 FIT UNCERTAINTIES - Q^2 DEPENDENCE

The hadronic contribution to the anomalous magnetic moment cannot be extracted directly from a lattice simulations. A fit on the momentum dependence needs to be performed in order to extrapolate the lattice data and obtain a continuous description of the vacuum polarisation. Since only little is known for the vacuum polarisation, various fits are pursued to estimate the systematic uncertainty introduced by the fits. The various fit ansätze have been presented in section 8.4 and are commonly used by the lattice community [119, 121, 124, 126]. Figure 72 shows the result for the three fits used in this study, where as the bare numbers are listed in tables 8 and 9. The data points have been separated in order to distinguish the result for the different fit functions. The individual linear fits indicate that the three fits used in this work are compatible within the current statistical precision. Nevertheless, we use half of the spread of the fits A-C as an estimate for the systematic uncertainties arising from the fit ansatz in the description of the Q^2-dependence.

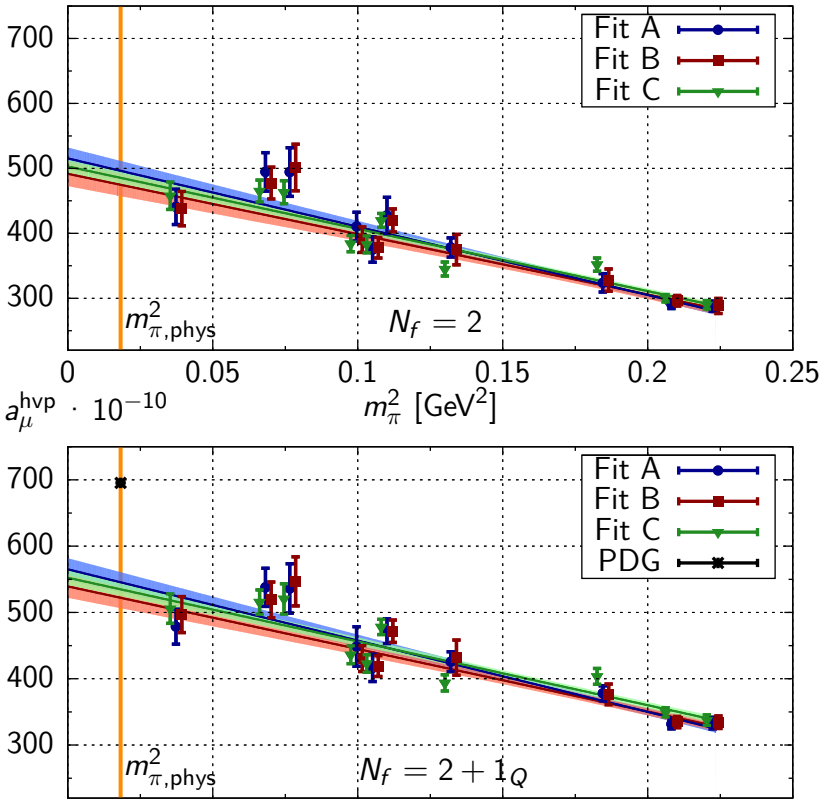

Figure 72: Comparison of the chiral behaviour for different fit ansätze.

10

CONCLUSIONS AND OUTLOOK

In the previous chapters, we have presented a lattice calculation of the leading hadronic vacuum polarisation contribution to the anomalous magnetic moment of the muon using two dynamical flavours. We have restricted this calculation to quark-connected diagrams. The contribution of the strange quark has been computed by adding a partially quenched strange quark to our two-flavour simulation. We have shown that partially twisted boundary conditions can be applied to our calculation, even though the vacuum polarisation tensor is a flavour-diagonal quantity. Partially twisted boundary conditions improve the momentum resolution of $\Pi(Q^2)$, as seen in figures 61 and 62. The improved momentum resolution does not reduce the statistical uncertainties, but enhances our confidence in the fit of momentum dependence of the vacuum polarisation. All systematic uncertainties of the lattice approach have been discussed and included in our error budget. If we used the combined chiral fit presented in section 9.4 and add the estimated uncertainties, we obtain a value for a_μ^{hvp} of

$$a_\mu^{\text{hvp}}\,[N_f = 2] = 546.5\,(56.0)^{\text{stat}}(74.7)^{\text{chiral}}(10.8)^{\text{fits}} \cdot 10^{-10}, \tag{201}$$

$$a_\mu^{\text{hvp}}\,[N_f = 2 + 1_Q] = 595.3\,(49.3)^{\text{stat}}(57.7)^{\text{chiral}}(11.7)^{\text{fits}} \cdot 10^{-10}. \tag{202}$$

The statistical error also includes lattice artefacts by performing a combined fit including cutoff effects in the chiral extrapolation. Adding the errors in quadrature, we achieve a total precision of 17% for the case of two flavours and 13% if we include a strange quark. The size of the uncertainties can be understood by looking at the individual precision of the data points, which are of compatible precision. The statistical uncertainties grow significantly, when we simulate with lighter pion masses. The chiral extrapolation currently dominates our uncertainties, which is caused by an unexpected trend seen on our lightest ensemble. In order to corroborate the chiral behaviour we need to improve the accuracy of the ensembles close to the physical point, or ideally simulate with a physical pion mass. The uncertainties of the lattice spacing a, which we use in this work as input, are partially included in the chiral extrapolation, since we compare to a scale-independent determination of a_μ^{hvp} (compare section 9.3).

Currently, we are investigating a technique which allows us to obtain a continuous description of the subtracted vacuum polarisation [122, 123, 147–149]. For small momentum transfer $Q_0^2 \to 0$, we can relate

$$\Pi(Q_0^2) - \Pi(0) = \int_0^\infty \mathrm{d}x_0 \, G(x_0) \left(x_0^2 - \frac{4}{Q_0^2} \sin^2\left(\frac{1}{2} Q_0 x_0\right) \right) \tag{203}$$

to an integral of a "*mixed-representation*" correlator $G(x_0)$

$$G(x_0)\delta_{kl} = -\int \mathrm{d}^3x \, \mathrm{Tr}\left(J_k(x_0, \vec{x}) J_l(0)\right) \tag{204}$$

and an analytic function with the complete momentum behaviour. The integral in equation (203) can be evaluated analytically using a combination of lattice data for the vector correlator $G(x_0)$ and the fitted asymptotic behaviour.

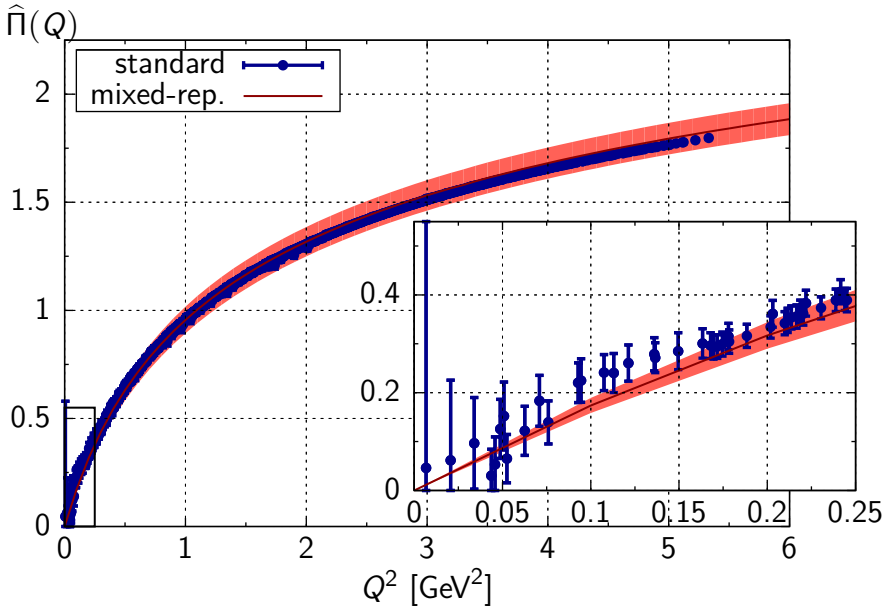

Figure 73: Comparison as in [123] of $\widehat{\Pi}(Q^2)$ for the F6 ensemble using the "standard" method and using the time-like vector correlator.

Figure 73 compares both ways of determining the subtracted vacuum polarisation on the F6 ensemble as shown in [123]. The results look very promising, since both methods agree very well within their statistical errors. The mixed-representation vector correlator provides a continuous description of the momentum behaviour of the subtracted vacuum polarisation, which we can use to improve the very low momentum region of $\Pi(Q^2)$, in which even partially twisted boundary conditions fail to provide reliable information.

In [120], Divitiis et al. have proposed a direct computation of the vacuum polarisation at vanishing momentum, $\Pi(0)$, which would remove the necessary extrapolation and would allow us to compute the subtracted vacuum

polarisation directly. We are currently adding the necessary operators into our simulation code, so that we can determine $\Pi(0)$ for our ensembles.

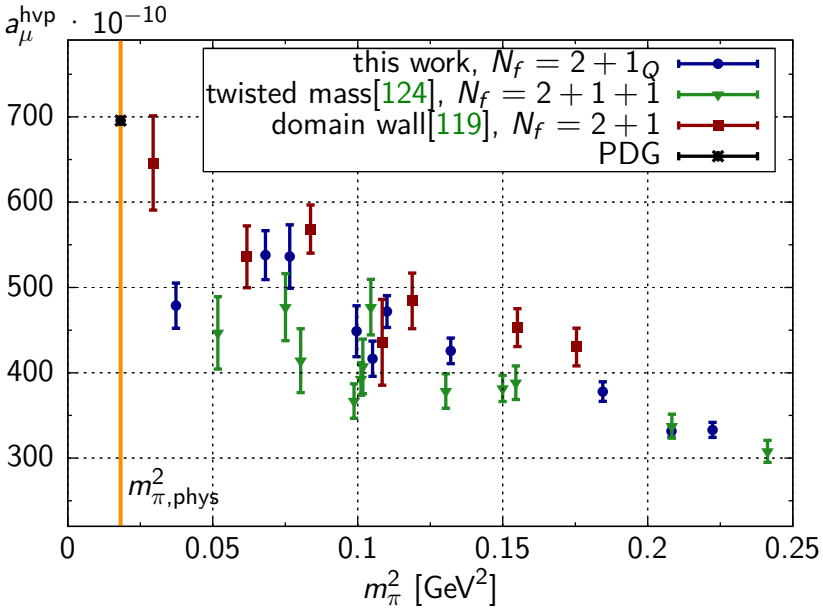

Figure 74: Comparison of the three flavour results of a_μ^{hvp} from various lattice groups [119, 124].

Figure 74 shows a comparison of the most recent results for the hadronic vacuum polarisation determined by various lattice groups [119, 124]. The overall agreement is quite remarkable considering that the groups use different setups including various lattice actions. Also the technical details used to extract a_μ^{hvp} differ among these groups. The comparison suggests that there is very little, if any, dependence on the number of flavours.

Currently, the most precise estimate of the hadronic vacuum polarisation of the muon is obtained by using $e^+e^- \to$ hadrons data [47], which provides an accuracy of 0.6% (compare section 7.2.3)

$$a_\mu^{\mathrm{hvp}}\,[\mathrm{PDG}] = 692.3(4.2) \cdot 10^{-10}. \tag{205}$$

At the moment, our calculation of the leading hadronic contributions to $(g-2)_\mu$ shows a discrepancy with the value obtained by phenomenology. If we take our final value seriously, this would enhance the discrepancy seen between the experimental determination and the theoretical prediction of the anomalous magnetic moment of the muon. However, our calculation is at this stage not complete. Contributions from disconnected diagrams are expected to be small, but need to be checked numerically. We plan to use a stochastic estimate of the all-to-all propagator in combination with a generalised hopping parameter expansion to determine the remaining disconnected diagrams [150].

This approach was successfully used in the case of the scalar pion form factor [151].

The ETMC collaboration [124] sees indication for a non-negligible contribution of a charm quark. Despite the large mass of the charm quark, the charge factor of the charm, $z_c^2 = \frac{4}{9}$, enhances the charm contribution on the vacuum polarisation. The raw data in figure 74 do not differ significantly from our values computed with a partially quenched strange quark, nor from the $2+1$ flavour calculation of RBC/UKCQD, which contradicts the statement from ETMC to some extent. Lattice calculations of the leading hadronic contributions to $(g-2)_\mu$ are still at an early stage, further improvements are necessary to improve the overall accuracy by an order of magnitude. Iso-spin breaking effects have so far been neglected and might become relevant, once the lattice calculation achieves a sub-percent precision.

Part IV

APPENDIX

A

APPENDIX

A.1 GAMMA MATRICES

In this work, we use the gamma matrices in the Euclidean chiral representation [6]:

$$\gamma_0 = \begin{pmatrix} 0 & 0 & -1 & 0 \\ 0 & 0 & 0 & -1 \\ -1 & 0 & 0 & 0 \\ 0 & -1 & 0 & 0 \end{pmatrix}, \gamma_1 = \begin{pmatrix} 0 & 0 & 0 & -i \\ 0 & 0 & -i & 0 \\ 0 & i & 0 & 0 \\ i & 0 & 0 & 0 \end{pmatrix}, \tag{206}$$

$$\gamma_2 = \begin{pmatrix} 0 & 0 & 0 & -1 \\ 0 & 0 & 1 & 0 \\ 0 & 1 & 0 & 0 \\ -1 & 0 & 0 & 0 \end{pmatrix}, \gamma_3 = \begin{pmatrix} 0 & 0 & -i & 0 \\ 0 & 0 & 0 & i \\ i & 0 & 0 & 0 \\ 0 & -i & 0 & 0 \end{pmatrix}, \tag{207}$$

$$\gamma_5 = \gamma_0\gamma_1\gamma_2\gamma_3 = \begin{pmatrix} 1 & 0 & 0 & 0 \\ 0 & 1 & 0 & 0 \\ 0 & 0 & -1 & 0 \\ 0 & 0 & 0 & -1 \end{pmatrix}. \tag{208}$$

A.2 HEAVY BARYON CHIRAL PERTURBATION THEORY FIT

The nucleon axial charge can be fitted by an ansatz using Heavy Baryon Chiral Perturbation Theory in the small scale expansion with Δ degrees of freedom [102, 103]

$$\begin{aligned} g_A(m_\pi^2) = g_A^0 - \frac{(g_A^0)^3 m_\pi^2}{16\pi^2 f_\pi^2} + 4\Bigg(& C_{SSE}(\lambda) + \frac{c_A^2}{4\pi^2 f_\pi^2}\left[\frac{155}{972}g_1 - \frac{17}{36}g_A^0\right] \\ & + \frac{1}{16\pi^2 f_\pi^2}\left(\frac{50}{81}c_A^2 g_1 - \frac{1}{2}g_A^0 - \frac{2}{9}c_A^2 g_A^0 - (g_A^0)^3\right)\ln\frac{m_\pi}{\lambda}\Bigg) m_\pi^2 \\ & + \frac{4c_A^2 g_A^0}{27\pi^2 f_\pi^2 \Delta_0} m_\pi^2 + \frac{8}{27\pi^2 f_\pi^2} c_A^2 g_A^0 m_\pi^2 \sqrt{1 - \frac{m_\pi^2}{\Delta_0^2}}\, R(m_\pi) \\ & + \frac{c_A^2 \Delta_0^2}{81\pi^2 f_\pi^2}(25 g_1 - 57 g_A^0)\left(\ln\frac{2\Delta_0}{m_\pi} - \sqrt{1 - \frac{m_\pi^2}{\Delta_0^2}}\ln R(m_\pi)\right), \end{aligned} \tag{209}$$

where the function $R(m_\pi)$ is defined as

$$R(m_\pi) = \left(\frac{\Delta_0}{m_\pi} + \sqrt{\frac{\Delta_0^2}{m_\pi^2} - 1}\right). \tag{210}$$

We fix three parameters to their values in phenomenology as suggested in [60]:

$$c_A = 1.5\,\text{GeV}\ ,\ \Delta_0 = 0.2711\,\text{GeV and}\ \lambda = 1\,\text{GeV}. \tag{211}$$

The resulting fit depends on three fit parameters, which are g_A^0, f_π and $C_{SSE}(\lambda)$.

The expressions for the radii $\langle r_1^2\rangle$ and $\langle r_2^2\rangle$ have been derived in [152], which are

$$\begin{aligned} \langle r_1^2\rangle = & -\frac{1}{(4\pi f_\pi)^2}\left(1 + 7g_A^2 + (10g_A^2 + 2)\ln\left(\frac{m_\pi}{\lambda}\right)\right) - \frac{12 B_{10}^{(r)}(\lambda)}{(4\pi f_\pi)^2} \\ & + \frac{c_A^2}{54\pi^2 f_\pi^2}\left(26 + 30\ln\left(\frac{m_\pi}{\lambda}\right) + 30\frac{\Delta_0}{\sqrt{\Delta_0^2 - m_\pi^2}}\ln\left(R(m_\pi)\right)\right) \end{aligned} \tag{212}$$

and

$$\begin{aligned} \langle r_2^2\rangle = & \frac{g_A^2 m_N}{8\pi m_\pi f_\pi^2 \kappa(m_\pi)} + \frac{24 m_N B_{c2}}{\kappa(m_\pi)} \\ & + \frac{c_A^2 m_N}{9\pi^2 f_\pi^2 \kappa(m_\pi)\sqrt{\Delta_0^2 - m_\pi^2}}\ln\left(R(m_\pi)\right). \end{aligned} \tag{213}$$

These formulae can be combined to obtain an expression for the electric and magnetic radii

$$\langle r_E^2 \rangle = \langle r_1^2 \rangle + \frac{3\kappa}{2m_N^2}, \tag{214}$$

$$\langle r_M^2 \rangle = \langle r_1^2 \rangle + \frac{\langle r_1^2 \rangle + \kappa \langle r_2^2 \rangle}{1+\kappa}, \tag{215}$$

where the anomalous magnetic moment of the nucleon is given by

$$\begin{aligned}\kappa = \kappa^0 &- \frac{g_A^2 m_\pi m_N}{4\pi f_\pi^2} - 8E_1^{(r)}(\lambda) m_N m_\pi^2 + \frac{4c_A c_V g_A m_N m_\pi^3}{27\pi f_\pi^2 \Delta_0} \\ &+ \frac{2c_A^2 \Delta_0 m_N}{9\pi^2 f_\pi^2}\left(\sqrt{1-\frac{m_\pi^2}{\Delta_0^2}}\ln(R(m_\pi)) + \ln\left(\frac{m_\pi}{2\Delta_0}\right)\right) \\ &+ \frac{4c_A c_V g_A m_N m_\pi^2}{9\pi^2 f_\pi^2}\ln\left(\frac{2\Delta_0}{\lambda}\right) - \frac{8c_A c_V g_A \Delta_0^2 m_N}{27\pi^2 f_\pi^2}\times \\ &\left(\left(1-\frac{m_\pi^2}{\Delta_0^2}\right)^{\frac{3}{2}}\ln(R(m_\pi)) + \left(1 - \frac{3m_\pi^2}{2\Delta_0^2}\ln\left(\frac{m_\pi}{2\Delta_0}\right)\right)\right).\end{aligned} \tag{216}$$

LIST OF FIGURES

Figure 1 Self-interaction of gluons . . . 3
Figure 2 Pictorial representation of the lattice Λ . . . 5
Figure 3 Pictorial representation of the plaquette $P_{\mu\nu}$ . . . 6
Figure 4 Pictorial representation of the clover-leaf $Q_{\mu\nu}$ . . . 8
Figure 5 Bootstrap error procedure . . . 10
Figure 6 Properties of the gauge configurations . . . 12
Figure 7 Experimental determination of G_E . . . 20
Figure 8 Overview over lattice calculations of g_A . . . 21
Figure 9 Overview over lattice calculations of r_1 . . . 22
Figure 10 Overview over lattice calculations of κ . . . 22
Figure 11 Overview over lattice calculations of $\langle x \rangle_{u-d}$ . . . 23
Figure 12 General three-point function . . . 25
Figure 13 Schematic of the two-point function of the pion . . . 27
Figure 14 Effective mass of the pion . . . 28
Figure 15 Schematic of the two-point function of the nucleon . . . 29
Figure 16 Effective mass of the nucleon . . . 30
Figure 17 Three-point Wick contractions . . . 32
Figure 18 Extended propagator in the three-point function . . . 32
Figure 19 Computation of three-point function . . . 33
Figure 20 Shape of a smeared source . . . 35
Figure 21 Comparison of smeared and point correlator . . . 36
Figure 22 Ratios of the nucleon axial charge . . . 38
Figure 24 Summed operator insertion method . . . 40
Figure 25 Influence of statistics on excited states . . . 41
Figure 26 Momentum behaviour of the $F_1(Q^2)$ plateaus . . . 42
Figure 27 Dipole fit for $G_E(Q^2)$ . . . 43
Figure 28 Dipole fit for $G_M(Q^2)$ . . . 43
Figure 29 Results of nucleon axial charge . . . 47
Figure 30 Chiral behaviour of the axial charge . . . 48
Figure 31 Comparison of chiral extrapolations . . . 48
Figure 32 Study of cutoff effects . . . 50
Figure 33 Comparison of chiral extrapolations . . . 50
Figure 34 Study of finite-size effects . . . 51
Figure 35 The electric radius of the nucleon . . . 54
Figure 36 The magnetic radius of the nucleon . . . 55
Figure 37 Ratio of G_M and F_1 . . . 56
Figure 38 The anomalous magnetic moment of the nucleon . . . 56
Figure 39 Chiral behaviour of $\langle r_E^2 \rangle$ . . . 58

Figure 40 Chiral behaviour of $\langle r_M^2 \rangle$ . . . 59
Figure 41 Chiral behaviour of κ . . . 60
Figure 42 Study of cutoff and finite-size effects . . . 61
Figure 43 Study of cutoff and finite-size effects . . . 61
Figure 44 Comparison of the axial charge . . . 63
Figure 45 Average quark momentum fraction . . . 65
Figure 46 Schematic of experimental setup on $(g-2)_\mu$ . . . 70
Figure 47 Weak decay pattern of the muon . . . 70
Figure 48 Leading QED contribution to $(g-2)_\mu$ . . . 71
Figure 49 Lowest order weak diagrams to $(g-2)_\mu$ . . . 72
Figure 50 Hadronic vacuum polarisation diagram for $(g-2)_\mu$. 73
Figure 51 Schematic of the Optical Theorem . . . 73
Figure 52 Light-by-light scattering diagram for $(g-2)_\mu$. . . . 75
Figure 53 Comparison of the individual SM contribution . . . 75
Figure 54 Hadronic vacuum polarisation diagram for $(g-2)_\mu$. 77
Figure 55 Wick-contractions of the hadronic vacuum polarisation 78
Figure 56 Comparison of different choices for vector currents . 80
Figure 57 Momentum dependence of the vacuum polarisation . 82
Figure 58 Ward-Takahashi identities for the vacuum polarisation 84
Figure 59 Momentum dependence fit of the vacuum polarisation 85
Figure 60 Histogram of the fit results . . . 86
Figure 61 Contribution of several momentum ranges to a_μ^{hvp} . . 87
Figure 62 The integrand for a_μ^{hvp} . . . 88
Figure 63 Two flavour results for a_μ^{hvp} . . . 90
Figure 64 Three flavour results for a_μ^{hvp} . . . 92
Figure 65 Chiral behaviour of a_μ^{hvp} . . . 93
Figure 66 Comparison of standard and rescaled chirals fits . . . 94
Figure 67 Comparison of various chiral extrapolations . . . 95
Figure 68 Study of cutoff effects on the F7 and O7 ensemble . 96
Figure 69 Chiral extrapolation including lattice artefacts . . . 96
Figure 70 Study of finite-size effects for E5 and $D5$ ensemble . 97
Figure 71 Study of finite-size effects for E5 and A3 ensemble . 98
Figure 72 Comparison of the different fit ansätze . . . 99
Figure 73 Comparison of time-like and standard correlator . . . 102
Figure 74 Results for a_μ^{hvp} from different lattice groups . . . 103

LIST OF TABLES

Table 1 Gauge configurations 11
Table 2 Fit results of the axial charge 40
Table 3 Summary of input parameters for form factor calculation 46
Table 4 Results for the axial charge of the nucleon 46
Table 5 Results for the electro-magnetic radii 57
Table 6 Results for anomalous magnetic moment κ 58
Table 7 Summary of lattice and input parameters for $(g-2)_\mu$ 89
Table 8 Result for a_μ^{hvp} for various fits $(N_f = 2)$ 91
Table 9 Result for a_μ^{hvp} for various fits $(N_f = 2 + 1_Q)$ 92

BIBLIOGRAPHY

[1] D. J. Gross and F. Wilczek, *Ultraviolet behavior of non-abelian gauge theories*, *Physical Review Letters* 30 (1973) 1343–1346.

[2] M. Creutz, *Quarks, gluons, and lattices*. Cambridge University Press, 1983.

[3] I. Montvay and G. Münster, *Quantum Fields on a Lattice*. Cambridge University Press, 1997.

[4] J. Smit, *Introduction to Quantum Fields on a Lattice*. Cambridge University Press, 2002.

[5] H. Wittig, *QCD on the lattice*, in *Landolt-Börnstein New Series I 21A*. Springer, Berlin, 2008.

[6] C. Gattringer and C. B. Lang, *Quantum Chromodynamics on the Lattice*. Springer, Berlin, 1st ed., 2010.

[7] Y. Iwasaki, *Renormalization Group Analysis of Lattice Theories and Improved Lattice Action. II. Four-dimensional non-Abelian SU(N) gauge model*, *arXiv preprint 1111.7054* (2011).

[8] K. G. Wilson, *Confinement of quarks*, *Phys. Rev. D* 10 (1974) 2445.

[9] H. B. Nielsen and M. Ninomiya, *A no-go theorem for regularizing chiral fermions*, *Physics Letters B* 105 (1981) 219 – 223.

[10] K. Symanzik, *Continuum limit and improved action in lattice theories:(I). Principles and ϕ^4 theory*, *Nuclear Physics B* 226 (1983) 187 – 204.

[11] K. Symanzik, *Continuum limit and improved action in lattice theories:(II). O(N) non-linear sigma model in perturbation theory*, *Nuclear Physics B* 226 (1983) 205 – 227.

[12] B. Sheikholeslami and R. Wohlert, *Improved continuum limit lattice action for QCD with wilson fermions*, *Nuclear Physics B* 259 (1985) 572 – 596.

[13] K. Jansen and R. Sommer, *O(a) improvement of lattice QCD with two flavors of Wilson quarks*, *Nucl.Phys.* B530 (1998) 185–203.

[14] L. Susskind, *Lattice fermions*, *Phys. Rev. D* 16 (1977) 3031–3039.

[15] H. Neuberger, *Exactly massless quarks on the lattice*, *Physics Letters B* 417 (1998) 141–144.

[16] H. Neuberger, *More about exactly massless quarks on the lattice*, *Physics Letters B* 427 (1998) 353–355.

[17] D. B. Kaplan, *A method for simulating chiral fermions on the lattice*, *Physics Letters B* 288 (1992) 342 – 347.

[18] A. Shindler, *Twisted mass lattice QCD*, *Physics Reports* 461 (2008) 37–110.

[19] G. Colangelo, S. Dürr, A. Jüttner, L. Lellouch, H. Leutwyler, et al., *Review of lattice results concerning low-energy particle physics*, *The European Physical Journal C* 71 (2011) 1–76.

[20] S. Aoki, Y. Aoki, C. Bernard, T. Blum, G. Colangelo, et al., "Review of lattice results concerning low energy particle physics." `http://itpwiki.unibe.ch/flag/images/4/4b/FLAG.pdf`, Jul, 2013.

[21] B. Efron, *Bootstrap methods: another look at the jackknife*, *The Annals of Statistics* 7 (1979) 1–26.

[22] M. H. Quenouille, *Notes on bias in estimation*, *Biometrika 43* (1956).

[23] J. W. Tukey, *Bias and confidence in not quite large samples.*, *Annls. Math. Stat. 29* (1958).

[24] S. Capitani, M. Della Morte, G. von Hippel, B. Knippschild, and H. Wittig, *Scale setting via the Ω baryon mass*, *PoS* LATTICE2011 (2011) 145.

[25] `https://twiki.cern.ch/twiki/bin/view/CLS/WebIntro`, Nov, 2013.

[26] M. Lüscher, *Computational Strategies in Lattice QCD*, *Les Houches Summer School: Session* 93 (2011) 331–399.

[27] M. Lüscher, *Schwarz-preconditioned HMC algorithm for two-flavour lattice QCD*, *Comput. Phys. Commun.* 165 (2005) 199–220.

[28] M. Lüscher, *Solution of the Dirac equation in lattice QCD using a domain decomposition method*, *Computer physics communications* 156 (2004) 209–220.

[29] M. Marinkovic and S. Schaefer, *Comparison of the mass preconditioned HMC and the DD-HMC algorithm for two-flavour QCD*, *PoS* LATTICE2010 (2010) 031.

[30] S. Duane, A. D. Kennedy, B. J. Pendleton, and D. Roweth, *Hybrid Monte Carlo*, *Physics Letters B* 195 (1987) 216 – 222.

[31] M. Hasenbusch and K. Jansen, *Speeding up lattice QCD simulations with clover improved Wilson fermions*, *Nucl.Phys.* B659 (2003) 299–320.

[32] M. Della Morte, R. Hoffmann, F. Knechtli, R. Sommer, and U. Wolff, *Non-perturbative renormalization of the axial current with dynamical Wilson fermions*, *JHEP* 0507 (2005) 007.

[33] M. Della Morte, R. Sommer, and S. Takeda, *On cutoff effects in lattice QCD from short to long distances*, *Phys.Lett.* B672 (2009) 407–412.

[34] S. Sint and P. Weisz, *Further results on O(a) improved lattice QCD to one loop order of perturbation theory*, *Nucl.Phys.* B502 (1997) 251–268.

[35] S. Capitani, M. Della Morte, G. von Hippel, B. Jäger, A. Jüttner, et al., *The nucleon axial charge from lattice QCD with controlled errors*, *Phys.Rev.* D86 (2012) 074502.

[36] W. Kürzinger, *Untersuchung der Vakuumpolarisation auf dem Gitter*. PhD thesis, Freie Universität Berlin, 2001.

[37] J. C. Ward, *An identity in Quantum Electrodynamics*, *Phys. Rev.* 78 (Apr, 1950) 182.

[38] Y. Takahashi, *On the generalized Ward identity*, *Nuovo Cim.* 6 (1957).

[39] P. F. Bedaque, *Aharonov-Bohm effect and nucleon nucleon phase shifts on the lattice*, *Phys.Lett.* B593 (2004) 82–88.

[40] G. de Divitiis, R. Petronzio, and N. Tantalo, *On the discretization of physical momenta in lattice QCD*, *Phys.Lett.* B595 (2004) 408–413.

[41] C. Sachrajda and G. Villadoro, *Twisted boundary conditions in lattice simulations*, *Phys.Lett.* B609 (2005) 73–85.

[42] M. Breidenbach, J. I. Friedman, H. W. Kendall, E. D. Bloom, D. H. Coward, H. DeStaebler, et al., *Observed behavior of highly inelastic electron-proton scattering*, *Phys. Rev. Lett.* 23 (Oct, 1969) 935–939.

[43] M. N. Rosenbluth, *High energy elastic scattering of electrons on protons*, *Phys. Rev.* 79 (Aug, 1950) 615–619.

[44] J. Bernauer, M. Distler, J. Friedrich, T. Walcher, P. A. C. A. Gayoso, et al., *The electric and magnetic form factors of the proton*, *arXiv preprint 1307.6227* (2013).

[45] R. Pohl, A. Antognini, F. Nez, F. D. Amaro, F. Biraben, et al., *The size of the proton*, *Nature* 466 (Jul, 2010) 213–216.

[46] P. J. Mohr, B. N. Taylor, and D. B. Newell, *CODATA recommended values of the fundamental physical constants: 2010*, *Reviews of Modern Physics* 84 (2012) 1527.

[47] J. Beringer, J.-F. Arguin, R.M. Barnett, K. Copic, O. Dahl, et al. (Particle Data Group), *Review of particle physics*, *Phys. Rev. D* 86 (2012) 010001.

[48] S. Syritsyn, "Hadron structure review." `http://www.lattice2013.uni-mainz.de/presentations/Plenaries%20Thursday/Syritsyn.pdf`, Jul, 2013.

[49] D. Dolgov, R. Brower, S. Capitani, P. Dreher, J. Negele, et al., *Moments of nucleon light cone quark distributions calculated in full lattice QCD*, *Phys.Rev.* D66 (2002) 034506.

[50] S. Ohta and K. Orginos, *Nucleon structure with domain wall fermions*, *Nucl.Phys.Proc.Suppl.* 140 (2005) 396–398.

[51] R. Edwards, G. Fleming, P. Hägler, J. Negele, K. Orginos, et al., *The Nucleon axial charge in full lattice QCD*, *Phys.Rev.Lett.* 96 (2006) 052001.

[52] A. A. Khan, M. Göckeler, P. Hägler, T. Hemmert, R. Horsley, et al., *Axial coupling constant of the nucleon for two flavours of dynamical quarks in finite and infinite volume*, *Phys.Rev.* D74 (2006) 094508.

[53] H.-W. Lin, T. Blum, S. Ohta, S. Sasaki, and T. Yamazaki, *Nucleon structure with two flavors of dynamical domain-wall fermions*, *Phys.Rev.* D78 (2008) 014505.

[54] T. Yamazaki, Y. Aoki, T. Blum, H.-W. Lin, M. Lin, et al., *Nucleon axial charge in 2+1 flavor dynamical lattice QCD with domain wall fermions*, *Phys.Rev.Lett.* 100 (2008) 171602.

[55] T. Yamazaki, Y. Aoki, T. Blum, H.-W. Lin, M. Lin, et al., *Nucleon form factors with 2+1 flavor dynamical domain-wall fermions*, *Phys.Rev.* D79 (2009) 114505.

[56] G. Engel, C. Gattringer, L. Y. Glozman, C. Lang, M. Limmer, et al., *Baryon axial charges from Chirally Improved fermions: First results*, *PoS* LAT2009 (2009) 135.

[57] M. Göckeler, P. Hägler, R. Horsley, Y. Nakamura, D. Pleiter, et al., *Lattice Investigations of Nucleon Structure at Light Quark Masses*, *PoS* LAT2009 (2009) 125.

[58] J. Bratt, R. Edwards, M. Engelhardt, P. Hägler, H.-W. Lin, et al., *Nucleon structure from mixed action calculations using 2+1 flavors of asqtad sea and domain wall valence fermions*, *Phys.Rev.* D82 (2010) 094502.

[59] S. Capitani, B. Knippschild, M. Della Morte, and H. Wittig, *Systematic errors in extracting nucleon properties from lattice QCD*, *PoS* LATTICE2010 (2010) 147.

[60] C. Alexandrou, M. Brinet, J. Carbonell, M. Constantinou, P. Harraud, et al., *Axial Nucleon form factors from lattice QCD*, *Phys.Rev.* D83 (2011) 045010.

[61] S. Collins, M. Göckeler, P. Hägler, T. Hemmert, R. Horsley, et al., *Nucleon form factors and structure functions from $N(f) = 2$ Clover fermions*, *PoS* LATTICE2010 (2010) 153.

[62] M. Göckeler, P. Hägler, R. Horsley, Y. Nakamura, D. Pleiter, et al., *Baryon Axial Charges and Momentum Fractions with $N_f = 2 + 1$ Dynamical Fermions*, *PoS* LATTICE2010 (2010) 163.

[63] H.-W. Lin, *Lattice Hadron Structure: Applications within and beyond QCD*, *PoS* LATTICE2012 (2012) 013.

[64] J. Green, M. Engelhardt, S. Krieg, J. Negele, A. Pochinsky, et al., *Nucleon Structure from Lattice QCD Using a Nearly Physical Pion Mass*, *arXiv preprint 1209.1687* (2012).

[65] B. J. Owen, J. Dragos, W. Kamleh, D. B. Leinweber, M. S. Mahbub, et al., *Variational Approach to the Calculation of gA*, *Phys.Lett.* B723 (2013) 217–223.

[66] J. Green, M. Engelhardt, S. Krieg, J. Negele, A. Pochinsky, et al., *Nucleon structure with pion mass down to 149 MeV*, *PoS* LATTICE2012 (2012) 170.

[67] C. Alexandrou, M. Constantinou, V. Drach, K. Hatziyiannakou, K. Jansen, et al., *Nucleon Structure using lattice QCD*, *arXiv preprint 1303.6818* (2013).

[68] T. Bhattacharya, S. D. Cohen, R. Gupta, A. Joseph, and H.-W. Lin, *Nucleon Charges and Electromagnetic Form Factors from 2+1+1-Flavor Lattice QCD*, *arXiv preprint 1306.5435* (2013).

[69] M. Lin, *Status of nucleon structure calculations with 2+1 flavors of domain wall fermions*, *PoS* LATTICE2012 (2012) 172.

[70] R. Horsley, Y. Nakamura, A. Nobile, P. Rakow, G. Schierholz, et al., *Nucleon axial charge and pion decay constant from two-flavor lattice QCD*, *arXiv preprint 1302.2233* (2013).

[71] C. Alexandrou, *Hadron Structure and Form Factors*, *PoS* LATTICE2010 (2010) 001.

[72] S. Collins, M. Göckeler, P. Hägler, R. Horsley, Y. Nakamura, et al., *Dirac and Pauli form factors from lattice QCD*, *Phys.Rev.* D84 (2011) 074507.

[73] C. Alexandrou, M. Brinet, J. Carbonell, M. Constantinou, P. Harraud, et al., *Nucleon electromagnetic form factors in twisted mass lattice QCD*, *Phys.Rev.* D83 (2011) 094502.

[74] S. Capitani, M. Della Morte, G. von Hippel, B. Jäger, B. Knippschild, et al., *Excited state systematics in extracting nucleon electromagnetic form factors*, *PoS* LATTICE2012 (2012) 177.

[75] C. Alexandrou, M. Constantinou, S. Dinter, V. Drach, K. Jansen, et al., *Nucleon form factors and moments of generalized parton distributions using $N_f = 2 + 1 + 1$ twisted mass fermions*, *Phys.Rev.* D88 (2013) 014509.

[76] S. Capitani, M. Della Morte, G. von Hippel, B. Jäger, B. Knippschild, et al., *Excited state systematics in extracting nucleon electromagnetic form factors from the lattice*, *PoS* ConfinementX (2012) 321.

[77] S. Capitani, M. Della Morte, D. Djukanovic, G. von Hippel, B. Jäger, et al., *A high-statistics study of the nucleon EM form factors, axial charge and quark momentum fraction*, *PoS* LATTICE2013 (2013) 272.

[78] S. Syritsyn, J. Bratt, M. Lin, H. Meyer, J. Negele, et al., *Nucleon Electromagnetic Form Factors from Lattice QCD using 2+1 Flavor Domain Wall Fermions on Fine Lattices and Chiral Perturbation Theory*, *Phys.Rev.* D81 (2010) 034507.

[79] Y. Aoki, T. Blum, H.-W. Lin, S. Ohta, S. Sasaki, et al., *Nucleon isovector structure functions in (2+1)-flavor QCD with domain wall fermions*, *Phys.Rev.* D82 (2010) 014501.

[80] D. B. Renner, *Status and prospects for the calculation of hadron structure from lattice QCD*, *PoS* LAT2009 (2009) 018.

[81] C. Alexandrou, J. Carbonell, M. Constantinou, P. Harraud, P. Guichon, et al., *Moments of nucleon generalized parton distributions from lattice QCD*, *Phys.Rev.* D83 (2011) 114513.

[82] G. S. Bali, S. Collins, M. Deka, B. Glassle, M. Göckeler, et al., $\langle x \rangle_{u-d}$ *from lattice QCD at nearly physical quark masses*, *Phys.Rev.* D86 (2012) 054504.

[83] A. Sternbeck, M. Göckeler, P. Hägler, R. Horsley, Y. Nakamura, et al., *First moments of the nucleon generalized parton distributions from lattice QCD*, *PoS* LATTICE2011 (2011) 177.

[84] G. Martinelli and C. T. Sachrajda, *A Lattice Study of Nucleon Structure*, *Nucl.Phys.* B316 (1989) 355.

[85] S. Dinter, C. Alexandrou, M. Constantinou, V. Drach, K. Jansen, et al., *Precision Study of Excited State Effects in Nucleon Matrix Elements*, *Phys.Lett.* B704 (2011) 89–93.

[86] C. Alexandrou, S. Dinter, V. Drach, K. Hadjiyiannakou, K. Jansen, et al., *A Stochastic Method for Computing Hadronic Matrix Elements*, *arXiv preprint 1302.2608* (2013).

[87] S. Güsken, U. Löw, K. Mütter, R. Sommer, A. Patel, et al., *Nonsinglet Axial Vector Couplings of the Baryon Octet in Lattice QCD*, *Phys.Lett.* B227 (1989) 266.

[88] C. Alexandrou, F. Jegerlehner, S. Güsken, K. Schilling, and R. Sommer, *B meson properties from lattice QCD*, *Phys.Lett.* B256 (1991) 60–67.

[89] C. Allton, C. T. Sachrajda, R. Baxter, S. Booth, K. Bowler, et al., *Gauge invariant smearing and matrix correlators using wilson fermions at* $\beta = 6.2$, *Phys.Rev.* D47 (1993) 5128–5137.

[90] M. Albanese, F. Costantini, G. Fiorentini, F. Flore, M. Lombardo, et al., *Glueball Masses and String Tension in Lattice QCD*, *Phys.Lett.* B192 (1987) 163–169.

[91] M. Della Morte, B. Jäger, T. Rae, and H. Wittig, *Improved interpolating fields for hadrons at non-zero momentum*, *Eur.Phys.J.* A48 (2012) 139.

[92] M. Della Morte, B. Jäger, T. D. Rae, and H. Wittig, *Improved interpolating fields for hadrons at non-vanishing momentum*, *PoS* LATTICE2012 (2012) 260.

[93] G. M. von Hippel, B. Jäger, T. D. Rae, and H. Wittig, *The Shape of Covariantly Smeared Sources in Lattice QCD*, *JHEP* 1309 (2013) 014.

[94] G. M. von Hippel, B. Jäger, T. Rae, and H. Wittig, *Getting Covariantly Smeared Sources into Better Shape*, *PoS* LATTICE2013 (2013) 424.

[95] D. B. Leinweber, R. Woloshyn, and T. Draper, *Electromagnetic structure of octet baryons*, *Phys.Rev.* D43 (1991) 1659–1678.

[96] C. Alexandrou, R. Baron, M. Brinet, J. Carbonell, V. Drach, et al., *Nucleon form factors with dynamical twisted mass fermions*, *PoS* LATTICE2008 (2008) 139.

[97] B. Knippschild, *Baryons in the chiral regime*. PhD thesis, Johannes Gutenberg-Universität, 2011.

[98] G. von Hippel, J. Hua, B. Jäger, H. Meyer, T. D. Rae, et al., *Fitting strategies to extract the axial charge of the nucleon from lattice QCD*, *PoS* LATTICE2013 (2013) 446.

[99] L. Maiani, G. Martinelli, M. Paciello, and B. Taglienti, *Scalar Densities and Baryon Mass Differences in Lattice QCD With Wilson Fermions*, *Nucl.Phys.* B293 (1987) 420.

[100] J. Bulava, M. Donnellan, and R. Sommer, *On the computation of hadron-to-hadron transition matrix elements in lattice QCD*, *JHEP* 1201 (2012) 140.

[101] J. J. Kelly, *Simple parametrization of nucleon form factors*, *Phys. Rev. C* 70 (Dec, 2004) 068202.

[102] T. R. Hemmert, M. Procura, and W. Weise, *Quark mass dependence of the nucleon axial vector coupling constant*, *Phys.Rev.* D68 (2003) 075009.

[103] S. R. Beane and M. J. Savage, *Baryon axial charge in a finite volume*, *Phys.Rev.* D70 (2004) 074029.

[104] G. Colangelo, A. Fuhrer, and S. Lanz, *Finite volume effects for nucleon and heavy meson masses*, *Phys.Rev.* D82 (2010) 034506.

[105] M. Göckeler, T. Hemmert, R. Horsley, D. Pleiter, P. Rakow, et al., *Nucleon electromagnetic form factors on the lattice and in chiral effective field theory*, *Physical Review D* 71 (2005).

[106] M. Göckeler, P. Hägler, R. Horsley, Y. Nakamura, M. Ohtani, et al., *Nucleon structure with partially twisted boundary conditions*, *PoS* LATTICE2008 (2008) 138.

[107] G. Bennett, B. Bousquet, H. Brown, G. Bunce, R. Carey, et al., *Final report of the E821 muon anomalous magnetic moment measurement at BNL*, *Phys. Rev. D* 73 (2006) 072003.

[108] F. Jegerlehner and A. Nyffeler, *The muon $g-2$*, *Phys. Rept.* 477 (2009) 1–110.

[109] J. Bailey, K. Borer, F. Combley, H. Drumm, C. Eck, et al., *Final Report on the CERN Muon Storage Ring Including the Anomalous Magnetic Moment and the Electric Dipole Moment of the Muon, and a Direct Test of Relativistic Time Dilation*, *Nucl.Phys.* B150 (1979) 1.

[110] J. Schwinger, *On Quantum-Electrodynamics and the Magnetic Moment of the Electron*, *Phys. Rev.* 73 (1948) 416–417.

[111] T. Aoyama, M. Hayakawa, T. Kinoshita, and M. Nio, *Complete tenth-order QED contribution to the muon $g-2$*, *Phys. Rev. Lett.* 109 (Sep, 2012) 111808.

[112] P. W. Higgs, *Broken symmetries and the masses of gauge bosons*, *Phys. Rev. Lett.* 13 (Oct, 1964) 508–509.

[113] F. Englert and R. Brout, *Broken symmetry and the mass of gauge vector mesons*, *Phys. Rev. Lett.* 13 (Aug, 1964) 321–323.

[114] T. Blum, *Lattice calculation of the lowest order hadronic contribution to the muon anomalous magnetic moment*, *Phys.Rev.Lett.* 91 (2003) 052001.

[115] M. Göckeler, R. Horsley, W. Kürzinger, D. Pleiter, P. Rakow, et al., *Vacuum polarization and hadronic contribution to muon $g-2$ from lattice QCD*, *Nucl.Phys.* B688 (2004) 135–164.

[116] C. Aubin and T. Blum, *Calculating the hadronic vacuum polarization and leading hadronic contribution to the muon anomalous magnetic moment with improved staggered quarks*, *Phys.Rev.* D75 (2007) 114502.

[117] D. B. Renner, X. Feng, K. Jansen, and M. Petschlies, *Leading order hadronic contribution to $g-2$ from twisted mass QCD*, *PoS* LATTICE2010 (2010) 155.

[118] X. Feng, K. Jansen, M. Petschlies, and D. B. Renner, *Two-flavor QCD correction to lepton magnetic moments at leading-order in the electromagnetic coupling*, *Phys.Rev.Lett.* 107 (2011) 081802.

[119] P. Boyle, L. Del Debbio, E. Kerrane, and J. Zanotti, *Lattice Determination of the Hadronic Contribution to the Muon $g-2$ using Dynamical Domain Wall Fermions*, *Phys.Rev.* D85 (2012) 074504.

[120] G. de Divitiis, R. Petronzio, and N. Tantalo, *On the extraction of zero momentum form factors on the lattice*, *Physics Letters B* 718 (2012) 589 – 596.

[121] M. Della Morte, B. Jäger, A. Jüttner, and H. Wittig, *Lattice calculations of the leading hadronic contribution to $(g-2)_\mu$*, *PoS* LATTICE2012 (2012) 175.

[122] X. Feng, S. Hashimoto, G. Hotzel, K. Jansen, M. Petschlies, et al., *Computing the hadronic vacuum polarization function by analytic continuation*, *Phys.Rev.* D88 (2013) 034505.

[123] A. Francis, B. Jäger, H. B. Meyer, and H. Wittig, *A new representation of the Adler function for lattice QCD*, *Phys.Rev.* D88 (2013) 054502.

[124] F. Burger, X. Feng, G. Hotzel, K. Jansen, M. Petschlies, et al., *Four-Flavour Leading Hadronic Contribution To The Muon Anomalous Magnetic Moment*, *arXiv preprint 1308.4327* (2013).

[125] M. Golterman, K. Maltman, and S. Peris, *Tests of hadronic vacuum polarization fits for the muon anomalous magnetic moment*, *arXiv preprint 1309.2153* (2013).

[126] M. Golterman, K. Maltman, and S. Peris, *Tests of hadronic vacuum polarization fits for the muon anomalous magnetic moment*, *arXiv preprint 1310.5928* (2013).

[127] M. Della Morte, G. Herdoiza, H. Horch, B. Jäger, A. Jüttner, et al., *Computing the Adler function from the vacuum polarization function*, *PoS* LATTICE2013 (2013) 304.

[128] M. Della Morte, G. Herdoiza, H. Horch, B. Jäger, A. Jüttner, et al., *Fitting the lattice vacuum polarisation function to perturbation theory*, *PoS* LATTICE2013 (2013) 444.

[129] B. Lautrup and E. De Rafael, *Calculation of the sixth-order contribution from the fourth-order vacuum polarization to the difference of the anomalous magnetic moments of muon and electron*, *Physical Review* 174 (1968) 1835–1842.

[130] B. Lautrup, A. Peterman, and E. De Rafael, *Recent developments in the comparison between theory and experiments in quantum electrodynamics*, *Physics Reports* 3 (1972) 193–259.

[131] A. Jüttner and M. Della Morte, *New ideas for $g-2$ on the lattice*, *PoS* LATTICE2009 (2009).

[132] M. Della Morte and A. Jüttner, *Quark disconnected diagrams in chiral perturbation theory*, *JHEP* 1011 (2010) 154.

[133] B. Jäger, *Lattice Determination of the Leading Order Hadronic Contribution to the Anomalous Magnetic Moment of the Muon*. Diploma thesis, Johannes Gutenberg-Universität, 2010.

[134] M. Della Morte, B. Jäger, A. Jüttner, and H. Wittig, *Towards a precise lattice determination of the leading hadronic contribution to* $(g-2)_\mu$, *JHEP* 1203 (2012) 055.

[135] C. Aubin, T. Blum, M. Golterman, and S. Peris, *The hadronic vacuum polarization with twisted boundary conditions*, *Phys.Rev.* D88 (2013) 074505.

[136] C. Aubin, T. Blum, M. Golterman, and S. Peris, *Model-independent parametrization of the hadronic vacuum polarization and* $g-2$ *for the muon on the lattice*, *Phys.Rev.* D86 (2012) 054509.

[137] C. Michael, *Fitting correlated data*, *Phys.Rev.* D49 (1994) 2616–2619.

[138] C. Michael and A. McKerrell, *Fitting correlated hadron mass spectrum data*, *Phys.Rev.* D51 (1995) 3745–3750.

[139] G. Golub and W. Kahan, *Calculating the singular values and pseudo-inverse of a matrix*, *Journal of the Society for Industrial and Applied Mathematics: Series B, Numerical Analysis* (1965) 205–224.

[140] B. Gough, *GNU Scientific Library Reference Manual - Third Edition*. Network Theory Ltd., 2009.

[141] Wolfram Research, Inc., *Mathematica, Version 8.0*. Champaign, Illinois, 2010.

[142] K. Chetyrkin, J. H. Kühn, and M. Steinhauser, *Three loop polarization function and* $O(\alpha_s^2)$ *corrections to the production of heavy quarks*, *Nucl.Phys.* B482 (1996) 213–240.

[143] M. Della Morte, R. Frezzotti, J. Heitger, J. Rolf, R. Sommer, et al., *Computation of the strong coupling in QCD with two dynamical flavors*, *Nucl.Phys.* B713 (2005) 378–406.

[144] M. Della Morte, R. Hoffmann, F. Knechtli, J. Rolf, R. Sommer, et al., *Non-perturbative quark mass renormalization in two-flavor QCD*, *Nucl.Phys.* B729 (2005) 117–134.

[145] P. Fritzsch, J. Heitger, and N. Tantalo, *Non-perturbative improvement of quark mass renormalization in two-flavour lattice QCD*, *JHEP* 1008 (2010) 074.

[146] G. von Hippel. private communication, 2013.

[147] D. Bernecker and H. B. Meyer, *Vector Correlators in Lattice QCD: Methods and applications*, *Eur.Phys.J.* A47 (2011) 148.

[148] A. Francis, B. Jäger, H. B. Meyer, and H. Wittig, *Adler function and hadronic vacuum polarization from lattice vector correlation functions in the time-momentum representation*, *PoS* LATTICE2013 (2013) 305.

[149] X. Feng, S. Hashimoto, G. Hotzel, K. Jansen, M. Petschlies, et al., *Using analytic continuation for the hadronic vacuum polarization computation*, *arXiv preprint 1311.0652* (2013).

[150] V. Gülpers, *Improved stochastic estimators for disconnected contributions to mesonic form factors in Lattice QCD*. Diploma thesis, Johannes Gutenberg-Universität, 2011.

[151] V. Gülpers, G. von Hippel, and H. Wittig, *The scalar pion form factor in two-flavor lattice QCD*, *arXiv preprint 1309.2104* (2013).

[152] M. Göckeler, T. Hemmert, R. Horsley, D. Pleiter, P. Rakow, et al., *Nucleon electromagnetic form-factors on the lattice and in chiral effective field theory*, *Phys.Rev.* D71 (2005) 034508.